Synthesis and study of different heterostructured nanocomposite materials

Thesis submitted to

VIDYASAGAR UNIVERSITY, MIDNAPORE

For the Degree of

DOCTOR OF PHILOSOPHY(SCIENCE)

BY

Tushar Kanti Jana

Department of Physics and Technophysics

Vidyasagar University, Midnapore 721102

West Bengal, India

2016

Dedicated to my family

Declaration

I, Tushar Kanti Jana, hereby declare that the material contained in this thesis is the result of my own work.The matter of this thesis is original and has not been submitted in whole or in part for the award of a degree at this or any other university.

Tushar kanti Jana

(Tushar kanti Jana)

Dept. of Physics and Technophysics

Vidyasagar University

Midnapore, West Bengal

VIDYASAGAR UNIVERSITY

MIDNAPORE, DIST.: PASCHIM MEDINIPUR

PIN - 721102 (W.B.) INDIA

Dr. Kuntal Chatterjee
Assist.Professor
Department of Physics and Technophysics
Phone : **+91 9474816352**
E-mail : kuntal@mail.vidyasagar.ac.in

Date: 05. 12. 2016

CERTIFICATE

This is to certify that the thesis entitled **"SYNTHESIS AND STUDY OF DIFFERENT HETEROSTRUCTURED NANOCOMPOSITE MATERIALS"** submitted by Tushar Kanti Jana who got his name registered on 04.01.2011 for the award of Ph. D (science) degree of Vidyasagar University , is absolutely based upon his own work under my supervision and that neither this thesis nor any part of it has been submitted for any degree/diploma or any other academic award anywhere before.

Signature of supervisor:

Kuntal Chatterjee 05.12.2016

(Dr. Kuntal Chatterjee)
Assistant Professor
Dept. Physics and Technophysics
Vidyasagar University

Assistant Professor
Dept. of Physics
Vidyasagar University.

Acknowledgement

First of all, I would like to express my heartfelt gratitude to my doctorate advisor, Dr. Kuntal Chatterjee, at Vidyasagar University, for the honor to work under his guidance. I am really proud of being the Ph. D student to discover the nano-world in his laboratory. I greatly appreciate the freedom opportunity he has given me to pursue my research in my own way. It is noteworthy to mention that I decided to pursue my doctorate degree in Department of Physics and Technophysics, Vidyadsagar University due to his priceless guidance, support and encouragement that have made my life easier and my research better. I feel fortunate to be able to work in his laboratory. His association will remain a beacon light to me throughout my career.

It is my pleasure and honor to thank Dr. Satyajit Saha, Dr. Radharaman Pal, Dr. P.C. Jana and Dr. Surajit Gosh of Department of Physics and Technophysics for their excellent teaching, helpful discussion and kind direction.

I am very much grateful and want to thank Kingshukda, Sujitda and Sachhuda who have helped me in the Department.

A special thanks to my lab mates Arnab, Saikat, Koushik, Sankalpita, Parbati, Amit who make my life here in the lab not lonely but fruitful and enjoyable.

I deeply appreciate the help by Suman Maji and Ramaprasad Maiti whenever I need.

I express my deepest and endless thanks to my wife, brother, sister, parents, my little nephew and sweet niece for their unlimited love, encouragement and support.

Lastly, I take this opportunity to thank all of them who supported me directly, indirectly, technically or morally.

Tushar Kanti Jana

(Tushar kanti Jana)

Publications:

1. Photocatalytic and antibacterial activity of cadmium sulphide/zinc oxide nanocomposite with varied morphology, **T.K. Jana,** S. K. Maji, A. Pal, R. P. Maiti, T. K. Dolai, K. Chatterjee, **Journal of Colloid and Interface Science** 480 (2016) 9–16.

2. TiO_2 Decorated Silica Nanospheres for Highly Efficient Photocatalytic Application under Visible Light Irradiation, A. Pal, **T.K. Jana,** K. Chatterjee, **Materials Research Bulletin** 76 (2016) 353–357.

3. Magnetic and photocatalytic study of Co_3O_4-ZnO nanocomposite, **T.K. Jana,** A. Pal, K. Chatterjee, **Journal of Alloys and Compounds** 653 (2015) 338-344.

4. Self assembled flower like CdS–ZnO nanocomposite and its photocatalytic activity, **T.K. Jana**, A. Pal, K. Chatterjee, **Journal of Alloys and Compounds** 583 (2014) 510–515.

5. Morphology dependent magnetic properties of α-Fe_2O_3 nanostructures, S. Chakrabarty, **T. K. Jana,** K. De, S. Das, K. Dey and K. Chatterjee, **Materials Research Express 1** (2014) 046104.

ABSTRACT

The main objective of this thesis is to highlight the state of knowledge in synthesis, characterization, different properties, and potential applications for different heterostructured nanocomposite materials. Structural, chemical and morphological details of these nanocomposites have been studied. This work describes some possible applications of CdS/ZnO(three system), Co_3O_4/ZnO nanocomposites having different morphology.

In chapter 1, basic introductory discussion on nanostructured materials considering the origin of different properties that distinctively differs from their bulk components has been put forward. Some novel properties of as synthesized nanocomposites like optical, magnetic, photocatalytic and antibacterial properties are also discussed and have been reviewed.

Chapter 2 highlights chemical synthesis routes for CdS/ZnO(three system), Co_3O_4/ZnO, nanocomposites as well as how to engineer morphological variation in that nanophase system by simple technique. This chapter also includes structural, Chemical, optical and Morphological study of the nanocomposites extensively.

Chapter 3 presents the photocatalytic property of as synthesized nano composites. The visible-light photocatalytic activity of CdS-ZnO1:1, CdS-ZnO1:2, CdS-ZnO1:3 and Co_3O_4-ZnO samples was carried out by using it to degrade rhodamine B dye aqueous solution. To address the photocatalytic effect in details a

possible charge transfer mechanism in our synthesized system is proposed as a modified energy band diagram.

In Chapter 4, study of magnetic behaviour of Co_3O_4-ZnO is presented. The M-*T* and *M-H* variation of prepared Co_3O_4-ZnO nanocomposite are studied. The blocking temperature (T_B) for the Co_3O_4-ZnO nanocomposite, the signature of T_B has been observed at nearly 33K. The most interesting observation for the Co_3O_4-ZnO nanocomposite sample is that, nearly at 15K both M_{ZFC} and M_{FC} data start to increase rapidly.

Chapter 5 demonstrates the antibactrrial activity of as prepared nanocomposites. Investigation showed that CdS-ZnO nanocomposites showed larger inhibition zones against *Staphylococcus sp* than *Escherichia coli and Klebsiella sp* and demonstrates the potential application of CdS/ZnO nanocomposites as an effective antibacterial agent against *Staphylococcus sp, Escherichia coli and Klebsiella sp*.

Chapter 6 includes the conclusion and future work proposals. The work can be continued in different directions such as synthesis and study of Fe_2O_3/ZnO, RGO/metal oxide nanocomposites, antibacterial property and water splitting by different nanocomposites etc.

CONTENTS

Chapter 1:

1. Introduction and review

Chapter 2:

2. Synthesis of nanocomposite and study of Structural and Optical properties

CHAPTER 1

INTRODUCTION AND REVIEW

1.1 Nanoscience and Nanotechnology: A General Introduction

" Everything we see around us is made of atoms, the tiny elemental building blocks of matter. From stone to copper, bronze, iron, steel, and now silicon, the major technological ages of humankind have been defined by what these atoms can do in huge aggregates, trillions of atoms at a time, molded, shaped, and refined as macroscopic objects "

____ R. E. Smalley

Nanotechnology deals with the development and practical application of structures and devices having dimensions of the order of a billionth of a meter (1 nm = 10^{-9} m). Nanostructures are those structures with at least one dimension below 100 nm[1]. Smallest pieces of everything around us, are measured in nanometers. A water molecule is less than 1 nm. Size of a typical bacterium is of the order of about 1000 nm and virus are even smaller than the bacterium. Red blood corpuscles are in nanometers and DNA is in the 2.5 nm range. Length of ten hydrogen atoms placing side by side is 1 nm. The prefix 'nano'-being derived from the Greek word 'nanos', synonymous to 'dwarf' meaning extremely small. The properties of manufactured products in nanotechnology depend on how the atoms are arranged. We can make diamond if we rearrange the atoms in coal and computer chips if we rearrange the atoms in sand adding a few other trace elements. The existence of structures of nanometer dimensions is not new and infact such structures have existed on Earth as long as life itself. The abalone, a mollusk, makes very strong shells by organizing calcium carbonate into strong nanostructured bricks held together by a glue made of a carbohydrate-protein mix. Cracks produced on the outside are unable to move through

the shell due to the nanostructured bricks.The shells having the natural demonstration represent that a structure fabricated from nanoparticles can be much stronger. It is known that Roman glassmakers were manufacturing glasses containing nanosized metals. The Lycurgus cup, an artefact from this period was made from soda lime glass containing silver and gold nanoparticles. When a light source is placed inside it, the color of the cup changes from green to a deep red. The beautiful colors of the windows of medieval cathedrals are due to the presence of metal nanoparticles in the glass. In 1959, Richard P. Feyman suggested that it should be possible to construct machines small enough to manufacture objects with atomic precision. On 29 December 1959, he presented a visionary and prophetic lecture at the meeting of American Physical Society at the California Institute of Technology(Caltech) after dinner, entitled "There is plenty of Room at the bottom", where he speculated on the possibility and potential of nanosized materials[2]. He proposed manipulating individual atoms to make new small structures having very different properties. Feyman said, " What I want to talk about is the problem of manipulating and controlling things on a small scale". He described how the entire Encyclopedia Britannica could be written on the head of a pin. The lecture is widely considered to be the foreshadowing of nanotechnology. The science behind nanotechnology is known as nanosciences. Physics of low-dimensional system helps to understand the nuances of nanosciences. Nanoscience is a convergence of physics, chemistry, material science and biology, that deals with the manipulation and characterization of matter at nanoscale. It involves self-assembled nanostructures, thin film growth, and manipulation of nanoscale as well as nanolithography to fabricate nanodevices. Nanoscience reveals how materials behave when their sizes close to atomic dimension. In the nanoscale the properties of materials are different from those at a larger scale. Nanostructured materials have a

relatively larger surface compared to the same mass of material produced in a larger form. A large percentage of atoms become surface atoms compared to their bulk counterparts resulting more surface energy. Thus large surface to volume ratio can make materials more chemically reactive and affect their strength and electrical properties. Particularly, quantum effects play an important role to dominate the behaviour of matter at nanoscale. It can affect optical, electrical and magnetic behaviour of materials. Nanoscale materials are classified into three categories: (a) the two-dimensional(2D) nanosystems-quantum well, (b) one-dimensional(1D)nanosystem- quantum wire, (c) zero-dimensional(0D) nanosystem-quantum dot. The word quantum is added because the changes in properties arise from the quantum-mechanical nature of physics in the domain of the ultrasmall. The dimensionality affects when one, two or all three dimensions become small. Quantum mechanical laws are used to describe the behaviours of nanomaterials closer in size to atoms or molecules. Electrons are confined in a small space rather than the space of bulk material resulting in their confinement. This quantum confinement affects the optical properties of the nanoparticles where the quanta of light or the electromagnetic waves interact with the confined electron of the nanoparticle. The properties of solid state functional materials are controlled by the quantum confinement of electrons originated from the potential well of the nanometer sized structure.

Two approaches are followed for the fabrication of nanostructured materials-(a) bottom-up approach, and (b) top-down approach. The bottom-up approach is to collect, consolidate and fashion individual atoms and molecules into the desired structure. Top-down approach starts with a large-scale object or pattern and gradually reduces to its nano dimensions. Lithography, ball milling belong to this category. Bottom-up approach which is widespread in biology is carried out by a sequence of

chemical reactions. Self-assembly is such an approach to make nanostructures which referred to as botto-up nanotechnology. It starts with individual molecules or atoms which are assembled to construct the desired structure.

Nanotechnology and nanoscience have indeed taken cetre stage in the arena of academic science and as a result it is developing rapidly in different fields such as physics, biology, engineering, chemistry, computer science and more[3-4.] Nanotechnology has the potential to impact all the commercial products today and of tomorrow in many areas of life, not least of which would be new and improved health treatments; reduced use of some harmful or scare resources; cleaner, faster and safer manufacturing; quicker and smaller devices; increased life-cycle of products; many other improvements to existing products. It has the potential to change our living way. The Nano revolution taking place is attributed to the availability of the tools that allow scientists to explore the world at the nanoscale and transform their discoveries into products and services with practical benefits to everyday life. As all industrial sectors depend on materials and devices made from atoms and molecules, they will be radically transformed by application of nanotechnology. Nanotechnology is the next industrial revolution that directly benefit common man. Thus , as we develop our ability to manufacture computer chips with smaller features and improve our ability to cure disease at the molecular level, nanotechnology is here.

1.2 Preparation of nanostructured materials:

As the size of an object gets smaller, it goes from our macroscopic world to the microscopic field, and finally into the nanoscale range. The mother nature has created biological materials with sizes covering all length scales: red ant-500,000 nm, human hair(width)- 50,000 nm, diameter of a typical bacterium-1,000-10,000 nm, human immunodeficiency virus- 90 nm, cell membrane- 10 nm, protein-5 nm, water molecule- 1nm, Hydrogen atom-0.1nm. Nanostructures can be fabricated using top-down and bottom up methods that are the two important broad categories. A tremendous progress in modern nanoscience and nanotechonology has been achieved which allows us to manipulate and manufacture things at all length scales not only via the traditional ―top-down approaches[5] which are essentially substractive; that is, a material is removed by grinding, ball milling etc. but also through ―bottom-up approaches[6] which assemble atomic or molecular building blocks in controllable fashions to form various desired structures. When it comes to the fabrication of nanoparticles with uniform size, the bottom-up approaches are most emphasized, as the top-down techniques can cause significant crystallographic damages and additional defects to the processed patterns. Some of the top-down techniques for fabrication of nanoparticles are― Ball miling[7-12]; nanocomposites and mixtures of elemental powders are fabricated, Laser ablation method[13-19]; broad range of nanoparticles including CNTs are fabricated, Arc discharge method[20-27]; Metal carbides, carbon nanotubes, fullerenes, carbon nanofibers are fabricated, Inert gas condensation[28-34]; oxides, alloys and semiconductors are fabricated, etc. Eric Drexler, a pioneer in nanotechnology, said, "our ability to arrange atoms lies at the foundation of technology". From this point on, several bottom-up approaches have blossomed, trying to fabricate nanostructures one atom at a time, in the most efficient and precise

way possible. Some of the bottom-up methods for fabrication of nanoparticles are—Chemical vapour deposition(CVD)[35-41]; CNTs, fullerenes and boron nanotubes are synthesized, Molecular beam epitaxy(MBE)[42-49]; compound semiconductors and thin films are fabricated, Wet chemical synthesis route[50-57]; semiconductor, metal oxides nanoparticles and nanocomposites are synthesized, Sol-gel synthesis[58-67]; colloidal and oxide nanoparticles are prepared, Hydrothermal synthesis[68-73]; elemental nanopowders and mostly oxides are synthesized, Microwave method[74-77]; various oxide nanomaterials including TiO_2 are synthesized, Laser pyrolysis[78-82]; Nanotubes, iron carbides shell-structured nanoparticles, Fe_2O_3, MnO_2, TiO_2, Ti, FeC, carbides, Microemulsion Method[83-88]; Metal nanoparticles (Cd, Ag, Au, Cu, Co, Pt, Pd, Ni, Fe), metal oxides (TiO_2, SiO_2, Fe_2O_3), metal sulfates ($BaSO_4$), metal carbonates ($BaCO_3$, $CaCO_3$), magnetic polymeric particles, silica-coated iron oxide, Sonochemical Method[89-94]; iron nanoparticles, metal oxides, alloy nanoparticles, coating for the surface of various particles, nitride, ferrite, chalcogenides (ZnS,CdS, CdSe, PbS, PbSe), etc.

1.3 Review of nanocomposites :

Nanocomposites consist of two or more synthesized materials having nanoscale dimension. A large variety of systems such as one-dimensional, two-dimensional, three-dimensional, and amorphous materials made of distinctly dissimilar components and mixed at the nanometer scale are defined as nanocomposites. Nanocomposites exhibit different optical, chemical, physical and mechanical properties which are not present in the constituent bulk materials[95-99]. Formation of the nanocomposites could be possible by materials such as organic with organic, organic with inorganic, and inorganic with inorganic. The properties of nanocomposites largely depend on their

morphology and interfacial characteristics. The surface energy of the nanocomposites is significantly higher as compared to that of the bulk. The fabrication of various nanocomposites is a fast growing area of research. Nanocomposites are gradually attracting more and more attention, since these nanocomposites have emerged at the frontier between materials chemistry and many other fields, such as electronics, biomedical, pharmaceutical, optics, and catalysis. Nanocomposites are highly functional materials with modified properties. The properties can be modified by changing either the constituting materials or the ratio of the elements. Ultimately, particles show distinctive properties of the different materials employed together. This is especially true of the inherent ability to manipulate the surface functions to meet the diverse application requirements. Furthermore, there has been a gradual increase in research activity because of the tremendous demand for more and more advanced materials fueled by the demands of modern technology.

Using rhodamine B degradation as model dye, **L**iu et al.[100] studied the photocatalytic activities of the nanocomposites under visible light irradiation. They explored the synthesis of ZnO/titanate nanotube nanocomposites via a two step solution chemistry method and photocatalytic property under visible light illumination. The optical absorption spectra of the nanocomposite shows a combination of the two spectra coming from ZnO nanoparticles and titanate nanotubes and the absorption edge of ZnO nanoparticles shows an obvious blue shift after the decoration with titanate nanotubes. The high photocatalytic property was probably caused by the reduction of O_2 by the injected electrons, which improves the photocatalytic property of the nanocomposites. Results of their work show the great potential of the nanocomposites in photocatalytic uses.

Vaidya et al.[101] carried out detailed investigation on the variation of the optical properties of the structures and the nature of shell-forming agent synthesized by a reverse-micelle based methodologywith a two step approach to obtain uniform structures of $Ag@TiO_2$ nanocomposite using titanium hydroxyacylate as the shell forming agent. The best (most uniform) shell formation can be obtained using titanium hydroxyacylate as the shell-forming agent. Presence of capping agent (2-mercaptoethanol) on silver in $Ag@TiO_2$ affects the uniformity of the shell. $Ag@TiO_2$ core–shell nanostructures (without 2-mercaptoethanol) exhibited SERS activity. The PL stydy shows intensity (of TiO_2) decreases in the nanocomposite in presence of 2-mercaptoethanol due to the formation of Ag_2S as an intervening shell.

The use of fluorescent nanocomposites as indicators in biological applications such as imaging and sensing has dramatically increased. Nanocomposites with core-shell architecture are monodisperse, bright, photostable, and amenable to further surface modification for the conjugation of biomolecules and/or fluorophores combining diverse functionalities into a single hybrid nanocomposite. Aslan et al.[102] developed core-shell (silver core-silica shell) nanocomposites with various shell thicknesses featuring a variety of fluorophores, and have demonstrated their application in metal-enhanced fluorescence (MEF) and single nanoparticle sensing. The development of highly versatile highly fluorescent core-shell $Ag@SiO_2$ nanocomposites allow researchers to incorporate any fluorophore to the outer-silica shell by two simple methods (i.e., simple doping or covalent attachment) while exploiting the benefits of using a silver core for MEF.

Room temperature photoluminescence spectrum presents only an ultraviolet emission bandedge peak at 383 nm for Ag_2O/ZnO nanocomposite, exhibiting an excellent optical quality. Wang et al.[103] reported the synthesis Ag_2O/ZnO nanohybrid composite with a feasible simple two-step procedure without any surfactants as nanocomposites represent better properties. A possible growth mechanism is proposed based on these experimental results. The as-synthesized flowerlike Ag_2O-ZnO nanohybrid possesses Ag_2O nanoparticles coated uniformly on the surface of ZnO microflowers. A possible growth mechanism is proposed based on the experimental results. The composite exhibited greatly optical properties compared to ZnO microflowers.

Nanocomposites are capable to manipulate the optical properties and enhance the functionality of semiconductor nanostructure. Nayak et al.[104] reported the synthesis of CdS–ZnO composite nanorods by a low temperature aqueous chemical growth technique. ZnO nanorods were dip coated with CdS. In CdS–ZnO nanocomposite, CdS acts as a visible sensitizer and ZnO, being a wide band gap (3.34 eV) semiconductor, is responsible for effective charge separation reducing the recombination process. With CdS–ZnO nanorods as catalyst, the 3,4-dihydroxy benzoic acid (DHBA) was successfully degraded in an aqueous medium, under illumination with visible radiation and possible mechanism was discussed.

The structure and the vibrational properties of the above nanocomposite were systematically investigated.

As Au nanoparticles (AuNPs) are good quenchers once they closely contact with luminophore, an effort was made by fabricating Au/CdS nanocomposite to enhance chemiluminescence(ECL). Shi et al.[105] reported different fabrication approaches to

obtain enhanced electrogenerated chemiluminescence (ECL) behaviour based on Au/CdS nanocomposite films by tuning the amount of AuNPs in the nanocomposite. The strong ECL emission from Au/CdS nanocomposites film was exploited to determine H_2O_2 and could be useful for ECL analysis and detection based on Au/CdS nanocomposite. The results demonstrated in this article may provide guidance for designing stable and high-efficient biosensors.

Chou et al.[106] synthesized Ag/SiO_2 nanocomposite which is shown to be stable up to 1000^{o}c maintaining its original shape and showing no signs of sintering between particles. These porous composite particles can be used as catalysts for applications at high temperatures. Sto¨ber process is followed to fabricate Ag/SiO_2 core shell particles and polyvinylpyrrolidone (PVP) as protecting agent for Silver colloids. The shell thickness is controlled by the amount of tetraethyl orthosilicate (TEOS). Porous silica shell structure is obtained after burning off the PVP molecules which are trapped and dispersed in the silica shell during the silica growth. As silica shell begins to cover surface of the silver colloids, the absorption peak at 409 nm shifted to longer wavelengths due to changes of dielectric constant of the environment near the silver surface.

To enhance photocatalytic activity, noble metal Ag is deposited on a TiO_2 surface, because it acts as an electron trap promoting interfacial charge transfer processes in the composites. Cheng et al[107] and his group fabricated $Ag@TiO_2$ nanocomposite nanowires using vapor-thermal method, and the composite superstructures show higher photocatalytic activity than conventional TiO2 and P25 particles for the photocatalytic decolorization of Rhodamine B aqueous solution at ambient temperature. This study provides new insights into the design and fabrication of

advanced photocatalytic materials with complex hierarchical architectures for wastewater treatment. The synthesis strategy may be extended to the preparation of complex functional structures with controlled physicochemical properties.

In order to develop multifunctional NCs with solubility and biocompatibility in aqueous solution Wang et al.[108] demonstrated the chemical synthesis of water-soluble and bifunctional ZnO-Au nanocomposites by a simple and effective route to obtain semiconductor and metal heterostructure composites that are soluble in aqueous media and have expanded functionalities of nanostructured materials in technological applications. ZnO-Au NCs provide a distinct dual functionality:ZnO provides fluorescence and Au is used for organic functionality for bioconjugation. The UV emission of the ZnO-Au NCs is stronger than that of pure ZnO nanocrystals, which is attributed to the strong interfacial interactions between ZnO and Au. The surface plasmon absorption band of ZnO-Au NCs in aqueous solution is distinctly broadened and red-shifted relative to monometallic Au nanoparticles. The investigation on the functional multicomponent composites as ZnO-Au NCS explores not only the biological applications but also by better understanding the interfacial interaction mechanism of metal Au and semiconductor ZnO components.

The basic requirement for exhibiting good photocatalytic performance by a heterosystem-based semiconductor photocatalyst are (i) good crystallinity to retard charge recombination, (ii) high surface area by size optimization into nanodimension, and (iii) higher contact area of semiconductor surface and electrolyte responsible for hole scavenging. Barpuzary et al.[109] and his research group fabricated nanourchin-shaped narrow-band-gap CdS@Al_2O_3 and CdS@ZnO nanocomposites photocatalysts

with high surface area combined with good crystallinity result in effective photocatalysis. The investigation manifests the production of H_2 by use of $CdS@Al_2O_3$ and CdS@ZnO heterostructures (hereafter, CdS@oxide) having urchinlike morphology. This report provides the cost-effective hydrothermal method for high rates of H_2 production even in the absence of expensive noble metals reducing the total cost of H_2 production efficiently.

Kundu et al.[110] studied photocatalytic activity of ZnO/CdS nanocomposite by the degradation of methylene blue dye under solar irradiation. They fabricated ZnO/CdS heterostructure vai a simple wet chemical route which involves the nucleation of a Cd-precursor on ZnO nanorods with a subsequent sulfidation step leading to the formation of the ZnO/CdS nanoscale heterostructures. The synthesis procedure confirms that the morphology and composition of the nanohybrid at the interface had been controlled by changing conditions of sulfidation. This study shows that the photoactivity of the material can be tuned by manipulating the interface of the heterostructure. The novel method is advantageous to a wide range of similar hybrids for photocatalytic and photovoltaic application.

Study of photoelectrochemical properties of nanocomposites is necessary for better understanding of improved photocatalytic properties of the nanocomposites. Vinodgopal et al.[111] prepared SnO_2/TiO_2 nanocomposite and studied electrochemically assisted photocatalytic degradation of a textile azo dye naphthol blue black (NBB). The improved photocatalytic activity composite catalyst is ascribed to increased charge separation in these systems. Photoelectrochemical and photocatalytic

degradation experiments were also carried out in both nitrogen- and oxygen-saturated solutions with an externally applied electrochemical bias.

Photocatalysts with magnetic core become one of the most promising candidates for the exploration of new applications. Wu et al.[112] successfully prepared the spindle-like mesoporous α-Fe_2O_3/ZnO core−shell heterostructures by a facile wet-chemical routes. The different structure features of the iron oxide/ZnO composite particles was obtained by tailoring the concentration of zinc precursor which controls thickness of ZnO layer. Magnetic and optical properties of the nanostructures were studied by various characterization techniques. Photocatalytic activity was tested by the degradation of RhB dye and the degradation rate is higher than that of the naked iron oxide seeds, commercial TiO_2 nanoparticles (P25). Significantly enhanced degradation rate attributed to the effective electron−hole separation at the interfaces of the core-shell heterostructures. The enhanced performance demonstrates the importance of evaluating new composite photocatalysts, and provide a new path to fabricate heterostructural materials for photocatalytical applications.

The light-absorption properties and photocatalytic characteristics were studied for the TiO_2/CdS heteroarchitectures. Su et al.[113] fabricated electrospun nanofibers of TiO_2/CdS heteroarchitectures combining electrospinning technique with hydrothermal process. CdS crystalline particles of ca. 6–40 nm in diameter were uniformly and closely grown on anatase TiO_2 nanofibers. The optical absorption spectra showed that absorption of TiO_2/CdS heteroarchitectures was extended to the visible region.TiO_2/CdS heteroarchitectures possess excellent photocatalytic activity better

than that of the pure TiO_2 nanofibers by the degradation of rhodamine B dye as a model organic substrate under visible-light irradiation.

After introducing the SiO_2 layer the superparamagnetic properties was remained to great extent and the photocatalytic activity towards degradation of rhodamine B (RhB) dye molecules was also significantly improved, as compared to that of the Fe_3O_4@TiO_2 (FT) counterparts. Yu et al.[114] prepared sandwich-like hierarchical porous γ-Fe_2O_3@SiO_2@TiO_2 composite microspheres by an effective three-step approach. This typical structure consists of superparamagnetic γ-Fe_2O_3 nanosphere as inner core, inactive SiO_2 adsorbent as middle layer and photoactive TiO_2 photocatalyst as top coating. Due to enhanced photocatalytic activity for dye decomposition and magnetically separable recycling performance, this novel nanocomposite has potential to design other multifunctional material systems.

Spherical Fe-doped SiO_2/TiO_2 composite nanoparticles well dispersibility were prepared by sol-gel-hydrothermal process. Li et al.[115] studied the photoactivity of Fe-doped SiO_2/TiO_2 composite by the photodecomposition of methylene blue. The composites were characterized by X-ray diffraction (XRD), transmission electron microscope (TEM), thermal gravimetry (TG), X-Ray photoelectron spectroscopy(XPS), and UV-Vis diffuse reflectance spectra (DRS). As a the photoactivity of Fe-doped SiO_2/TiO_2 was lowered, Fe doped SiO_2/TiO_2 composite nanoparticles prepared by sol-gel-hydrothermal method is a promising anti-UV reagent to be used in cosmetics, paint, plastics, and the like.

As the band gap of ZnS is larger than that of ZnO, the luminescence from ZnO could be improved by ZnS coating. Li et al.[116] fabricated ZnS-coated ZnO nanowires by a self-assembling method. Single crystalline nature was confirmed by electron diffraction measurement of the ZnO/ZnS core-shell nanostructure. The photoluminescence (PL) spectra of ZnS-coated ZnO nanostructures showed that the UV emission of nanorods is dramatically enhanced at the expense of the green emission indicating that the ZnS shell with a higher band gap confines the photogenerated carriers inside the ZnO core.

Xu et al.[117] prepared and characterized a composition of nanostructured metal particles on oxide tubes (TiO_2 and ZrO_2). They demonstrated a simple method for fabrication of three dimensional assemblies of gold nanoparticles on TiO_2 and ZrO_2 nanotubes. The composite materials were studied by transmission electron microscopy, scanning electron microscopy, FT-IR absorption, and UV–visible absorption spectra. Results from the characterization of the composites showed that nanoparticle-modified nanotube composites could be used in catalytic, electronic and optical applications.

Kanjwa et al.[118] reported that electrospinning of colloidal solution consisting of titanium isopropoxide/poly(vinyl acetate) zinc nanoparticles was to produce polymeric nanofibers embedding solid nanoparticles. The calcined TiO_2 nanofibers were treated with two chemicals: bis-hexamethylene triamine and zinc nitrate hexahydrate for growing ZnO outgrowths by hydrothermal technique. As anode in lithium ion battery, the nanostructure exhibited a high rate capacity.

Hierarchical ZnS/SiO_2 heterostructures was synthesized via a high-temperature vapor-liquid-solid process. Shen et al.[119] reported that typical hierarchical ZnS/SiO_2 heterostructures were composed of single-crystal ZnS nanowires (core) wrapped with high-density SiO_2 nanowires (branches). A possible growth mechanism was described for the growth of the hierarchical heterostructures and the heterostructures were characterized using X-ray diffraction, scanning electron microscopy and transmission electron microscopy.

The γ-Fe_2O_3/SiO_2 and ε-Fe_2O_3/SiO_2 nanocomposite spheres have the potential to be used as building blocks to fabricate photonic band-gap crystals or threedimensionally ordered innovative materials through self-assembly which are not available in nature. Nakamura et al.[120] developed a facile and novel impregnation method to fabricate highly monodispersed γ-Fe_2O_3/SiO_2 and ε-Fe_2O_3/SiO_2 nanocomposite spheres containing well-dispersed magnetic iron oxide nanoparticles with the use of MMSS hosts. The nanocomposite spheres have exhibited higher monodispersity, better surface smoothness, and better magnetic properties than those prepared by other methods. Characterization was carried out by XRD, SEM and TEM techniques. The magnetic properties of the composite spheres were studied with a vibrating sample magnetometer at room temperature.

Fe_2O_3/SiO_2 nanocomposites based on fumed silica A-300 with iron oxide deposits at different content were synthesized Bogatyrev et al.[121] and his group using Fe(III) acetylacetonate dissolved in isopropyl alcohol or carbon tetrachloride for impregnation of the nanosilica powder at different amounts of Fe(acac)3 then oxidized in air. Characteristics of Fe_2O_3/SiO_2 nanocomposites were studied by using XRD, XPS,

Mossbauer spectroscopy, AFM, nitrogen adsorption, FTIR, TPD MS, TG/DTA, and quantum chemistry methods.

Magnetic mesoporous γ -Fe_2O_3/SiO_2 nanocomposites have great potential to be applied in fields of bioseparation, catalysis, toxin removal, and drug targeting and control release. Wang et al.[122] synthesized magnetic mesoporous γ -Fe_2O_3/SiO_2 nanocomposites by an evaporation-induced self-assembly (EISA) approach. The structural and magnetic properties of the magnetic mesoporous γ -Fe_2O_3 nanocomposites with different content of γ -Fe_2O_3 in composite were studied by XRD, TEM, N_2-sorption, and superconducting quantum interference device (SQUID) magnetometer. The release behaviors of lysozyme from these magnetic porous nanocomposites were also compared.

ZnO/$BaTiO_3$ heterojunction is important for use of semiconductor/ferroelectric heterojunction multifunctional devices. Jia et al.[123] studied X-ray photoelectron spectroscopy of the ZnO/$BaTiO_3$ heterojunction grown by metal-organic chemical vapor deposition. Measured the valence band offset indicates that It indicates that a type-II band alignment forms at the interface, in which the valence and conduction bands of ZnO are concomitantly higher than those of $BaTiO_3$.

He et al.[124] studied photophysical properties and magnetic properties of FMCNPs (fluorescent magnetic composite nanoparticles) and CdTe QDs. FMCNPs and CdTe QDs were synthesized based on a straightforward application of the reverse microemulsion approach at room temperature. Characterizitation of the nanocomposites were carried out by transmission electron microscopy (TEM),

ultraviolet–visible (UV–vis) spectrometry, photoluminescence (PL) spectrometry, and fluorescence microscopy in a magnetic field. FMCNPs with more MNPs and QDs encapsuled in one silica exhibited strong excitonic photoluminescence and superparamagnetic properties. These types of highly stable and luminescent composite nanoparticles could be easily manipulated by an external magnetic field and and detected by using their luminescence. Due to biocompatibility, the nanocomposites are potentially useful for many applications in biolabelling, imaging, drug targeting, bioseparation and bioassays.

The photovoltaic performance of the ZnO/CdS core/shell nanorod arrays were studied by Guerguerian et al.[125] in a PEC system. ZnO/CdS core/shell nanocable architectures were fabricated using the successive ion layer adsorption and reaction (SILAR) technique. Structural, morphological, optical properties and photoelectrochemical (PEC) cell performances of the heterostructures have been studied. The investigation displayed that CdS single-crystalline domains with a mean diameter of about 7 nm are uniformly and conformally covered on the surface of the single-crystalline ZnO nanorods. Optical properties exhibited different well defined absorption edges. A 13-fold enhancement in photoactivity was observed using the ZnO/CdS coaxial heterostructures compared to bare ZnO nanorod.

The photocatalytic hydrogen evolution was investigated by Wang et al.[126] in a gas-closed circulation with vacuum using The Pt nanoparticle loaded ZnO–CdS@Cd heterostructure. They synthesized ZnO–CdS@Cd structure consisting of a metal Cd core and a ZnO–CdS shell, where the CdS shell is directly grown on a Cd core and ZnO nanoparticles as islands are embedded in the CdS shell. Metal Cd core to improve

photoexcited carrier transport at the interface of a ZnO–CdS heterostructure. Hydrogen evolution rate of ZnO–CdS@Cd was high as compared to Pt-loaded ZnO–CdS heterostructure.

How the bandgap, optical absorption, and carrier localization can be controlled by fabricating quantum-well-like and nanowire-based heterostructures of ZnO/ZnS and ZnO/ZnTe was studied Schrier et al.[127]. In the case of ZnO/ZnS core/shell nanowires, which can be synthesized using existing methods applying band-corrected pseudopotential density functional theory calculations. The work demonstrate that the formation of ZnO/ZnS and ZnO/ZnTe nanoheterostructures can reduce the optical band gap while simultaneously maintaining required optical absorption. The results showed that ZnO/ZnS and ZnO/ZnTe nanoheterostructures could be efficient for the creation of photovoltaic devices.

Much faster photoresponse and enhancement in PC and UV PL intensity are obtained from Au/ZnO and Ti/ZnO heterostructures. Dhara et al.[128] reported uniform decoration of metal NPs on the surface of the ZnO NWs by sputtering process and characterization by field emission scanning electron microscopy, high resolution transmission electron microscopy, x-ray diffraction and UV-Vis absorption spectroscopy. The mechanism of photoinduced charge transport and origin of enhanced PC and PL from Au and Ti NPs were investigated. Significant improvement in the band-edge related UV emission and quenching of green occurred for Ti/ZnO and Au/ZnO heterostructures and Ti/ZnO heterostructures shows much faster photoresponse compared to the Au/ZnO.

He et al.[129] investigated enhanced photocatalytic activity of γ-Fe_2O_3@SiO_2@Ce-doped-TiO_2 core–shell nanocomposite capable of magnetic separation. The core-shell nanocomposite photocatalysts were synthesized by a facile sol–gel and after-annealing process and characterized by XRD, XPS, UV-vis spectrophotometer,TEM and vibrating sample magnetometer. Results showed that γ-Fe_2O_3@SiO_2@Ce-TiO_2 hybrid photocatalysts have potentially practical use in wastewater treatment.

To understand the underlying mechanism of the enhanced UV emission and photocatalytic activity of these unique heterostructures, a passible model based on band-gap alignment was proposed by Wu et al.[130] ZnO–ZnS heterostructures were prepared via using ZnO rods as template in different Na_2S aqueous solutions. Characterization were carried out by scanning electronic microscopy (SEM), transmission electronic microscopy (TEM), X-ray diffraction (XRD), energydispersive X-ray analysis (EDX), Fourier transform infrared (FT-IR), and electrochemical impedance spectroscopy (EIS). Electron transfer between ZnS shell and ZnO core strongly affect the photoluminescence and photocatalytic performances of these heterostructures. The heterostructures exhibit enhanced UV emission and improved visible emission.

Gold-capped TiO_2 nanoparticles have been found to improve the efficiency of interfacial charge-transfer process resulting in 40% enhancement in the efficiency of thiocyante oxidation. Dawson et al.[131] reported a simple method for preparing gold-capped TiO_2 nanoparticles in aqueous medium and the morphological changes of the nanocomposite wwre associated with visible laser excitation. The concentration of the

TiO_2 core directlynnnnmnm influences the particle size and the stability of these composite nanoparticles.

ZnO/(La,Sr)CoO_3 core-shell composite nanorod arrays was synthesized by a sequential combination process of a hydrothermal synthesis followed by a pulsed laser deposition (PLD) process (or a colloidal deposition process). Jian et al.[132] studied the structural characteristics and catalysis properties of ZnO/(La, Sr) CoO_3 (ZnO/LSCO) core-shell composite constructs. The surface morphologies and orientations of the composite nanorod arrays are characterized by field-emission scanning electron microscopy (FESEM), transmission electron microscopy (TEM), and X-ray diffraction (XRD). The investigation suggested that these unique composite nanoarchitectures could be a promising candidates for for applications in catalysis, gas sensing, photovoltaics and magnetism.

The core/shell nanostructures having good magnetic properties, which enables their integration into a quartz crystal microbalance (QCM) detection cell with the help of a permanent magnet. Tang et al.[133] synthesized a novel core/shell magnetic nanomaterial $CoFe_2O_4/SiO_2$ which could be used as matrices for the formation, isolation, and physical separation of biorecognition complexes from complex biological mixtures by means of an external magnet. The protein assay system, based on nanometersized magnetic cores and silica shells was used for the detection of cancer antigen 15-3 (CA 15-3, used as a model here) in clinical immunoassays.

Metal Ag was fabricated from Ag_2O using glucose as reducing agent with the growth of the crystalline ZnO. Ye et al.[134] fabricated Silver/zinc oxide (Ag/ZnO) composites

by a facile one-pot synthesis method under hydrothermal conditions. The structural and optical properties were investigated by XRD, SEM, TEM, UV–Vis, and SERS. It was seen that the morphology of the composites was varied with the increased amount of Ag from flower-like to rod-like and finally returned to flower-like. Analysis showed that Ag/ZnO composites exhibit a mixed structure which comprises wurtzite of ZnO and fcc of nanosized Ag and the addition of silver has great effects on the UV–Vis and Raman spectra. The synthesis procedure demonstrated in this report was a simple and effective way to synthesis other similar composites with special morphology for application in various fields.

The conductance of the ZnO/CdS composites showed an enhancement compared with that of the uncoated ZnO nanorod and this enhancement could be attributed to the interaction between the two semiconductors of ZnO and CdS. Gao et al.[135] studied the optical Properties, and electrical Properties of Core/Shell-type ZnO nanorod/CdS nanoparticle composites synthesized by ultrasonic irradiation of a mixture of single crystalline ZnO nanorods, cadmium chloride, and thiourea in an aqueous medium. Transmission electron microscopy images of the ZnO/CdS composites reveal that the ZnO nanorods are coated with CdS nanoparticles. ZnO/CdS composites showed an ultraviolet emission peak at 376 nm and a green emission around 523 nm. Furthermore, ZnO/CdS composites were used as ethanol sensors offering promising opportunities for the design and fabrication of new optoelectronic devices such as highly sensitive gas sensors.

Nanosized Mn_2O_3 particles were incorporated in ordered graphitic mesoporous carbon (OGMC) with a well controlled homogeneous insertion in the carbon matrix. Zhang et al.[136] the electrochemical properties of the Mn_2O_3–carbon nanocomposites in an

aqueous electrolyte under different scan rates. Mn_2O_3–carbon composite materials weresynthesized via a simple self-controlled redox deposition process under neutral pH conditions. The electrochemical performance of the composite material was significantly improved because of the contribution of pseudocapacitance and homogeneous dispersion of the nano-sized transition metal oxide together with the tailored carbon nanostructure. Investigation showed that templated mesoporous carbon with layered graphene domains holds a great promise for high-rate supercapacitor applications.

TiO_2/SiO_2 nanocomposite decomposed the stains through monitoring the discolouring rate of coffee stains on pristine and treated wool samples and water absorption behaviour of treated samples was analysed based on the water droplet contact angle. Pakdela et al.[137] reported that wool fabrics were treated with TiO_2/SiO_2 nanocomposites through a low temperature sol–gel method using the dip-pad-dry-cure process. TiO_2/SiO_2 nanocomposites were synthsized taking different ratio of TiO_2 and SiO_2. Characterization were performed by XRD, FTIR, Attenuated total reflectance(ATR) and SEM. Fabrics functionalised with TiO_2/SiO_2 30:70 showed the highest efficiency in stain removal.

Photocatalytic hydrogen evolution from water using TiO_2/ZnS/CdS composites was reported by Stengl et al.[138] The composite were prepared by homogeneous hydrolysis of aqueous solutions mixture of $TiOSO_4$, $ZnSO_4$, and $CdSO_4$ with thioacetamide. XRD, SEM, BET and UV-vis diffuse reflectance spectroscopy were employed to characterize TiO_2/ZnS/CdS nanocomposites. photocatalytic activity were tested by the degradation of Orange II dye in an aqueous slurry under UV irradiation at 365nm

wavelength and visible light up to 400nm wavelength. Hydrogen was generated from water in the presence of palladium and platinum nanoparticles deposited on TiO_2/ZnS/CdS composites.

Sol-gel method is employed for the preparation of TiO_2/Fe_3O_4 particles consisting of TiO2 nanoparticles and Fe3O4 magnetic cores. Yuxianga et al.[139] studied The photocatalytic activity of the nano TiO_2/Fe_3O_4 composite particles by degrading methyl blue solution under UV illumination. X-ray diffraction, transmission electron microscopy, and vibration sample magnetometry were used to characterize the TiO_2/Fe_3O_4 particles. To keep the composite particles with both photocatalytic efficiency and magnetism at a high level, the optimum molar ratio of TiO_2 to Fe_3O_4 is about 8. Photocatalytic activity of the materials after repeated utilization was tested which is effective in purifying waste water.

Photocatalytic activity of cadmium sulphide–zinc sulphide (CdS·ZnS) nanocomposites was monitored for the evolution of hydrogen during visible-light mediated splitting of water. Deshpande et al[140]. explored a relationship between the physico-chemical properties and catalytic activity of cadmium sulphide–zinc sulphide (CdS·ZnS) nanocomposites for production of hydrogen by photo-splitting of water. by HRTEM and XPS studies revealed that CdS and ZnS moieties exist in a close contact with each other, giving rise to the generation of CdS_{1-x} Zn_xS solid solutions at interfaces that may have a distorted lattice structure. It was investigated from XRD and XPS studies showed the nanocomposites were comprised of the face-centered cubic (α) phases of both CdS and ZnS in a close contact with each other. From UV-

vis spectra a blue shift was observed in the spectrum of CdS on addition of ZnS, in conformation with the quantum size effects.

Cobalt ferrite nanoparticles ($CoFe_2O_4$) were prepared via a solution phase colloidal route and then stabilized in solution using the amphiphilic diblock copolymer, poly(acrylic acid)-*b*-poly(styrene) (PAA-PS). Dai et al.[141] demonstrated that self-assembled ferrimagnet-polymer composite was suitable as a magnetic recording media. Read/write cycles were carried out using a contact magnetic tester and result showed that the FMNP-polymer composite was suitable as a self-assembled magnetic recording media. The nanoparticle-polymer complex was spin-coated onto a silicon substrate to afford self organized thin film arrays which was exposed to an external magnetic field while simultaneously heated above the glass transition temperature of poly(styrene) to allow the nanoparticles to physically rotate to align their easy axes with the direction of the magnetic field.

Embden et al.[142] investigated the effects of core size and shell thickness on the optical properties of CdSe/CdS heterostructure nanocrystals. Thick wurtzite CdS shell on a wide range of CdSe core sizes with monolayer control of shell thickness was grown by a reliable reproducible method. HRTEM verification showed that thick CdS shell growth across a range of CdSe core sizes. HRTEM investigations also demonstrated a strong link between the core/shell dimensions and their optical response and their band-edge transition energies, quantum yields, and excited state lifetimes was established.

The CdS(bulk)/TiO_2 composite photocatalyst photocatalyst could be applied where simultaneous hydrogen production and H_2S removal are desired. Jang et al.[143] reported that CdS–TiO_2 nano-bulk composite (NBC) photocatalyst exhibited extremely high rates of hydrogen production from decomposition of water containing Na_2S/Na_2SO_3 as sacrificial agents and also showed very high activity of hydrogen production from a more practical system of H_2S dissolved in NaOH solution under visible light irradiation. The CdS(bulk)/TiO_2 composite photocatalyst was synthesized by a precipitation method and sol–gel method.

Superparamagnetic behaviour of γ-Fe_2O_3/SiO_2-coated nanocomposites was studied by superconducting quantum interference device magnetometry and Mo¨ssbauer spectroscopy. This nanocomposites are promising candidates for magneto-optical applications. Zhang et al.[144] reported that magnetic and electronic properties of the nanocomposites were controlled and tailored by the interface between the nanoclusters and the host matrix. γ-Fe_2O_3 /SiO_2-coated nanocomposites were synthesized by coprecipitation of ferrous and ferric salts encapsulated within sol-gel derived silica (SiO_2) and displayed a spherical morphology. SiO_2 coating provides a means for thermally stable dispersion of Fe_2O_3 clusters. UV-vis spectra showed that the absorption edge of the nanocomposites to be slightly blue shifted and it was attributed to the combined effects of the quantum confinement of the nanocrystalline γ-Fe_2O_3 clusters and the stress present at the particle/support interface.

ZnO–Ag is a potential nanocomposite material for the UV light emission and for the development of nonlinear optical devices. Irimpan et al.[145] studied the spectral and nonlinear optical properties of ZnO–Ag nanocomposites. ZnO–Ag nanocomposites

were prepared through colloidal chemical synthesis. The optical absorption spectra of the nanocomposite showed a gradual shift in absorbance towards the visible region. Photoluminescence spectra showed that ultraviolet (UV) emission was enhanced and was three times than that of pure ZnO. These nanocomposites exhibited self-defocusing nonlinearity and good nonlinear absorption behaviour which increases with increasing Ag volume fraction.

Zhu et al.[146] studied the photocatalytic activity of CdS/TiO_2 nanocomposites by measuring the degradation of methylene blue (MB) under visible light irradiation. The CdS/TiO_2 nanotubes composites were prepared by a facile chemical reduction method. Composites were characterized by TEM, HRTEM, XRD, XPS, FTIR and UV-vis spectroscopy. Optical study showed that the presence of CdS nanoparticles can extend the absorption edge to visible region at about 540 nm, together with the high specific area of TiO_2 nanotubes.

ZnO–RGO composites exhibited an enhanced photocatalytic performance in reduction of Cr(VI) under UV light irradiation as compared with pure ZnO due to the increased light absorption intensity and range as well as the reduction of electron–hole pair recombination in ZnO with the introduction of RGO. Liu et al.[147] synthesized ZnO–reduced graphene oxide (RGO) composites via UV-assisted photocatalytic reduction of graphite oxide by ZnO nanoparticles in ethanol. Characterizitation of the composite were carried out by scanning electron microscopy, transmission electron microscopy, atomic force microscopy, X-ray diffraction spectroscopy, UV–vis absorption spectrophotometer. ZnO nanoparticles were decorated on the RGO nanosheets.

Due to large surface area, high redox potential of the photogenerated charge carriers, and selective reduction/oxidation of different classes of organic compounds, nanostructured colloidal semiconductors with heterogeneous photocatalytic behavior have drawn considerable attention of the researchers. Srinivasan et al.[148] studied the structural,microstructural, UV-Vis spectral characteristics and visible light photocatalytic behaviour of CdS-TiO_2 nanocomposite. Pure TiO_2, pure CdS and CdS coupled TiO_2 nanocomposite were synthesized by employing reverse micelle process. UV-Vis spectra showed that the surface-coated CdS and TiO_2 anatase nanocomposite extends the absorption band edge in the visible region. CdS-TiO_2 nanocomposite materials showed better photocatalytic activity than that of pure TiO_2.

Titanate nanotube/anatase nanoparticle composites nanocomposites exhibited enhanced photocatalytic activity compared to titanate nanotube, anatase TiO_2 nanoparticle, and even the commercial Degussa P-25. Yan et al.[149] studied the photocatalytic activity of the Titanate/anatase nanocomposites by photocatalytic decolorization of rhodamine B under visible light irradiation. Titanate nanotube/anatase nanoparticle composites were synthesized via a novel combinational hydrothermal method.

CdS/TiO_2 nanocomposites can degrade Acid Rhodamine B under visible light irradiation and showed high photocatalytic activity with a mass ratio of 4:1(TiO_2:CdS). Bai et al.[150] prepared CdS/TiO_2 nanocomposites via a simple wet chemical method, and characterized through X-ray diffraction (XRD) and transmission electron microscopy (TEM). Furthermore, the photocatalytic activity of the CdS/TiO_2

catalysts can be enhanced by controlling the CdS nanoparticle dispersion on TiO_2 nanotube surface.

The nanocomposite with CdS and TiO_2 in the molar ratio of 0.25:1 exhibited the highest photocatalytic activity under visible light irradiation that could be attributed to excellent crystallinity, high specific surface area, large pore volume and strong absorption in the visible light region of that particular nanocomposite. Shi et al.[151] prepared CdS/TiO_2 composites with better crys-tallinity with a hydrothermal reaction at 180 ◦C for 6 h. Composites were fabricated by four different synthesis ruote. The photocatalytic activities of these prepared samples were examined by the degradation of rhodamine B and methyl orange under visible light irradiation, respectively.

Hydrogel–silver nanocomposites was synthesized by a unique methodology, which involves formation of silver nanoparticles within swollen poly (acrylamide-*co*-acrylic acid) hydrogels. Thomas et al.[152] studied antibacterial effects on Escherichia coli (E. coli) of the nanocomposites. It was investigated that immersion of plain hydrogel in 20 mg/30 ml $AgNO_3$ solution yielded nanocomparticle–hydrogel composites with optimum bactericidal activity. The antibacterial activity ascribed to size of the nanocomposites, amount of silver nanoparticles, and amount of monomer acid present within the hydrogel–silver nanocomposites.

Study of magnetic property of MFeCMS reveals that the room-temperature magnetization curve shows a large magnetic hysteresis loop, which depicts the strong magnetic response to a varying magnetic field. Zhao et al.[153] fabricated magnetic core/mesoporous silica shell (MFeCMS) nanospheres with uniform particle diameter.

The mesoporous silica shell on magnetic core was formed from simultaneous sol-gel polymerization of tetraethoxysilane and *n*-octadecyltrimethoxysilane. Ibuprofen, a typical anti-inflammatory drug was introduced into the pores of MFeCMS and most of the drug molecules incorporated can be released to the SBF in 70 h. This material has potential application in targeted drug delivery and multiphase separation.

In vitro bactericidal activity of porous TiO_2-Ag composite against methicillin-resistant Staphylococcus aureus was studied by Necula et al.[154] Bactericidal coating was produced on a titanium medical alloy Ti–6Al–7Nb using a plasma electrolytic oxidation process performed in an calcium acetate/calcium glycerophosphate electrolyte bearing Ag nanoparticles. Ag associated with particles distributed on the porous oxide surface was observed by SEM-EDS analysis. The coating was characterized with respect to surface morphology, chemical composition, roughness, wettability. The investigations showed a complete killing of MRSA inocula within 24 h, even in the presence of 50% human serum, while oxidized titanium in the absence of Ag nanoparticles showed a 1000-fold increase in bacteria CFU.

Photo-antibacterial activity of the nanocomposite film exposed by the solar light was better than activity of the Ag/a-TiO_2 and a-TiO_2, respectively. Akhavan et al.[155] studied the photodegradation of Escherichia coli bacteria in presence of Ag–TiO_2/Ag/a-TiO_2 nanocomposite film with an effective storage of silver nanoparticles in the visible and the solar light irradiations. The nanocomposite film was synthesized by sol–gel deposition. X-ray photoelectron spectroscopy (XPS) and scanning electron microscopy (SEM) analyses proved the self-accumulation of Ag nanoparticles on the film surface.

Antibacterial activity of Ag/MMT/Cts bionanocomposites against Gram-positive bacteria, ie, Staphylococcus aureus and methicillin-resistant S. aureus and Gram-negative bacteria (ie, Escherichia coli) by the disk diffusion method on Muller–Hinton Agar at different sizes of Ag-NPs was studied by Shameli et al.[156] Silver nanoparticles were prepared via a green physical synthetic route into the lamellar space of montmorillonite (MMT)/chitosan (Cts) utilizing the ultraviolet (UV) irradiation method in the absence of any reducing agent or heat treatment. Ag/MMT/Cts BNCs were characterized by powder X-ray diffraction, transmission electron microscopy, scanning electron microscopy, energy dispersive X-ray fluorescence, Fourier transform infrared, and UV-visible spectroscopy. MMT/Cts BNCs can be useful in different biologic research and biomedical applications.

Gas sensor properties of the core–shell nanospindles are significantly enhanced compared to pristine α-Fe_2O_3 which was attributed to the unique core–shell nanostructure. Zhang et al.[157] investigated the gas sensing performances of α-Fe_2O_3@ZnO core–shell nanocomposite using ethanol as the main probe gas. α-Fe_2O_3@ZnO core shell nanospindles were fabricated via a two-step hydrothermal approach. Energy band structure and the electron depletion theory was employed to understand Sensing mechanism.

Plasma sprayed nano-titania/silver coatings were deposited on titanium substrates to fabricate an implant material having excellent antibacterial property. Li et al.[158] studied the bioactivity of nano-titania/silver coatings by simulated body fluid soaking test. Nano-titania/silver coatings were characterized by scanning electron microscopy,

energy dispersive spectrometer, optical emission spectrometry and X-ray diffraction. The antibacterial activity of the material was tested by bacterial counting method against Escherichia coli. Due to good bioactivity, cytocompatibility and antibacterial property, which made nano-titania/silver coatings promising candidate to be applied in hard tissues replacement against postoperative infections.

The nano-sized coupled oxides ZnO/SnO_2 thin films in different molar ratios of were prepared using sol–gel dip coating method. Talebiana et al.[159] reported bactericidal activities of nanostructured ZnO and SnO_2 films as well as $ZnO:SnO_2$ composite films in killing of Gram-negative bacteria, E. coli. Composite was characterized with X-ray diffraction (XRD), scanning electron microscopy (SEM) and UV–vis spectroscopy. The bactericidal activity was estimated by relative number of bacteria survived calculated from the number of viable cells which form colonies on the nutrient agar plates applying the so-called antibacterial drop test under UV illumination.

Matai et al.[160] prepared silver–zinc oxide(Ag–ZnO) nanocomposites of varied molar ratios having broad-spectrum antibacterial activity against Gram-positive and Gram-negative bacteria by simple microwave assisted reactions in the absence of surfactants. The crystalline behavior, composition and morphological analysis of the nanocomposite were evaluated by X-ray diffraction, infrared spectroscopy, field emission scanning electron microscopy (FE-SEM), atomic absorption spectrophotometry (AAS) and transmission electron microscopy (TEM). The minimum inhibitory concentration (MIC)and minimum killing concentration (MKC) of the nanocomposite were investigated by visual turbidity analysis and optical density analysis. Qualitative

and quantitative assessments of antibacterial effects were obtained by fluorescent microscopy, fluorescent spectroscopy and Gram staining measurements.

Nanostructured sol-gel TiO_2-Ag have a bactericide effect including highly pathogenic bacteria such as EPEC and MRSA even more than conventional bactericides with the advantage of suitability for repeated use with potential to surface application. Goerne et al.[161] studied bacterial sensitivity of silver nanoparticles highly dispersed over nanostructured titania. Ag-TiO_2 nanoparticles showed sensibility several Gramnegative and Gram-positive bacteria including enterophatogenic Escherichia coli and highly resistant strains such as methicillin-resistant Staphylococcus aureus.

1.4 Scope of this thesis:

In this work, we have provided an overview of the facile synthesis of heterostructured nanocomposites and their important applications. We have also engineer their morphology to get diversity in their properties and applications. The morphological modification of nanocomposites which introduces additional functionality to the nanocomposites, has led to them gaining increasing interest for a wide range of applications. Particular attention has been devoted to synthesis of the nanocomposites. The facile wet chemical synthesis of nanocomposites using less toxic and readily available precursors, as well as environmentally benign solvents or supports, under ambient conditions was described. Different properties such as optical, magnetic, photocatalytic and antibacterial properties were extensively studied.

We propose a novel method to to combine individual components in such a fashion so that self assembled unique nanostructures of CdS-ZnO (CZ1:1, CZ1:2 and

CZ1:3), Co_3O_4-ZnO nanocomposites have been synthesized. Simple chemical route is adopted for the growth of these novel nanocomposites and structural, chemical and morphological details of the specimen has been studied. The growth mechanism of the composite structures with is delineated with oriented attachment self assemble techniques. Absorption and emission properties of the nanocomposites have been investigated. Photocatalytic activity of CdS/ZnO nanocomposites with varying morphology and Co_3O_4-ZnO nanocomposite were explored for the degradation of rhodamine B dye in presence of visible light irradiation. The results reveal that the best catalytic performance arises in CdS/ZnO composite with 1: 1 ratio. The sample shows high photocatalytic activity employing effective charge transfer between two coupled semiconductors. The antibacterial efficiency of CZ1:1, CZ1:2 and CZ1:3 nanocomposites were investigated on pathogenic microorganisms without light irradiation and results showed significant antibacterial activity in CdS/ZnO composite with 1:3 ratio. Overall, CdS/ZnO and Co_3O_4-ZnO nanocomposites excel in different potential applications, such as visible light photocatalysis and antimicrobial activity with their tuneable structure. Although remarkable progress has been made with these nanocomposites, further work is needed to discover other new and advanced applications for these nanocomposites, such as for Green Chem., and envi-ronmentally sustainable protocols.

The take-home message from our work is that new Nanotechnology is breathing new life into the design and preparation of well-defined heterostructured nanocomposites with highly desirable properties and applications. By combining these new self-assembly syntheses, it should prove possible to develop a new generation of highly functional material in the future.

REFERENCES

1. G. L. Hornyak, H. F. Tibbals, J. Dutta, J. J. Moore, "Introduction to Nanoscience & Nanotechnology", Publisher Taylor & Francis group, Chap 1, 1-54 (2009).
2. J. C. Glenn, Technol. Forecast. Soc. 73, 128 (2006).
3. S. K. Sahoo, S. Parveen, J. J. Panda, Nanomedicine: Nanotechnology, Biology, and Medicine 3, 20 (2007).
4. J. Corbett, P. A. McKeown, G. N. Peggs, R. Whatmore, Nanotechnology: international development and emerging products. CIRP Annals – Manufacturing Technology 49, 523 (2000).
5. R. Lane, B. Craig, W. Babcock, AMPTIAC 6, 31 (2002).
6. Nanoscale Materials in Chemistry (Klabunde, K. J., Editor). Chapter 4. Wiley, New York, 2001.
7. D. L. Leslie-Pelecky, R. D. Reike, Chem. Mater. 8, 1770 (1996).
8. J. Y. Ying, T. Sun, J. Of Electroceramics 1, 219 (1997).
9. C. C. Koch, Annual Review of Mater. Sci. 19, 121 (1989).
10. C. Suryanarayana, Progr. Mater. Sci. 46, 1 (2001).
11. I. Kerr, G. Creston, Metal powder report, 48, 36 (1993).
12. P. G. McCormick, Mater. Trans. Jpn. Inst. Metals 36, 161 (1995).
13. W. Marine, L. Patrone, B. Luk'yanchuk , M. Sentis, Appl. Surf. Sci. 345, 154 (2000).

14. M. Saito, K. Yasukawa, Opt. Mater. 30 1201 (2008).
15. R. G. Song, M. Yamaguchi, Appl. Surf. Sci. 253, 3093 (2007).
16. D. Kim, D. Jang, Appl. Surf. Sci. 253, 8045 (2007).
17. M. Muniz-Miranda, C. Gellini and E. Giorgetti, J. Phys. Chem. C 115, 5021 (2011).
18. J. Lee, D.-K. Kim, W. Kang, Bull. Korean Chem. Soc. 27, 1869 (2006).
19. J. S. Benjamin, E. Arzt, L. Schultz (DGM Information gesellschaft, Oberursel, Germany,), New Materials by Mechanical Alloying Techniques, 3 (1989).
20. V. P. Dravid, J. J. Host, M. H. Teng, B. Elliott, J. H. Hwang, D. L. Johnson, T. O. Mason, J. R. Weert-man, Nature 374, 602 (1995).
21. P. J. F. Harris, S. C. Tsang, Carbon 36, 1859 (1998).
22. W.Z.Wu, Z.P. Zhu, Z.Y. Liu, Y.I. Xie, J. Zhang, T. D. Hu, Carbon 41, 317 (2003).
23. C. P. Chen, T. H. Chang, T. F. Wang Ceram. Int. 28, 925 (2002).
24. P. M. Ajayan, Chem. Rev. 99, 1787 (1999).
25. Y. H. Wang, S. C. Chiu, K. M. Lin, Y. Y. Li, Carbon 42, 2535 (2004).
26. H. Kajiura, H. J. Huang, S. Tsutsui, Y. Murakami, M. Miyakoshi, Carbon 40, 2423 (2002).
27. Z. Osvath, A. A. Koos, Z. E. Horvath, J. Gyulai, A. M. Benito, M. T. Martinez, W. Maser, L. P. Biro, Mater. Sci. Eng. C 23, 561 (2003).
28. E. Pérez-Tijerina, M. Gracia Pinilla, S. Mejía-Rosales,U. Ortiz-Méndez, A. Torres, M. José-Yacamán, Faraday Discuss 138, 353 (2008).
29. W. Han, D. Nana, L. Rufeng, Z. Bei, Rare Metal Materials and Engineering 44, 164 (2015).

30. S. G. Pandya, M. E. Kordesch**,** Nanoscale Research Letters 10, 258 (2015).
31. A. Tasaki, S. Tomiyama, S. Iida, N. Wada, R. Uyeda, J. Appl. Phys. 4, 707 (1965).
32. C. G. Granqvist, R. A. Buhrman, J. Appl. Phys. 47, 2200 (1976).
33. Birringer, R., Gleiter, H., Klein, H. P. and Marquardt, P., Phys. lett. A 102, 365(1984).
34. B. H. Kear, P. R. Strutt, Nanostruct. Materials 6, 227–236 (1995).
35. P. John, S. J. Moss, A. Ledwith, In The Chemistry of the Semiconductor Industry, Eds.; Chapman and Hall: New York, (1987).
36. M. L. Hitchman, K. F. Jensen(Eds.), Chemical Vapor Deposition, Academic Press (1993).
37. C. L. Bowes, A. Makek, G. A. Ozin, Chem. Vap. Deposition 2, 97 (1996).
38. T.Kyotani, L.-F. Tsai, A.Tomita, Chem. Mater. 8, 2109 (1996).
39. T. Kyotani, T. Nagai, S. Inoue, A.Tomita, Chem. Mater. 9, 609 (1997).
40. G. Che, B. B. Lakshmi, C. R. Martin, E. R. Fisher, Chem. Mater. 10, 260 (1998).
41. W. Z. Li, S. S. Xie, L. X. Qian, B. H. Chang, B. S. Zou, W. Y. Zhou, R. A. Zhao, G.Wang, Science 274, 1701 (1996).
42. E. Moreau, S. Godey, F. J. Ferrer, D. Vignaud, X. Wallart, J. Avila, M. C. Asensio, F. Bournel, J-J Gallet, Appl. Phys. Lett. 97 241907 (2010).
43. G. Lippert, J. Dabrowski, Y. Yamamoto, F. Herziger, J. Maultzsch, J. Baringhaus, C. Tegenkamp, M. C. Lemme, W. Mehr, G. Lupina, Phys. Status Solidi 249, 2507 (2012).

44. A.Fontcuberta i Morral, C. Colombo, and G. Abstreiter, Applied Physics Letters 92, 063112 (2008).
45. K. Kawaguchi, R. Kita, M. Nishiyama, T. Morishita, J. Cryst. Growth 143, 221 (1994).
46. D. S. Darvish, H. A. Atwater, J. Cryst. Growth 319, 39 (2011).
47. J. Li, Z. Mei, D. Ye, H. Liang, Y. Liu, X. Du, J. Cryst. Growth 353, 63 (2012).
48. C. Thelander, Appl. Phys. Lett. 83, 2052 (2003).
49. M. T. Bjork, Appl. Phys. Lett. 81, 458 (2002).
50. F. Castro, S. Kuhn, K. Jensen, A. Ferreira, F. Rocha, A. Vicente, J.A. Teixeira, Chem. Eng. Sci. 100, 352 (2013).
51. V. Ström, R.T. Olsson, K.V. Rao, J. Mater. Chem. 20, 4168 (2010).
52. H. Van den Rul, D. Mondelaers, M.K. van Bael, J. Mullens, J. Sol-Gel Sci. Tech. 39, 41 (2006).
53. A. Jones, S. Rigopoulos, R. Zauner, Comput.Chem. Eng. 29, 1159 (2005).
54. A.Mersmann, Chem. Eng. Process. 38, 345 (1999).
55. N. R. Jana, L. Gearheart, C. J. Murphy, Chem. Mater. 13, 2313 (2001).
56. H. Yu, P.C. Gibbons, K.F. Kelton, W. E. Buhro, J. Am. Chem. Soc. 123, 9198 (2001).
57. J.P. Wilcoxon, P.P. Provencio, J. Am. Chem. Soc. 126, 6402 (2004).
58. J. Livage, Science 2, 132 (1997).
59. K. A. Vorotilov, M. I. Yanovskaya, E.P. Turevskaya, A. S. Sigov., Journal of Sol-Gel Science and Technology 16, 109 (1999).
60. L. L Hench, J. K.West, Chemical Review 90, 33 (1990).

61. G. Ennas, A. Mei, A. Musinu, G. Piccaluga, G. Pinna, S.Solinas, Journal of Non-Crystalline Solids 232, 587 (1998).
62. N. Viart, M. Richard-Plouet, D. Muller, G. Pourroy. Thin Solid Films 437, 1 (2003).
63. T. K. Kundu, M. Mukherjee, D. Chakravorty, T. P.Sinha, Journal of Matererials Science 33, 1759 (1998).
64. S. Ananthakumar, A. K. Prabhakaran, U. S. Hareesh, P. Manoharan, Materials Chemistry and Physics 85, 151 (2004).
65. S. Sivakumar, C. P. Sibu, P. Mukundan, P. K. Pillai, K. G. K. Warrier., Materials Letters 58, 2664 (2004).
66. Warrier KGK, Anilkumar GM., Materials Chemistry and Physics. 67(1-3):263-266(2001).
67. N. N. Ghosh, P.Pramanik, Materials Science and Engineering: C 16, 113 (2001).
68. F. Cansell, B. Chevalier, A. Demourgues, J. Etourneau, C. Even, Y. Garrabos, V. Pessey, S. Petit, A. Tressaud, F. Weill, J. Mater. Chem. 9, 67 (1999).
69. M. Rajamathi, R. Seshadri, Curr. Opin. Solid State Mater. Sci. 6, 337 (2002).
70. E. Reverchon, R. Adami, J. Supercrit. Fluid. 37, 1 (2006).
71. J. Yang, G.-H. Cheng, J.-H. Zeng, S.-H. Yu, X.-M. Liu, Y.-T. Qian, J. Yang et al., Chem. Mater. 13, 848 (2001).
72. H. Chen, J. Lee, J. Nanosci. Nanotechno. 10, 629 (2010).
73. V. Amendola, S. Polizzi, M. Meneghetti, J. Phys. Chem. B 110, 7232 (2006).

74. V. V. Namboodiri, R. S. Varma, Green Chem. 3, 146 (2001).

75. S. Komarneni, Curr. Sci. 85 1730 (2003).

76. M. Blosi, S. Albonetti, M. Dondi, C. Martelli and G. Baldi, J. Nanopart. Res. 13, 127 (2011).

77. H.-T. Zhu, C.-Y. Zhang, Y.-S. Yin, J. Cryst. Growth 270, 722 (2004).

78. R. D'Amato,M. Falconieri, S. Gagliardi, E. Popovici, E. Serra, G. Terranova, E. Borsella, Journal of Analytical and Applied Pyrolysis 104, 461 (2013).

79. C. A. Grimes, D. Qian, E. C. Dickey, J. L. Allen, P. C. Eklund, J. Appl. Phys. 87, 5642 (2000).

80. B. David, N. Pizurova, O. Schneeweiss, P. Bezdicka, I. Morjan, R. Alexandrescu, J. Alloys Compd. 378, 112 (2004).

81. F. Dumitrache, I. Morjan, R. Alexandrescu, V. Ciupina, G. Prodan, I. Voicu, C. Fleaca, L. Albu, M. Savoiu, I. Sandu, E. Popovici, I. Soare, Appl. Surf. Sci. 247, 25 (2005).

82. S. Martelli, A. Mancini, R. Giorgi, R. Alexandrescu, S. Cojocaru, A. Crunteanu, I. Voicu, M. Balu, I. Morjan, Appl. Surf. Sci. 154, 353 (2000).

83. Z. Z. Xu, C. C. Wang, W. L. Yang, Y. H. Deng, S. K. Fu, J. Magn. Magn. Mater. 277, 136 (2004).

84. Y. Deng, L. Wang, W. Yang, S. Fu, A. Elaissari, J. Magn. Magn. Mater. 257, 69 (2003).

85. P.Tartaj, J. Tartaj, Chem. Mater. 14, 536 (2002).

86. Santra, S., Tapec, R., Theodoropoulou, N., Dobson, J., Hebard, A., and Tan, W. H., Langmuir 17, 2900 (2001).

87. C. Burda, X., Chen, R. Narayanan, M. A. El-Sayed, Chem. Rev. 105, 1025 (2005).

88. I. Capek, Adv. Colloid Interface Sci. 110, 49 (2004).

89. V. G. Pol, M. Motiei, A. Gedanken, J. CalderonMoreno, Y. Mastai, Chem. Mater. 15, 1378 (2003).

90. R. Vijayakumar, Y. Koltypin, I. Felner, A. Gedanken, Mater. Sci. Eng. A 286, 101 (2000).

91. A. Gedanken, Ultrason. Sonochem. 11, 47 (2004).

92. K. V. P. M. Shafi, A. Ulman, X. Z. Yan, N. L. Yang, C. Estournes, H. White, M., Rafailovich, Langmuir 17, 5093 (2001).

93. H. Khalil, D. Mahajan, M. Rafailovich, M. Gelfer, K. Pandya, Langmuir 20, 6896 (2004).

94. K. S. Suslick, G. J. Price, Annu. Rev. Mater. Sci. 29, 295 (1999).

95. T. Mokari, C.G. Sztrum, A. Salant, E. Rabani, U. Banin, Nat. Mater. 4, 855(2005).

96. Pulickel M. Ajayan, Linda S. Schadler, Paul V. Braun, Science and Technology; Wiley & Sons: New York, (2003).

97. D. Y. Godovsky, AdV. Polym. Sci. 153, 163 (2000).

98. H. K.Schmidt, E. Geiter, M. Menning, H. Krug, C. Becker, R. P. Winkler, J. Sol.-Gel Sci. Technol. 13, 397 (1998).

99. F. Caruso, AdV. Mater. 13, 11 (2001).

100. G. Liu, G. Li, Xiaoqing Qiu, L. Li, Journal of Alloys and Compounds 481, 492 (2009).

101. S. Vaidya, A. Patra, A. K. Ganguli, J. Nanopart. Res. 12, 1033 (2010).

102. K. Aslan, M. Wu, J. R. Lakowicz, C. D. Geddes, J. Am. Chem. Soc. 129, 1524 (2007).

103. J. Wang, Y. Liu, Y. Jiao, F. Qu, Q. Pan, X. Wu, Journal of Nanomaterials Article ID 684797 (2013).

104. J. Nayak, S. N. Sahu, J. Kasuya, S. Nozaki, Applied Surface Science 254, 7215 (2008).

105. C. Shi, Y. Shan, J. Xu, H. Chen, Electrochimica Acta, 8268 (2010).

106. K-S Chou, C-C Chen, Microporous and Mesoporous Materials 98, 208 (2007).

107. B. Cheng, Y. Le, J. Yu, Journal of Hazardous Materials 177, 971(2010).

108. X. Wang, X. Kong, Y. Yu, H. Zhang, J. Phys. Chem. C 111, 3836 (2007).

109. D. Barpuzary, Z. Khan, N. Vinothkumar, M. De, M. Qureshi, J. Phys. Chem. C 116, 150 (2012).

110. P. Kundu, P. A. Deshpande, G. Madras, N. Ravishankar, J. Mater. Chem. 21, 4209 (2011).

111. K. Vinodgopal, Idriss Bedja, and Prashant V. Kamat, Chem. Mater., 8, 2180-2187(1996).

112. W. Wu, S. Zhang, X. Xiao, J. Zhou, F. Ren, L. Sun, C. Jiang, ACS Appl. Mater. Interfaces 4, 3602 (2012).

113. C. Su, C. Shao, Y. Liu, Journal of Colloid and Interface Science 359, 220 (2011).

114. X. Yu, S. Liu, J. Yu, Applied Catalysis B: Environmental 104, 12 (2011).

115. Z. Li, B. Hou, Y. Xu, D. Wu, Y. Sun, Journal of Materials Science 40, 3939 (2005).

116. J. Li, D. Zhao, X. Meng, Z. Zhang, J. Zhang, D. Shen,Y. Lu, X. Fan, J. Phys. Chem. B 110, 14685 (2006).

117. J-Z Xu, W-B Zhao, J-J Zhu, G-X Li, H-Y Chen, Journal of Colloid and Interface Science 290, 450 (2005).

118. M. A. Kanjwa, N. A. M. Barakat, F. A. Sheikh, H. Y. Kim, Bioceramics Development and Applications, 1, Article ID D1101293 (2011).

119. G. Shen, Y. Bando, C. Tang, D. Golberg, J. Phys. Chem. B 110, 7199 (2006).

120. T. Nakamura,Y. Yamada, K. Yano, J. Mater. Chem. 16, 2417 (2006).

121. V.M. Bogatyrev, V.M. Gun'ko, M.V. Galaburda, M.V. Borysenko, V.A. Pokrovskiy, O.I. Oranska, E.V. Polshin, O.M. Korduban, R. Leboda, J. Skubiszewska-Zieba, Journal of Colloid and Interface Science 338, 376 (2009).

122. Y. Wang, J. Ren, X. Liu, Y. Wang, Y. Guo, Y. Guo, G. Lu, Journal of Colloid and Interface Science 326, 158 (2008).

123. C.H. Jia, Y.H. Chen, X.L. Zhou, A.L. Yang, G.L. Zheng, X.L. Liu, S.Y. Yang, Z.G.Wang, Appl. Phys. A 99, 511 (2010).

124. R. He, X. You, J. Shao, F. Gao, B. Pan, D. Cui, Nanotechnology, 18, 315601 (2007).

125. G. Guerguerian, F. Elhordoy, C. J. Pereyra, R. E. Marotti, F. Mart´ın, D. Leinen, J. Ramos-Barrado, E. A. Dalchiele, Nanotechnology 22, 505401 (2011).

126. X. Wang, G. Liu, L. Wang, Z-G Chen, G. Qing (Max) Lu, H-M Cheng, Adv. Energy Mater. 2, 42 (2012).

127. J. Schrier, D. O. Demchenko, L-W Wang, Nano Lett. 7, 2377 (2007).

128. S. Dhara, P. K. Giri, Journal of applied physics 110, 124317 (2011).

129. M. He, D. Li, D. Jiang, M. Chen, Journal of Solid State Chemistry 192, 139 (2012).

130. D. Wu, Y. Jiang, Y. Yuan, J. Wu, K. Jiang, J. Nanopart. Res. 13, 2875 (2011).

131. A. Dawson, P. V. Kamat, J. Phys. Chem. B 105, 960 (2001).

132. D. Jian, P-X Gao, W. Cai, B. S. Allimi, S. P. Alpay, Y. Ding, Z. L. Wang, C. Brooks, J. Mater. Chem. 19, 970 (2009).

133. D. Tang, R. Yuan, Y. Chai, H. An, Adv. Funct. Mater. 17, 976 (2007).

134. X-Y Ye, Y-M Zhou, Y-Q Sun, J. Chen, Z-Q Wang, J. Nanopart. Res. 11,1159 (2009).

135. T. Gao, Q. Li, T. Wang, Chem. Mater. 17, 887 (2005).

136. L. L. Zhang, T. Wei, W. Wang, X.S. Zhao, Microporous and Mesoporous Materials 123, 260 (2009).

137. E. Pakdela, W. A. Daoudb, X. Wang, Applied Surface Science 275, 397 (2013).

138. V. Stengl, D. Kralova, International Journal of Photoenergy, Volume 2011, Article ID 532578 (2011).

139. L. Yuxianga, Z. Meia, G. Mina, W. Xidong, Rare Metals 28, 423 (2009).

140. A. Deshpande , P. Shah, R.S. Gholap, N. M. Gupta, Journal of Colloid and Interface Science 333, 263 (2009).

141. Q. Dai, D. Berman, K. Virwani, J. Frommer, P-O Jubert, M. Lam, T. Topuria, W. Imaino, A. Nelson, Nano Lett. 10, 3216 (2010).

142. J. Embden, J. Jasieniak, P. Mulvaney, J. Am. Chem. Soc. 131, 14299 (2009).

143. J. S. Jang, H. G. Kim, P. H. Borse, J. S. Lee, International Journal of Hydrogen Energy 32, 4786 (2007).

144. L. Zhang, G. C. Papaefthymiou, J. Y. Ying, J. Appl. Phys. 81, 6892 (1997).

145. L. Irimpan, V.P.N. Nampoori, P. Radhakrishnan, Chemical Physics Letters 455, 265 (2008).

146. J. Zhu, D. Yang, J. Geng, D. Chen, Z. Jiang, J. Nanopart. Res. 10, 729 (2008).

147. X. Liu, L. Pan, Q. Zhao, T. Lv, G. Zhu, T. Chen, T. Lu, Z. Sun, C. Sun, Chemical Engineering Journal 183, 238 (2012).

148. S. S. Srinivasan, J. Wade, E. K. Stefanakos, Journal of Nanomaterials, Volume 2006 Article ID 87326, 1 (2006).

149. Y. Yan, X. Qiu, H. Wang, L. Li, X. Fu, L. Wu, G. Li, Journal of Alloys and Compounds 460, 491 (2008).

150. S. Bai, H. Li, Y. Guan, S. Jiang, Applied Surface Science 257, 6406 (2011).

151. J. Shi, X. Yan, H.-J. Cui, X. Zong, M.-L. Fu, S. Chen, L. Wang, Journal of Molecular Catalysis A: Chemical 356, 53 (2012).

152. V. Thomas, M. M. Yallapu, B. Sreedhar, S.K. Bajpai, Journal of Colloid and Interface Science 315, 389 (2007).

153. W. Zhao, J. Gu, L. Zhang, H. Chen, J. Shi, J. Am. Chem. Soc. 127, 8916 (2005).

154. B. S. Necula, L. E. Fratila-Apachitei, S. A. J. Zaat, I. Apachitei, J. Duszczyk, Acta Biomaterialia, 5, 3573 (2009).

155. O. Akhavan, Journal of Colloid and Interface Science 336, 117 (2009).

156. K. Shameli, M. B. Ahmad, W. M. Z. W. Yunus, A. Rustaiyan, N. A. Ibrahim, M. Zargar,Y. Abdollahi, International Journal of Nanomedicine 5, 875 (2010).

157. J. Zhang, X. Liu, L. Wang, T. Yang, X. Guo, S. Wu, S. Wang, S. Zhang, Nanotechnology 22, 185501 (2011).

158. B. Li, X. Liu, F. Meng, J. Chang, C. Ding, Materials Chemistry and Physics 118, 99 (2009).

159. N. Talebiana, M. R. Nilforoushan, E. B. Zargar, Applied Surface Science 258, 547 (2011).

160. I. Matai, A. Sachdev, P. Dubey, S. U. Kumar, B. Bhushan, P. Gopinath, Colloids and Surfaces B: Biointerfaces, 115, 359–367 (2014).

161. T. M. L. Goerne, M. A. A. Lemus, V. A. Morales, E. G. López, P. C. Ocampo, J. Nanomed. Nanotechol. 5, 003(2012).

CHAPTER 2

SYNTHESIS OF NANOCOMPOSITE AND STUDY OF STRUCTURAL AND OPTICAL PROPERTIES

2.1 Synthesis of nanocomposites

2.2 Structural, Chemical and Morphological analysis

2.3 Optical property

Synthesis of nanocomposites:

Nature adopts the bottom- up approach for growth of cells and living beings, where as biology and chemistry can help them assemble and control the growth process. For the fabrication and synthesis of nanomaterials bottom-up method promises a better chance. Bottom-up methods refer to the build-up of nanostructures from bottom , i.e self-assembly of atom by atom, molecule by molecule or cluster by cluster. Fabrication is much less expensive, easy but time consuming approach. Using bottom-up approach we can fabricate nanostructures with less defects, more homogeneous chemical composition and better long- and short – range ordering. So bottom-up approaches are greatly advantageous, whereas the top-down methods usually have difficulties in terms of size and size distribution control. Reduction of Gibbs free energy occurs in case of bottom-up approach. Therefore produced nanostructures reached to a state of closer to a thermodynamic equilibrium state.

Chemical synthesis route is a bottom-up process which utilizes chemical methods to initiate and control the assembly process of the atomic or molecular building blocks. This process is intrinsically more powerful in controllable growth of a set of nanosized crystals with similar sizes and high surface/volume ratio. In the present work facile chemical synthesis procedures are followed for the preparation of the different nanocomposites. Details of the procedures is described below for as prepared nanocomposites.

2.1.1 Synthesis of CdS-ZnO nanocomposites:

All the chemicals are Merck made of analytical grade and used without further purification.

Preparation of CdS(1st step):

For preparation of CdS nanoseed, $CdCl_2$ and Na_2S were used as the reactants with molar ratio 1:1. These precursors were dissolved in distilled water under stirring (20 min). Then Na_2S solution was added drop wise in $CdCl_2$ solution keeping the solution under constant stirring. The whole system was maintained in ice-bath. The precipitate was centrifuged and washed with distilled water for several times until the pH becomes normal. The final water solution from where the precipitate was taken was also tested with silver nitrate solution to discard the presence of NaCl in the product. Finally, the obtained powder was dried at 100^{o}C for 2 hr in a vacuum furnace to get CdS nanoparticles which will be used as nanoseed for the next synthesis part. The Schematic diagram of the synthesis technique of CdS is shown in Figure 2.1.

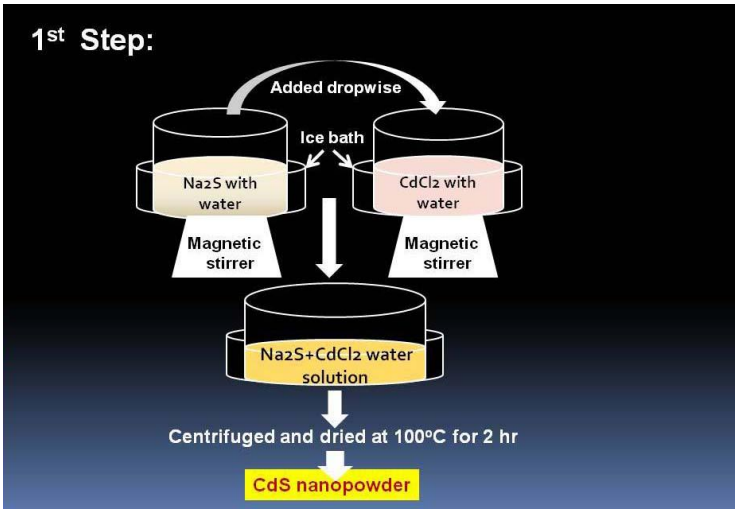

Fig.2.1. Schematic diagram showing the synthesis of CdS nanoparticle.

Preparation of CdS-ZnO nanocomposite(2nd step):

In the second step, CdS/ZnO nanocomposites in a molar ratio of 1:1 (CZ1:1), 1:2 (CZ1:2) and 1:3 (CZ1:3) were synthesized. For the preparation of CZ1:1, CZ1:2 and CZ1:3 the precursor of ZnO ($Zn(NO_3)_2$ and NaOH in 1:1 molar ratio) was taken in 1:1, 1:2 and 1:3 ratio with CdS in wt% . Measured amount of CdS nanoparticles were well dispersed in 25 ml distilled water. Appropriate amount of Zinc nitrate solution and NaOH solution were also prepared separately and added in the first solution very slowly under stirring condition. The obtained precipitate for three different samples were centrifuged, washed with distilled water for several times until the pH becomes 7 and were allowed to dry in a vacuum furnace at 100°C for 2 h. The Schematic diagram of the synthesis technique of CdS/ZnO nanocomposites is shown in Figure 2.2. To prepare the bare ZnO sample the second part of the synthesis has been carried out exactly in the same way without the CdS seed nanoparticles.

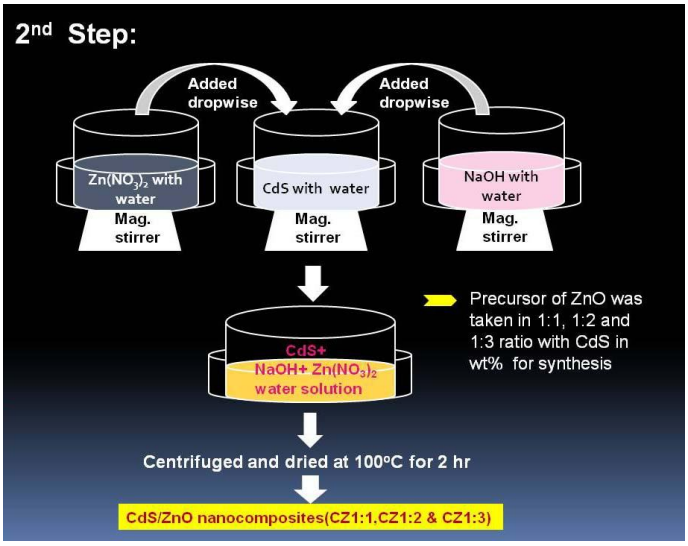

Fig.2.2. Schematic diagram showing the synthesis of CdS-ZnO nanocomposite.

2.1.2 Synthesis of Co_3O_4-ZnO nanocomposite:

Preparation of Co_3O_4(1st step):

All the chemicals are Merck made of analytical grade and used without further purification. For preparation of Co_3O_4 core, $CoCl_2$ and $NaHCO_3$ were used as the reactants with molar ratio 1:1. For this purpose 3.39 g of $CoCl_2$ was taken in 25ml of DI water and 1.2 g of $NaHCO_3$ was dissolved in 15ml of DI water. Both the solutions were kept under stirring (20 min). Then $NaHCO_3$ solution was added dropwise in $CoCl_2$ solution keeping the solution under constant stirring. The whole system was maintained in ice-bath. The precipitate was centrifuged and washed with distilled water for several times until the pH becomes normal. The final water solution from where the precipitate was taken was also tested with silver nitrate solution to discard the presence of NaCl in the product. Finally, the obtained powder was dried at 100^oC for 1hr and then calcined at 550^oC for 2 hr to get Co_3O_4 nanoparticles which will be used as nanoseed for the next synthesis part. The Schematic diagram of the synthesis technique of Co_3O_4 nanoparticles is shown in Figure 2.3.

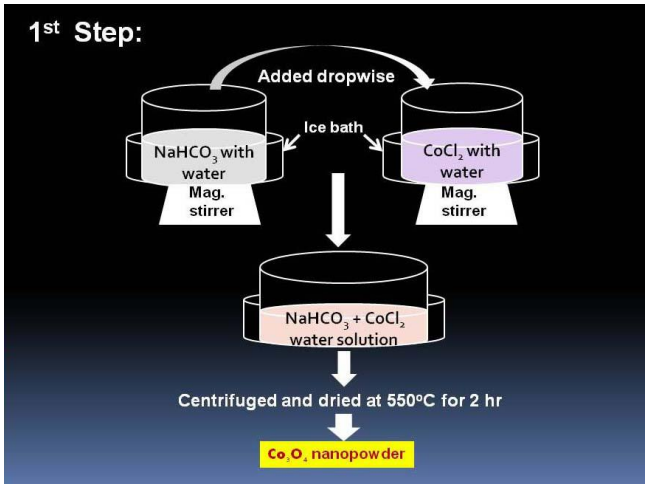

Fig.2.3. Schematic diagram showing the synthesis of Co_3O_4 nanoparticle.

Preparation of Co_3O_4 -ZnO nanocomposite(2nd step):

To produce Co_3O_4 -ZnO nanocomposites, 0.1 g prepared Co_3O_4 nanoparticles were dispersed in a solution prepared with 10ml of C_2H_5OH and 1.3ml of Triethanolamine (TEA). Separately 20 ml aqueous solution of 2.19 g zinc acetate was also prepared keeping the molar ratio of zinc acetate and TEA 1:1. Both the solutions were stirred for 30 min. Then the second solution is poured dropwise into the first solution under stirring condition, resulting in the formation of precipitates. The precipitate was centrifuged and washed with distilled water for several times. Finally, the obtained powder was dried at 60^o C for 2 hrs and then calcinated at 400^{o}C for 2 hours to form Co_3O_4-ZnO nanocomposite.The Schematic diagram of the synthesis technique of Co_3O_4-ZnO nanocomposite is shown in Figure 2.4. For comparison, only ZnO was also prepared in the above-mentioned procedure without taking the Co_3O_4 nanoparticles.

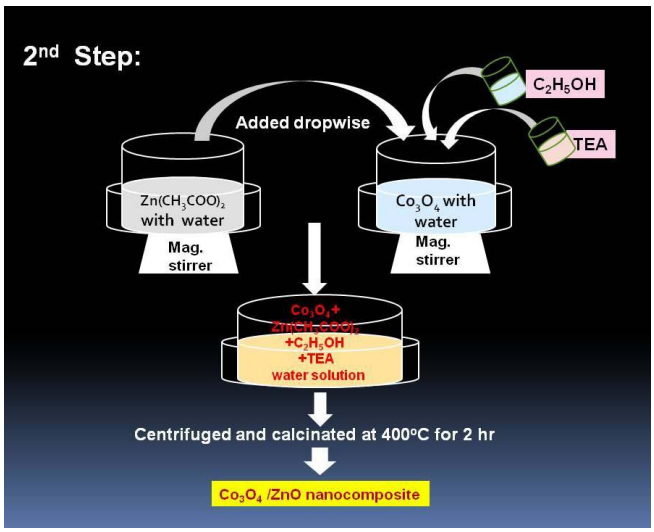

Fig.2.4. Schematic diagram showing the synthesis of Co_3O_4-ZnO nanocomposite.

2.2 Structural, Chemical and Morphological analysis:

2.2.1 Structural, Chemical and Morphological analysis of CdS-ZnO nanocomposites:

Structural analysis of all the powdered samples were carried out by Rigaku Mini-Flex X-Ray diffractometer using Cu K_α radiation (λ = 1.54178 Å) source. Morphological analysis was done by both JEM 2100 Transmission Electron Microscope at an accelerating voltage of 200 keV and FEI, Inspect F Scanning Electron Microscopy. EDX was carried out in S-4200, Hitachi.

Fig. 2.5(a)-(c) shows XRD patterns for CZ1:1, CZ1:2 and CZ1:3 samples respectively.

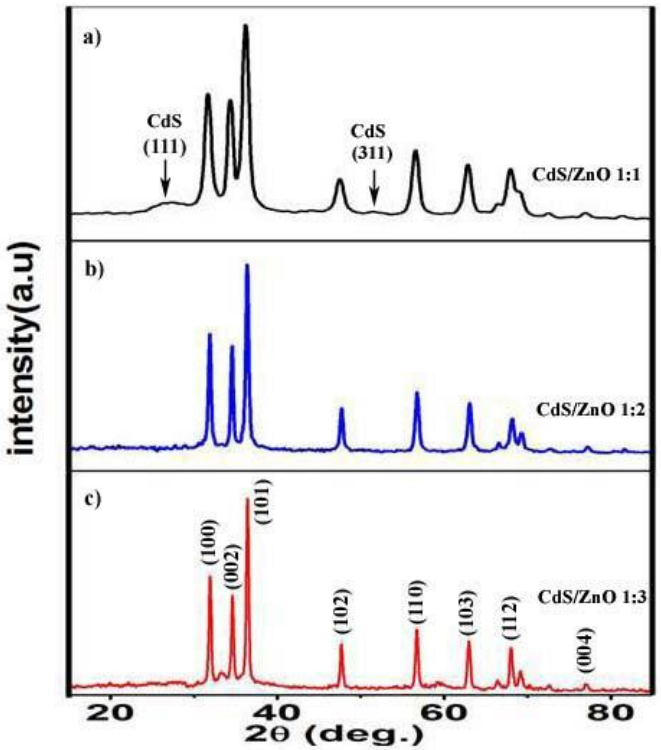

Fig.2.5. X-ray diffraction pattern of as prepared CZ1:1 (a), CZ1:2 (b) and CZ1:3 (c) sample synthesized by changing the ratio of CdS to ZnO.

As observed, three sets of diffraction peaks existed for the CdS/ZnO nanocomposites, which can be indexed as a mixture of CdS phase (ICDD card No. 65-2887) having a cubic zinc blend structure and ZnO phase, which is matched with ICDD card No. 36-1451 having the hexagonal wurtzite crystal structure. No remarkable shift and no characteristic peaks for impurity in diffraction pattern were detected. It was worthwhile to note that the diffraction peaks of ZnO in CdS/ZnO nanocomposites were intense, implying the high crystallinity. The peak intensity of CdS phase is noticeably weak (Fig. 2.5a) or absent. The result is expected [1,2] because the CdS is being shielded for the incoming X-ray by the ZnO in the CdS/ZnO nanocomposites. Figure 2.6 shows the magnified XRD analyzed data for as prepared CdS and CdS-ZnO 1:1 samples both clearly. XRD patterns of bare CdS and ZnO are shown in Fig. 2.7.

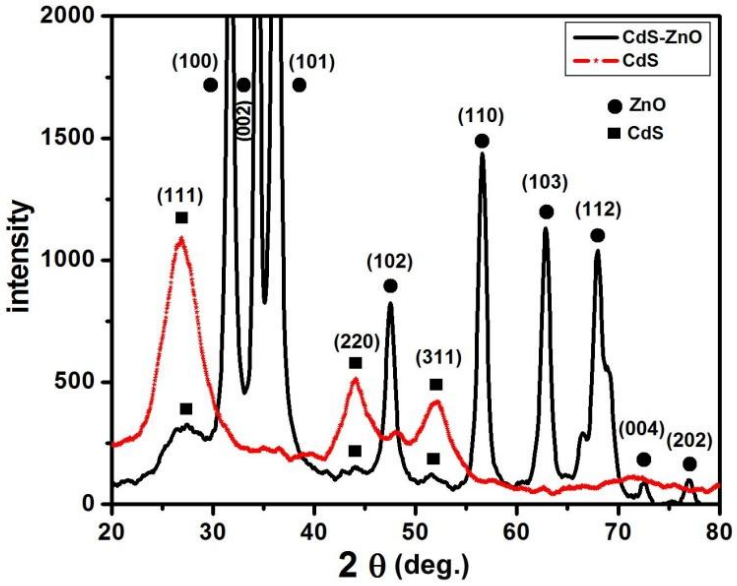

Fig. 2.6. X-ray diffraction patterns of as prepared CdS and CdS–ZnO1:1 nanocomposite.

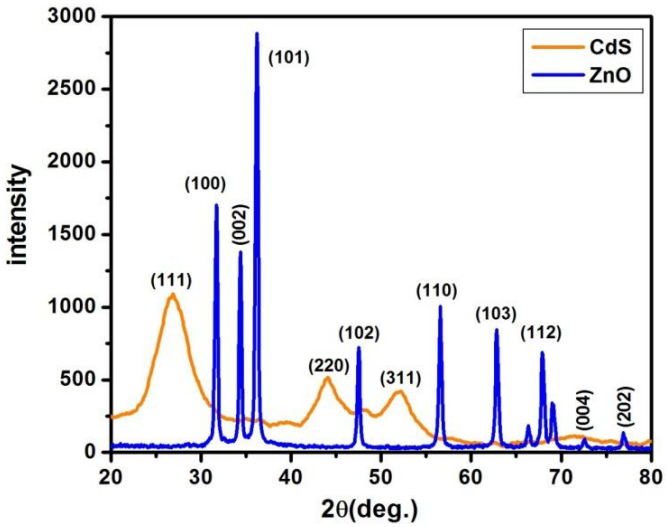

Fig.2.7. X-ray diffraction pattern of bare CdS and ZnO nanoparticles synthesized individually.

To corroborate the chemical analysis, EDX of the CZ1:1, CZ1:2 and CZ1:3 sample was also carried out and the result, Fig. 2.8(a)-(c), shows the existence of Cd, S, Zn and O elements for CZ1:1, CZ1:2 and CZ1:3 sample respectively. Fig. 2.8(d)-(f) presents the micrographs associated with the EDX measurement of CZ1:1, CZ1:2 and CZ1:3 sample respectively.

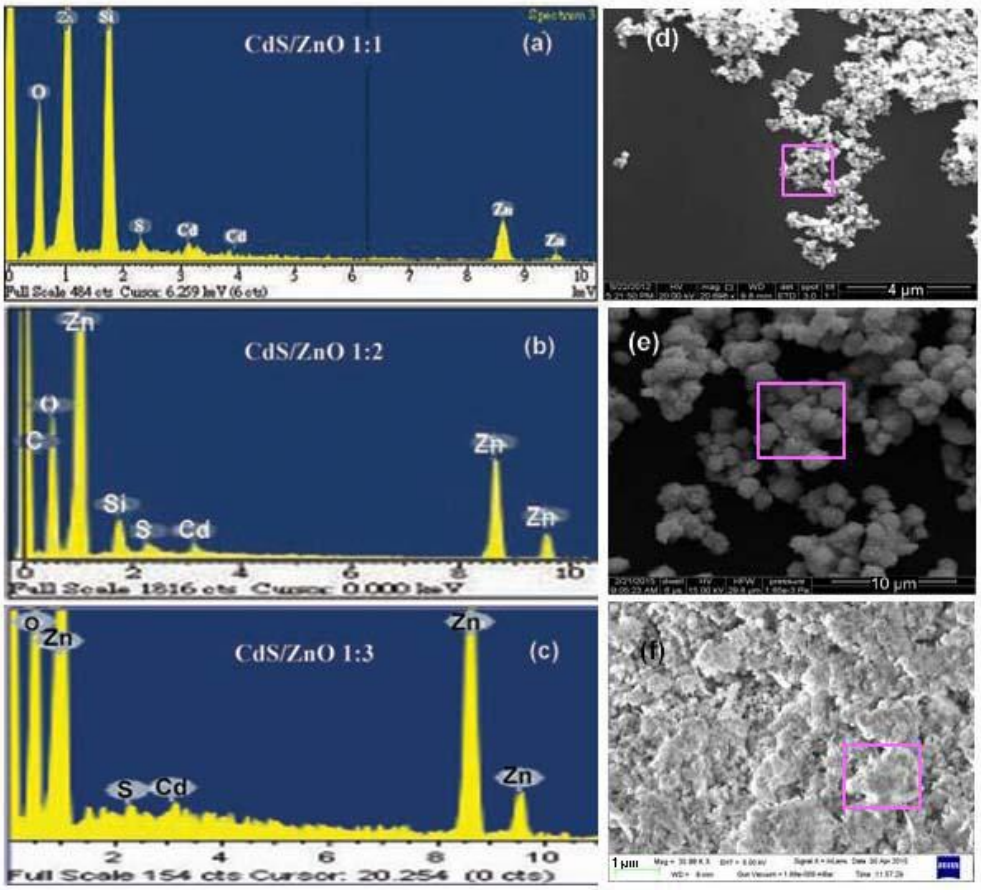

Fig.2.8. EDX (a) and associated micrograph (d) taken from CZ1:1 sample; EDX(b) and associated micrograph (e) taken from CZ1:2 sample; EDX (c) and associated micrograph (f) taken from CZ1:3 sample.

The SEM image of bare CdS, shown in Fig. 2.9(a) reveals that CdS nano seed of average size ~94 nm is the starting condition of the composite and the bare ZnO, shown in Fig. 2.9(b) presents it irregular shaped morphology with wide range of size distribution. Typical SEM and TEM images of the three CdS/ZnO nanocomposites with different morphology are shown in Fig. 2.10. Fig. 2.10(a)-(b), Fig. 2.10(e)-(f)

and Fig. 2.10(i)-(j) show SEM images of CZ1:1, CZ1:2 and CZ1:3 sample respectively at two different magnifications.

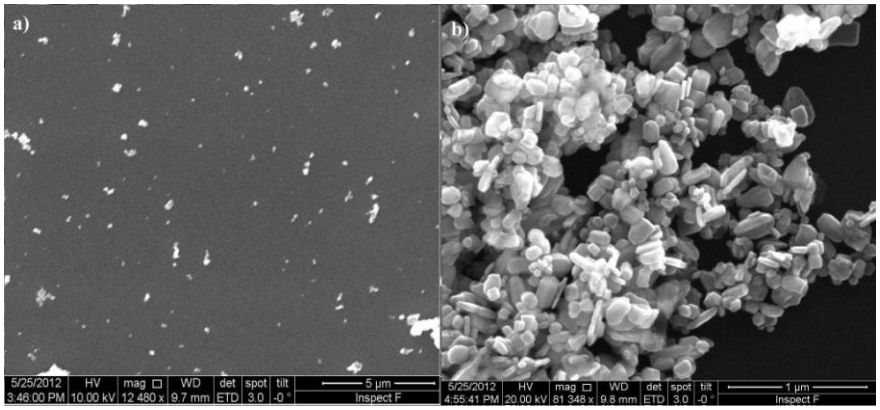

Fig.2.9. SEM image of CdS(a) and ZnO(b) nanoparticles synthesized independently.

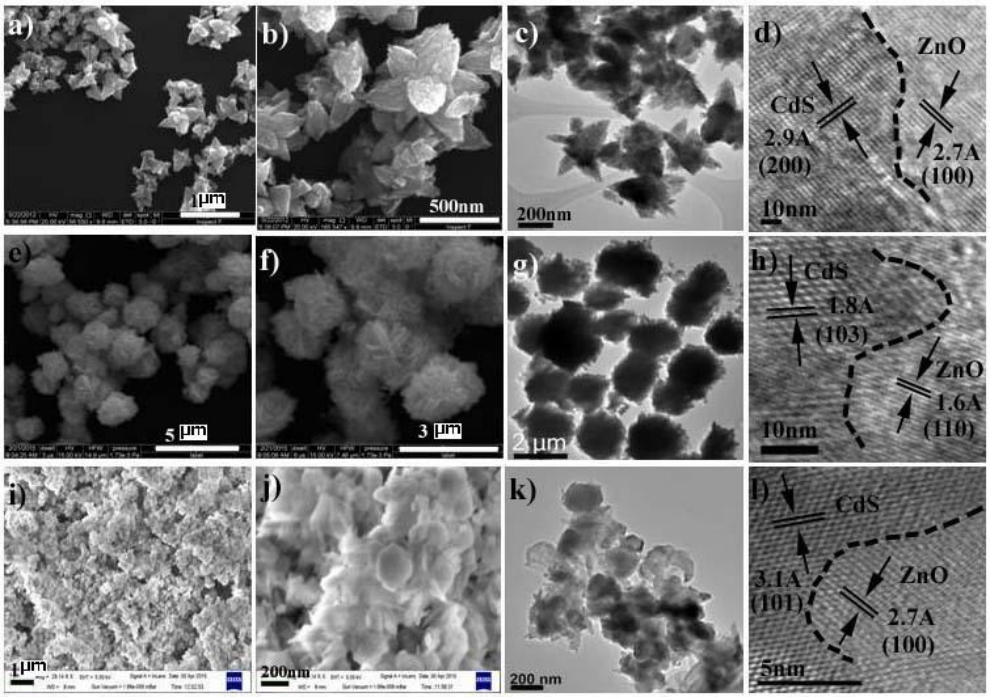

Fig.2.10. FESEM images (a)-(b) and TEM images (c) obtained for CZ1:1 sample; FESEM images (e)-(f) and TEM images (g) obtained for CZ1:2 sample; FESEM images (i)-(j) and TEM images (k) obtained for CZ1:3 sample; crystal planes are indexed within the HRTEM (d), (h) and (l) for CZ1:1, CZ1:2 and CZ1:3 respectively.

CZ1:1 sample has a flower like structure with several petal like protrusion come out at different directions from the centre. The photo gallery of Fig. 2.11 shows the typical SEM and TEM images of the synthesized CdS-ZnO nanocomposite structure. Figure 2.11(a), (b) and (c) show the SEM images at different magnifications and figure 2.11(d), (e) and (f) show the TEM images at increasing magnification. It is evident from figure 2.11(a) that the synthesized materials has an unique flower like structure where the central part looks much brighter and several petal like protrusion come out at different directions from the centre.

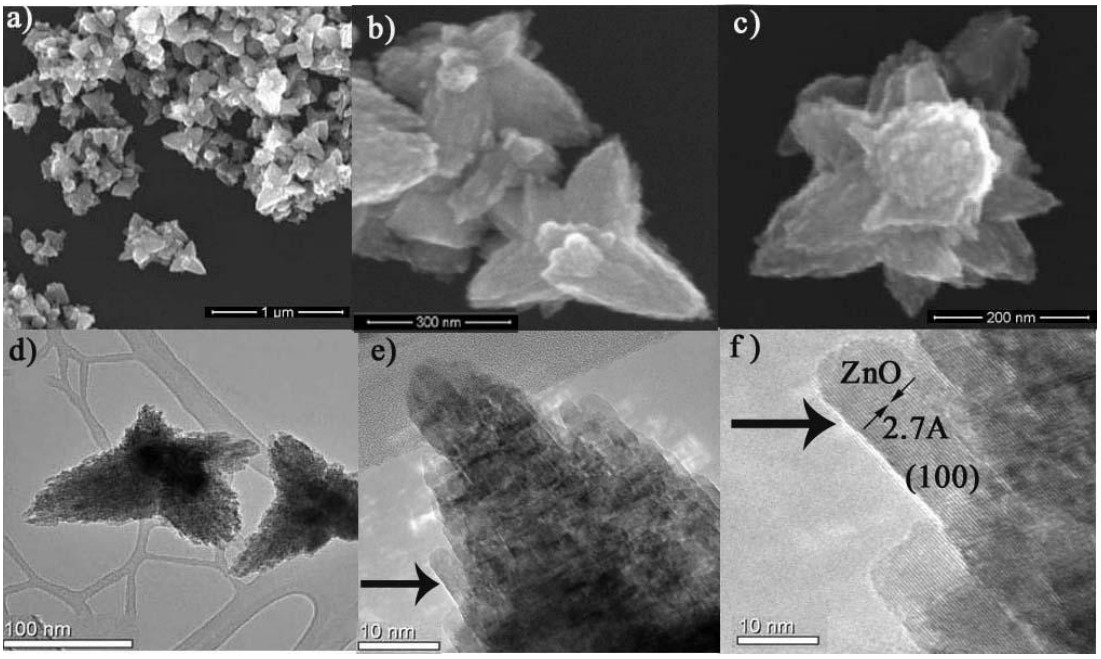

Fig.2.11. Typical FESEM (a) – (c), TEM (d) and (e) and HRTEM (f) images of the as prepared CdS–ZnO nanocomposite sample taken at different magnification. The arrow in (e) and (f) indicates the magnification region.

Figure 2.11(b) shows such few CdS-ZnO nanoflowers where it seems the flower has grown partially. In figure 2.11(c) one fully grown flower like structure has been shown. Here the number of petals is higher than the number of petals in the flower like

structure shown in figure 2.11(b) and the figure represents the typical structure of a complete CdS-ZnO unit, evolves in this synthesis mechanism. The TEM image shown in figure 2.11(d) also supports the morphology of a flower like structure of the grown composite materials. Here also the central part is much darker and it signifies that the central part is the densest region in these three dimensionally grown structures. Figure 2.11(e) shows the magnified version of a petal in the flower structure where it is seen that the petal is formed due to the congregation of several rod like structures. In figure 2.11(f) high resolution TEM shows clearly the aggregation of rods in a part of a petal. The atomic planes visible in the rod shows the unidirectional growth of ZnO and it is evident that the rods are actually made of ZnO to form the petal part of this unique structure. The average total size of a typical CdS-ZnO flower is around 400nm and the average size of the petal is 100-150nm. But the rod inside the petal has an average size of 10 nm. The average size of the central core is 90nm.

Sample CZ1:2 gives uniform ball-like structures and CZ1:3 has agglomerated flowerlike structures along with some broken petals. The TEM images shown in Fig.2.10(c), 2.10(g) and 2.10(k) also supports the morphology presented by the SEM images of the samples. Fig. 2.10(d), 2.10(h) and 2.10(l) display high resolution TEM images of the typical crystalline phases at the interface of CZ1:1, CZ1:2 and CZ1:3 sample respectively. Here the dotted black line in each figure is the eye-guidance for the interface line of the composites. The left part of the line matches with the CdS crystal plane, indexed within the figures, and the right side delineates the ZnO crystalline phase, also indexed in the figures.

2.2.2 Growth mechanism:

To understand the growth mechanism of these self assembled CdS/ZnO composite we propose the idea as shown in Fig. 2.12. Initially the synthesized CdS nanoparticles start working as the seeds to nucleate the growth of ZnO.

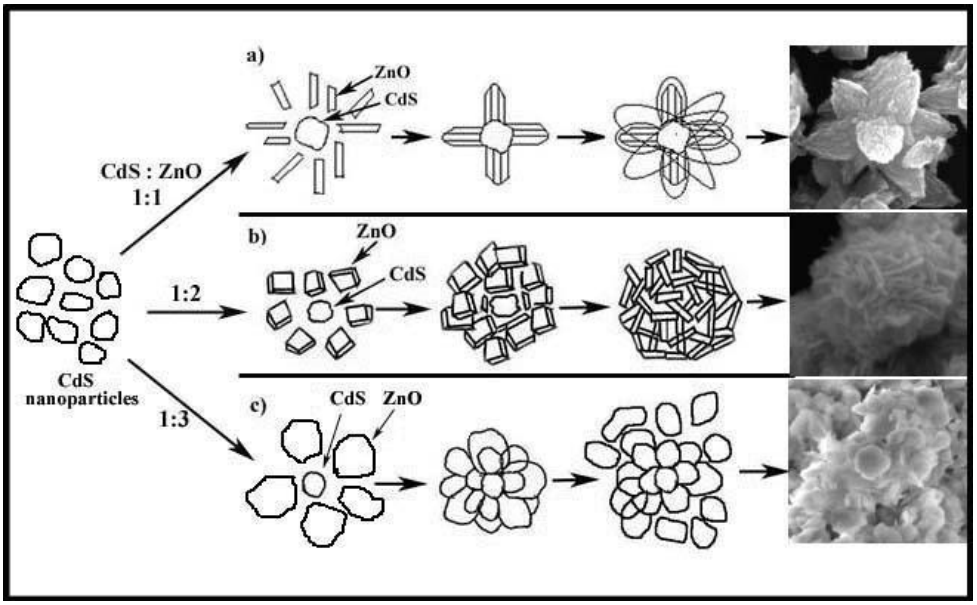

Fig.2.12. Schematic representation of the growth mechanism of CZ1:1 (a), CZ1:2(b) and CZ1:3 (c).

Now the dynamics of ZnO crystal growth depend on the atomic density of the reacting molecules in the microenvironment. It has been shown earlier that free nanoparticles often undergo entropy driven aggregation through strong inter particle interaction [3,4]. So, in the beginning, the availability of the ZnO particles, which varies according to the molar concentration, strongly controls the growth of ZnO nanocrystal on to the CdS nucleating points.

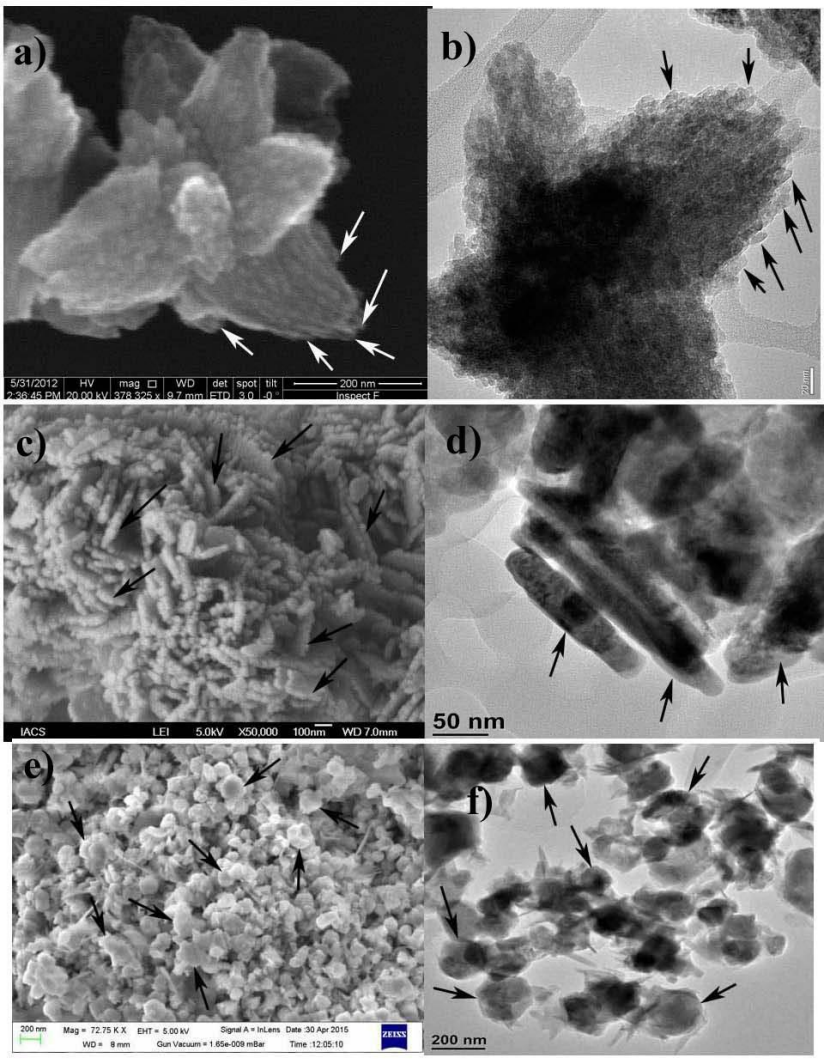

Fig.2.13. FESEM image (a) and TEM image (b) obtained for CZ1:1 sample; FESEM image (c) and TEM image (d) obtained for CZ1:2 sample; FESEM image (e) and TEM image (f) obtained for CZ1:3 sample.

In case of CZ1:1 the ZnO grows first in nanorods form and then develops, attaching to CdS centre, through point initiated vectorial growth. Consequently, those tiny nanorods marked by arrows in Fig. 2.13(a)-(b), get fused gradually at their high-surface-energy-growing fronts and form the petal like structures surrounding CdS

centre. It is found that both fully and partially grown flower like formations are available in the sample morphology. Further investigation is required to reveal the effect and control of different reaction parameters on the evolution of this nanocomposite structure. Though charge transfer characteristic of CdS quantum dot sensitized ZnO flower-like nanostructure have been reported earlier [5] in the category of these coupled semiconductors system but the growth mechanism was not addressed properly. In the category of single semiconductor system, direct observation of growth of MgO nanoflowers by chemical vapour deposition method was also addressed earlier [6]. Here, in our case, the system and structure are different and the development of the structure is given to have the in-depth understanding towards engineering the morphology of such materials.

But in case of 1:2 molar ratio, having a much higher collision probability of ZnO molecules, the growth dynamics alters from the previous case. Collisions, where the coalescence between nanocrystals may take place [7], control the oriented attachment of ZnO to form small sheet like structure first and then the structure develops surrounding the CdS nucleating zone. It is well understood that the growth rate of nanocrystals morphology strongly depends upon the [7,8] nanocrystal concentration and reactant concentrations. Here without implying any legand to control the viscosity we simply change the molar concentration to get the ligand free oriented attachments [8]. In this CZ1:2 sample, we typically get mostly uniform, ZnO-CdS ball-like structures where ZnO sheets marked by arrows in Fig. 2.13(c)-(d), are loosely bounded around the CdS nanocenters. In case of CZ1:3, even higher concentration of starting ZnO molecules accelerates the aggregation process of ZnO molecules to form a somewhat irregular sheet like structures which are marked by arrows in Fig. 2.13(e)-(f). The driving force of aggregation along different axis depends on the atomic

density of the corresponding crystal planes and in this particular reaction mechanism the plenty of ZnO oxide nanorod units eventually form the irregular petal like structure by oriented attachment. Those comparatively bigger petals of ZnO then settle around the CdS zone. But probably due to the bigger size of ZnO unit and their inter-particle interaction the CdS- ZnO flower structure disintegrates in some places. The predicted dynamics of the growth process for these three self assembled flowers like structures are delineated in Fig. 2.12. It is interesting to point out that without CdS nanoseed, the ZnO nanoparticles are grown in random shape and size (Fig. 2.9b). So it is quite obvious that the role and control of CdS nanoparticle in developing CdS/ZnO well defined composite structures are very much important. This also demonstrates the synergistic effect of heterostructured composite materials in self assembled growth dynamics.

2.2.3 Structural, Chemical and Morphological analysis of Co_3O_4-ZnO nanocomposites:

Figure 2.14 shows the XRD analyzed data for as prepared Co_3O_4, ZnO and Co_3O_4-ZnO samples. It is evident from the peaks of the Co_3O_4-ZnO sample that the product is well crystalline having no impurity as there is no unmatched peak. All the peaks of the final product are matched either with Co_3O_4 or ZnO. Interestingly compare to the peak intensity of pure Co_3O_4, the peak intensity Co_3O_4-ZnO for Co_3O_4 phase is noticeably weak and some of the previous peaks of Co_3O_4 sample are completely absent in the final product.

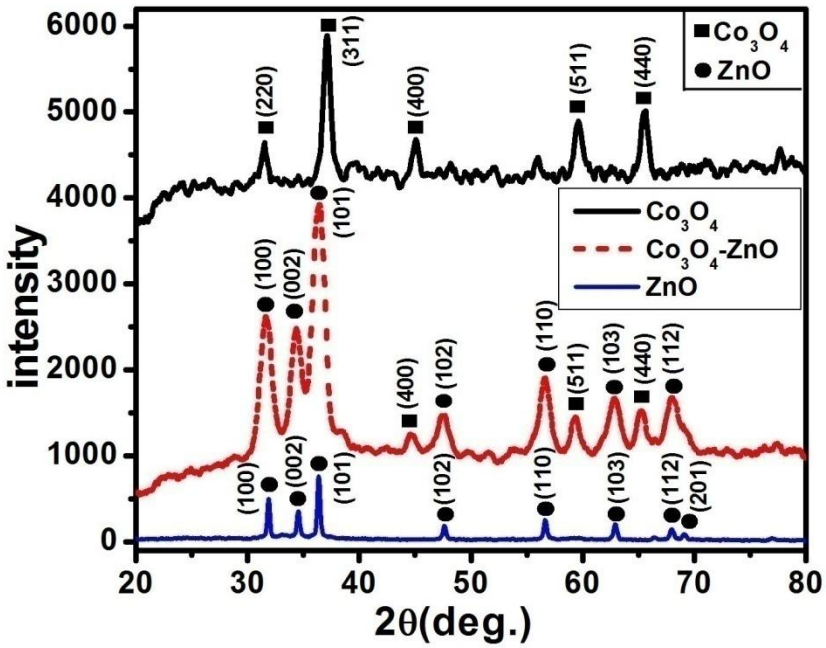

Fig.2.14. X-ray diffraction patterns of as prepared Co_3O_4, ZnO and Co_3O_4-ZnO nanocomposite.

The result is attributed to the fact that Co_3O_4 is being shielded for the incoming X-ray by the outer ZnO shell in the composite form and the findings of some other reported literatures [1-2]. It is also very distinct from the peak intensity that ZnO phase is much stronger than the Co_3O_4 phase in the final product. It is to be noted that the peak arising from (100) plane of ZnO of the final composition may also have partial contribution of (220) plane of Co_3O_4 core as it appears like a convoluted form of two peaks. Co_3O_4 phase (ICDD card no. 71-4921) has cubic structure with lattice constant a =8.04 Å where as ZnO phase is matched with ICDD card no. 36-1451 having hexagonal wurtzite crystal structure (a=b=3.2495 Å, c=5.2069 Å).

Figure 2.15 shows the EDX and SEM results in a combined fashion. To corroborate the chemical analysis, EDX of the sample was also carried out and the

result, figure 2.15a, shows the existence of Co, Zn and O elements. Here the Si line was originated from the Si wafer which was taken as the substrate for the powdered sample to carry out EDX measurement. Typical SEM images of the synthesized Co_3O_4-ZnO nanocomposite structure are presented in figure 2.15b and 2.15c in two different magnifications. It is seen that the boundary of the particles have different contrast that may arise due to the shell formation with ZnO onto the Co_3O_4 nanoparticles. Sizes of the nearly spherical particles are lying within 10-40 nm range.

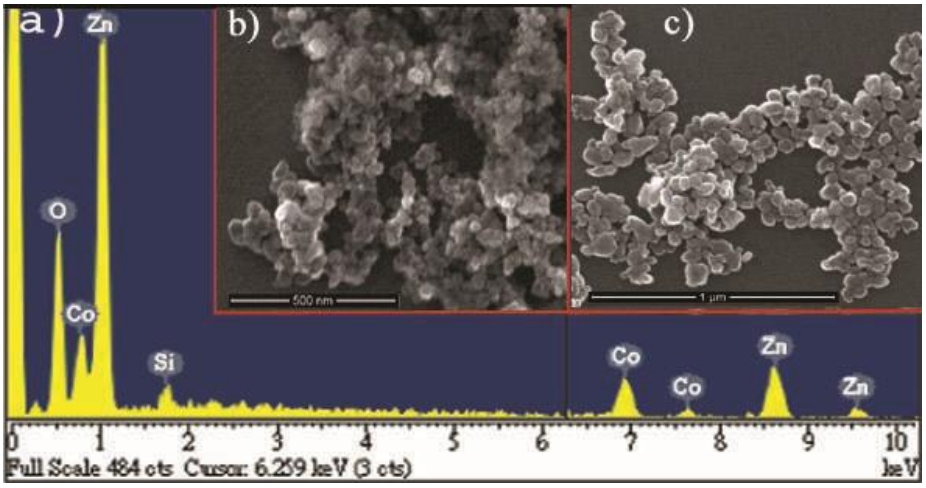

Fig. 2.15. EDX taken from as prepared Co_3O_4-ZnO coreeshell nanocomposite samples deposited on Si wafer (a); Typical FESEM images of the Co_3O_4-ZnO nanocomposite sample taken at different magnification (b)-(c).

To investigate the morphology in details TEM study was carried out and the result is shown in figure 2.16. Figure 2.16 a-c show the TEM images at increasing magnification. First image shows the typical morphology of the synthesized materials having almost core shell type nanostructure in some of the particles.

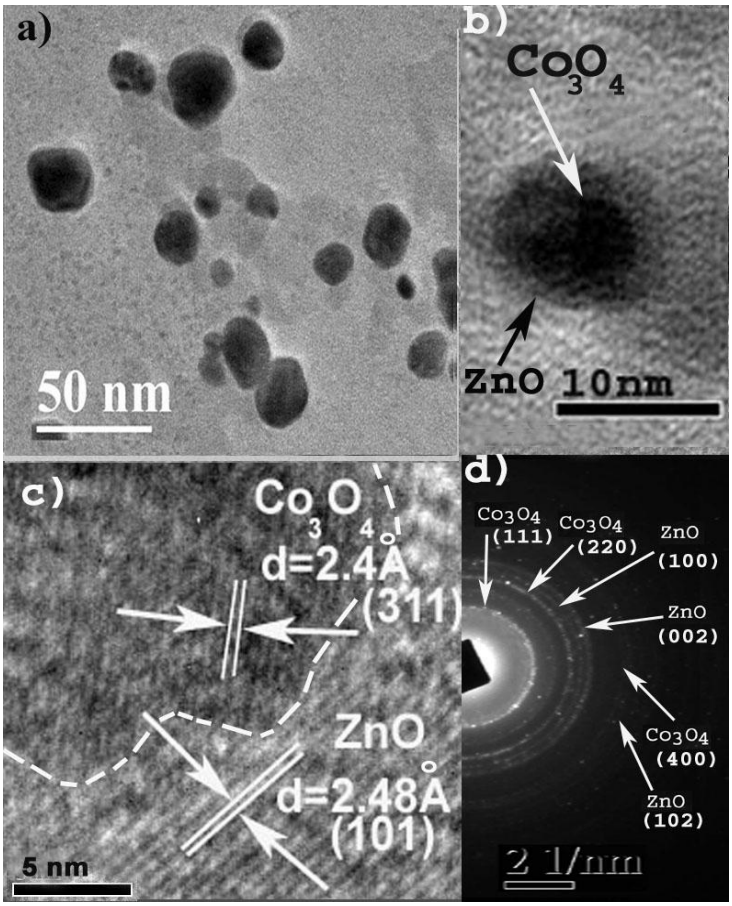

Fig. 2.16. TEM (a)-(b) and HRTEM (c) images of the as prepared Co3O4-ZnO nanocomposite sample taken at different magnification; Typical SAED pattern of Co_3O_4-ZnO nanocomposite with matched crystal planes (d).

It is also to be observed that the shell formation is not uniform onto the nanoparticles. As a whole the coupled nanocomposite structures are nearly spherical with distinct interface of the two materials. It is evident from figure 2.16b that the central part looks much darker referring the Co_3O_4 core and outer part reflects ZnO phase. In figure 2.16c high resolution TEM image shows the typical crystalline phases at the interface of one such composite nanoparticle. Here the dotted white line is the eye-guidance for the interface line. The inner part of the line matches with the Co_3O_4 crystal plane,

indexed within the figure, and the outer part delineates the ZnO crystalline phase, also indexed in the figure. Here it is worthy to note that typically the interfaces for the particles are not very regular and we believe that the stress generated due to the shell formation onto the Co_3O_4 core makes the outer surface of the core much curvilinear. Selected area electron diffraction pattern was also taken from such a typical nanocomposite and the result is shown in figure 2.16d.

It is to be noted that both the crystalline phases, indexed within the figure, were observed. The planes, calculated from the diffraction pattern, also support the initial observations from the XRD study. On the perspective of the results obtained so far, we have proposed a model of growth mechanism which is shown in figure 2.17.

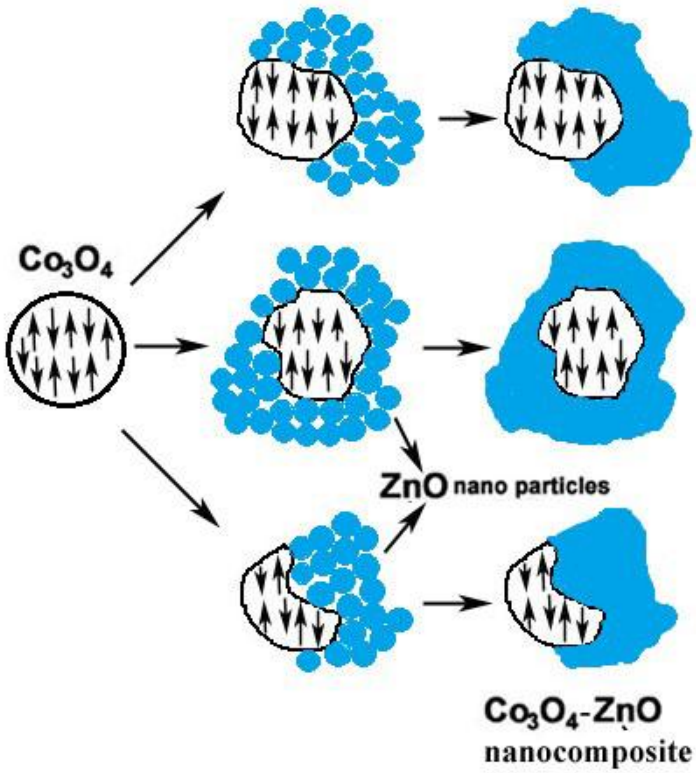

Fig.2.17. Schematic diagrams showing the formation of ZnO shell on magnetic Co3O4 core with irregular shaped coreeshell interface.

The model starts with the Co_3O_4 nanoparticle, grown in the first phase of the synthesis part and such Co_3O_4 nanoparticles are the nucleating points for the next phase of synthesis. In the next part of synthesis, several ZnO nanoparticles will start to grow initiating from the Co_3O_4 seeds. As the reaction proceeds, the nearby ZnO nanoparticles get agglomarated and eventually the ZnO shell is formed onto the surface of Co_3O_4 nanoparticles. Here it is to be noted that the outer shell ZnO is of wurtzite structure while the inner Co_3O_4 is of cubic structure. So in this heterostructured interface, strain induced defects and crystal dislocations are very much expected. Curvilinear interface boundary of the model represents the strain induced defects at the crystal boundary. This type of strain effect may contribute to the exhibition of novel physical properties in the heteronanostructures [9].

2.3 Optical property:

The optical properties of a material arise from the interaction of the incident electromagnetic wave with the composition and atomic structure of the material. The optical reflectance R is the fraction of the incident light that is reflected from the surface of the material. Metals have high reflectance at longer wavelengths(>500 nm) but the reflectance declines at shorter wavelengths. The high reflectance of the metals is due to the partially filled conduction band.this conduction band allows photons to be absorbed and reflected over a wide range of energies(1-3 eV) forming a continuum of energies from the infrared to the visible range. Most of the metals exhibit a marked decrease in reflection in the ultraviolet range. Semiconductors have low reflectance at longer wavelengths. But the reflectance of semiconductors increases rapidly with the

decrease in wavelength beyond a threshold wavelength called band edge or absorption edge. Semiconductors have higher absorbtion and reflection in the ultraviolet range(<380 nm) and very low in the infrared range(>760 nm). Absorption increases when the incident photon energy becomes larger than the bandgap for the semiconductors. Exciton generation is one of the optoelectronic processes that takes place in semiconductors. A bound electron-hole pair, called an exciton can be generated by a photon having an energy greater than the band gap of the material. The band gap is the energy separation between the top filled energy level of the valance band and the nearest unfilled level in the conduction band above it. The absorption of a photon, leading to excitation of an electron from the valence band to the conduction band of the semiconductor along with a hole in the conduction band, is associated with the band gap energy, E_g. The result is a hole in the valance band which corresponds to an electron with an effective positive charge. Due to Coulomb attraction between the positive hole and the ngetive electron, a bound pair, called exciton, is formed that can move through the lattice. The presence of the exciton has a strong influence on the electronic properties of the semiconductor and significantly its optical absorption. The optical properties of nanostructured materials differ remarkably from bulk materials. This difference is attributed to the quantum confinement effects, unique surface phenomena, and efficient energy and charge transfer over nanoscale distances within nanoparticles. Chakrabarty et al[10]. reported that NiO nanoparticle is almost transparent in visible region and shows almost sharp absorbance peak around 3.75eV(330 nm). Figure 2.18 presents the optical absorption spectra of Nickelous oxide (NiO).

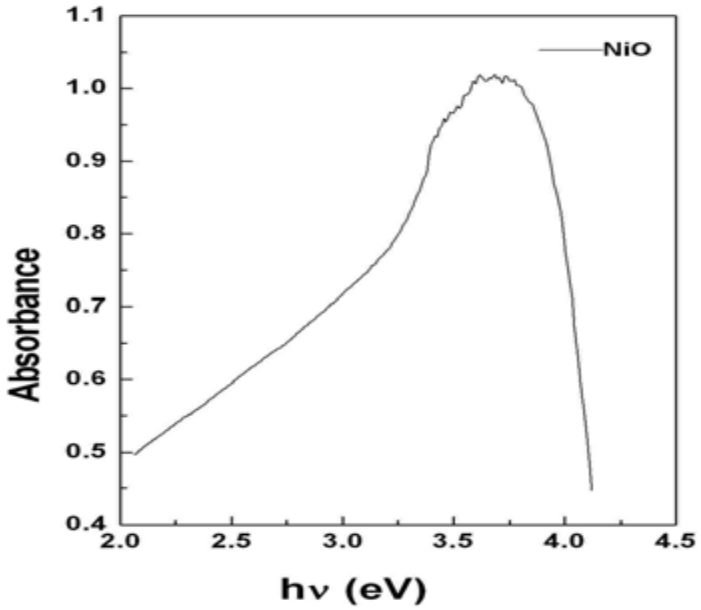

Fig.2.18. Optical absorption spectrum of NiO nanoparticles (From Chakrabarty et al. 2009)

For both types of material, direct and indirect band gap semiconductors, the absorption edge is shifted towards higher energy as the particle size decreases due to quantum confinemement. Since the absorption edge is due to band gap, the band gap increases as particle size decreases. Intensity of the absorption also increases as the particle size is reduced. The higher energy peaks are associated with the exciton and they shift to higher energies with the decrease in particle size. These effects are a result of the confinement of the exciton. As the particle size is reduced, the hole and the electron are forced closer together and the separation between the energy level changes. The spectroscopic study of the core/shell nanoparticles reveals that with increasing shell thickness the intensity of the UV absorbance increases and the reflectance shifts toward the higher wavelength region as shown in Figure 2.19[11-13].

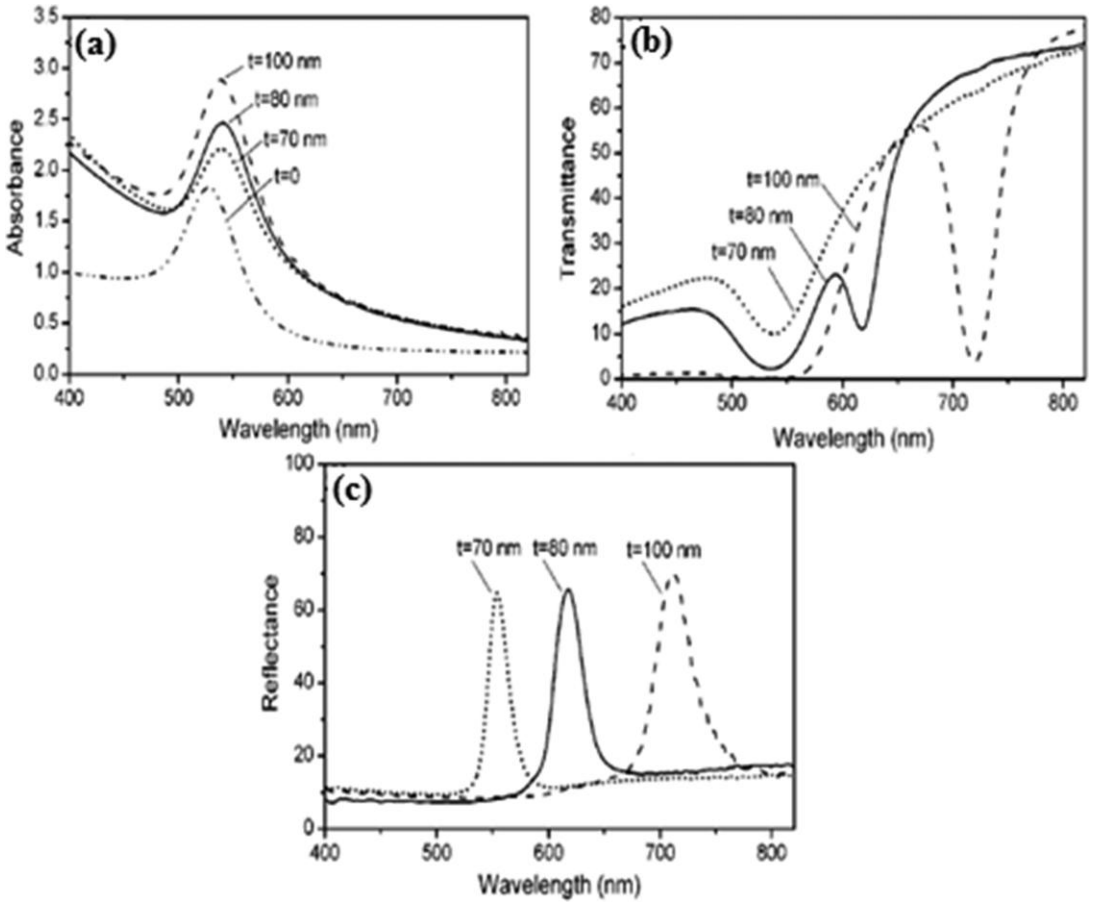

Fig 2.19 . (a) UV_visible absorption spectra of Au/SiO_2 core/shell nanoparticles with different shell thicknesses (t); (b, c) Transmission and reflectance spectra taken from photonic crystals crystallized from Au/SiO_2 core/shell particles. Reprinted with permission from ref 13. Copyright 2002 American Chemical Society.

In photoluminescence(PL), the energy of emitted photon is lower than the energy of excitation photons. A typical PL spectrum represents both band edge and trap state emission. The emission can be enhanced by surface modification like what is normally observed during nanoparticle growth. The enhancement of band edge emission is possible by capping the particle surface with materials that can reduce the trap states.

The PL spectra has also been observed to shift with change in particle size like absorption spectra. As the particle size reduces,various surface trap states affect due to increased surface area. The band gap also increases due to quantum confinement effect. Shiang et al. reported thatabsorption edge shifts with change in particle size[14]. Color of colloid solution changes as the size of semiconductor nanocrystal changes. The emission spectra of NiO nanoparticles with different particle size is shown in figure 2.20. It is observed that the emission peak intensity decreases with decreasing grain size[15].

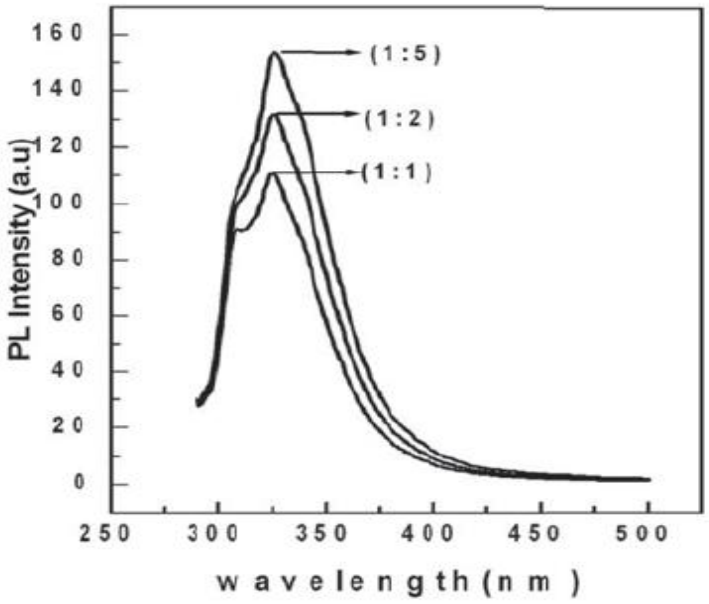

Fig.2.20. NiO nanoparticles with three different grain size- 1:1(17.8 nm), 1:2(24 nm), 1:5(30 nm) and the respective emission spectra (From Chakrabarty et al. 2012).

2.3.1 Optical study of CdS-ZnO nanocomposites:

Optical absorption spectra of the powdered samples were recorded in a UV-Vis 1700 Shimadzu Spectrophotometer and to get these spectra the powdered samples were dispersed in ethyl alcohol and mounted in the sample chamber while pure ethyl alcohol was taken in the reference beam position. For the PL the sample was taken in powder form and the measurement was carried out in Perkin Elmer LS55 fluorescence spectrophotometer. Figure 2.21(a) shows the UV-Vis absorption characteristics of the pure CdS and CdS-ZnO nanocomposite. In the lower panel of figure 2.21(a) the absorption peak for prepared CdS sample is found to be near 470nm. After formation of the nanocomposite the distinct signature of CdS has been lost and there is no such peak at 470nm observed in the absorption spectrum shown in the upper panel of figure 2.21(a). The sharp peak in the UV region at around 353nm is originated from the band edge transition of ZnO. Photoluminescence spectra of CdS and CdS-ZnO nanocomposite samples are shown in the figure 2.21(b). It is interesting to note that CdS has strong emission peak near 561nm along with two other peaks at 530nm and 544nm. It is established that surface defects as well as shallow and deep trap states play important role in the luminescence property of CdS. Here the strong emission peak near 561 (2.19eV) is expected to be linked to the trapped electron/holes at surface defects [16] and peak originated at 530nm (2.32eV) corresponds to the defects caused by the interstitial sulfur [17]. But in case of CdS-ZnO nanocomposite the spectrum shows almost quenching of emission peak intensity at 561nm while the other two peaks in position and intensity are almost remaining same as the pure CdS sample.

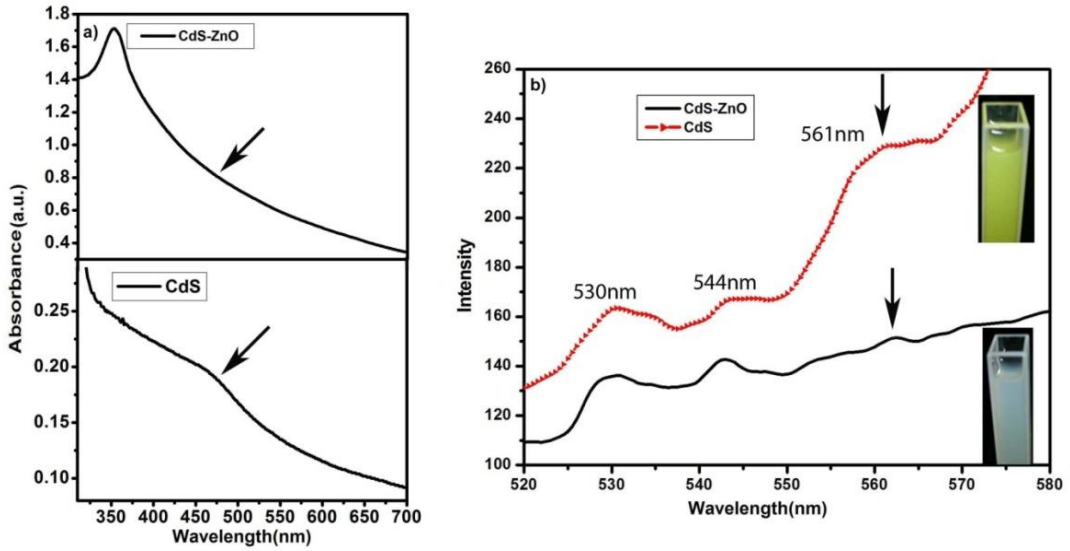

Fig.2.21. Optical absorbance spectrum for CdS sample [(a) lower panel] and for CdS–ZnO nanocomposite sample [(a) upper panel]; emission spectra for CdS and CdS–ZnO samples (b). The excitation wavelength is 310 nm for both the case. Inset of (b) panel shows the photograph of respective sample at UV light (254 nm).

+

It signifies that the transfer of electrons from CdS conduction band to ZnO conduction band in the present CdS-ZnO system may inhibit the radiative relaxation of the electrons in CdS energy levels and cause the effective quenching of emission band at 2.19 eV. To make the matter visibly clear the UV-photography of both samples are presented here. Inset near to CdS spectrum in figure 2.21(b) shows yellow luminescence of the CdS sample dispersed in DI water taken in UV light(254nm). The photograph for the CdS-ZnO sample taken in same UV source has been shown near to the CdS-ZnO spectrum in figure 2.21(b). Here also it is clear that the luminescence of CdS has been quenched after the formation of CdS-ZnO nanocomposite. These available separated electrons and holes now can effectively be

guided towards the activation of other chemical elements and this observation pave the foundation of the possibility that the materials can be utilized in photocatalytic applications.

2.3.2 Optical study of Co_3O_4-ZnO nanocomposites:

Figure 2.22 shows the UV-Vis absorption characteristics of the pure Co_3O_4 and Co_3O_4-ZnO nanocomposite. In the upper panel of figure 2.22, the absorption spectra for prepared Co_3O_4 and ZnO samples are shown. Co_3O_4 nanoparticles present two broad peaks, originated at around 455 nm and 754 nm. These two band gap absorption peaks are quite close to the recorded band energies of the other reported Co_3O_4 systems [18,19]. The multiple band gaps for the Co_3O_4 nanoparticles is attributed to the possibilities of O^{2-} to Co^{2+} and O^{2-} to Co^{3+} charge-transfer processes in Co_3O_4 nanoparticles as observed in Co_3O_4 quantum dot in cubic morphology [20]. Bare ZnO shows near band edge absorption peak at around 365nm. Lower panel of figure 2.22 shows the absorbance characteristics of Co_3O_4-ZnO nanocomposites sample. After formation of the nanocomposite the intense peaks of Co_3O_4 has been lost and weak peaks, originated from Co_3O_4, are observed at around 765 nm and around 485nm.

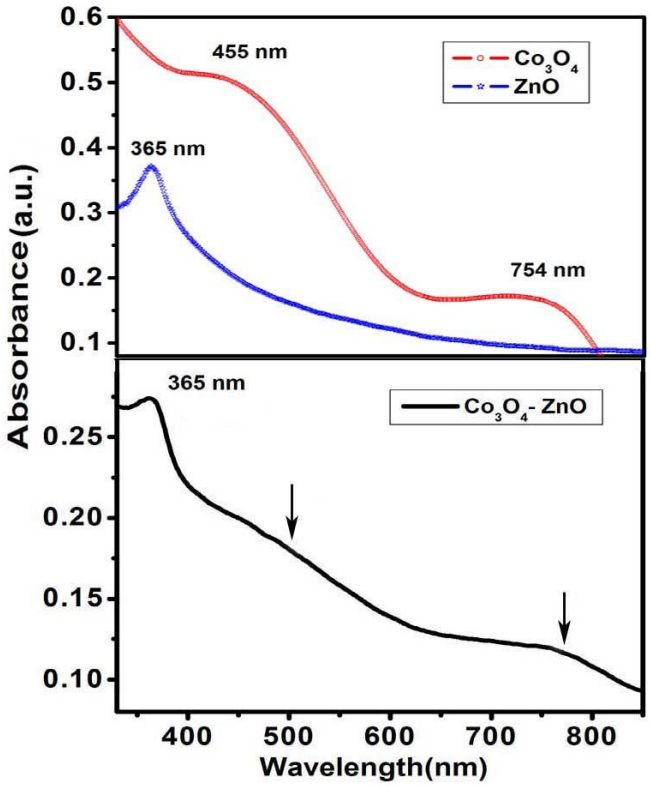

Fig.2.22. Optical absorbance spectrum for Co_3O_4-ZnO nanocomposite (lower panel) and same for bare ZnO and Co_3O_4 samples (upper panel).

The sharp peak in the UV region at around 365nm is originated from the band edge transition of ZnO. The wavelength shifting of the Co_3O_4 peak positions in the Co_3O_4-ZnO nanocomposite is attributed to the surface defect states/trap states caused by the local lattice mismatch after shell formation.

References

1. R.G. Chaudhuri, S. Paria, Chem. Rev. 112, 2373 (2012).
2. D. Jiang, L. Cao, W. Liu, G. Su, H. Qu, Y. Sun, B. Dong, Nanosc. Res. Lett. 4, 78 (2009).
3. H. Xu, W. Wang, W. Zhu, L. Zhou, M. Ruan, Cryst. Growth Des. 7, 2720 (2007).
4. J. Liu, X. Huang, Y. Li, K.M. Sulieman, X. He, F. Sun, Cryst. Growth Des. 6, 1690 (2006).
5. P. Sudhagar, S. Chandramohan, R.S. Kumar, R. Sathyamoorthy, C.H. Hong, Y.S. Kang, Phys. Status Solidi A 208, 474 (2011).
6. X.-S. Fang, C.-H. Ye, L.-D. Zhang, J.-X. Zhang, J.-W. Zhao, P. Yan, Small 1, 422 (2005).
7. X. Xu, F. Liu, K. Yu, W. Huang, B. Peng, W. Wei, ChemPhysChem 8, 703 (2007).
8. Y. Liu, D. Wang, Q. Peng, D. Chu, X. Liu, Y. Li, Inorg. Chem. 50, 5841 (2011).
9. X. Chen, Y. Lou, A.C. Samia, C. Burda, Nano Lett. 3, 799 (2003).
10. S. Chakrabarty and K. Chatterjee, Journal of Physical Sciences, 13, 245 (2009).
11. J. Ye, B. De Broek, R. D. Palma, W. Libaers, K. Clays, W. V. Roy, G. Borghs, G. Maes, Colloids Surf. A. 322, 225 (2008).
12. Y. Qi, M. Chen, S. Liang, W. Yang, J. Appl. Surf. Sci. 254, 1684 (2008).
13. Y. Lu, Y. Yin, Z. Y. Li, Y. Xia, Nano Lett. 2, 785 (2002).
14. J.J. Shiang, S.H. Risbud, A.P. Alivisatos, Journal of Chemical Physics 98, 8432 (1993).

15. S. Chakrabarty, K. Chatterjee, Nanoscience Methods 1, 213 (2012).

16. J. Chrysochoos, J. Phys. Chem. 96, 2868 (1992).

17. A. Blanco, C. Lopez, R. Mayoral, H. Miguez, F. Meseguer, Appl. Phys. Lett. 73, 1781 (1998).

18. A.E. Kandjani, S.E.H. Amiri, M.R. Vaezi, S.K. Sadrnezhaad, J. Optoelectron. Adv. Mater. 12, 2057 (2010).

19. X. Wang, X. Chen, L. Gao, H. Zheng, Z. Zhang, Y. Qian, J. Phys. Chem. B 108, 16401 (2004).

20. R. Xu, H.C. Zeng, Langmuir 20, 9780 (2004).

CHAPTER 3

PHOTOCATALYTIC PROPERTY OF NANOCOMPOSITE

3.1 Photocatalytic Properties of CdS-ZnO nanocomposite

3.2 Photocatalytic Property of Co_3O_4-ZnO nanocomposite

In 1839 Bequerel et al. first reported photocatalysis[1]. The investigation that was reported with the concept of "heterogeneous photocatalysis" in 1964 by Doerfler and Hauffe when they carried out the oxidation of CO using zinc oxide as catalyst under illumination[2]. However, revolution took place in the field of heterogeneous photocatalysis after the work by Fujishima and Honda in 1972[3]. They studied the photo-assisted catalysis of water on irradiation on TiO_2 with photons of energy greater than the bandgap of TiO_2 semiconductor. The photocatalytic process begins when the photons of energy higher or equal to the band gap energy hits the surface of the semiconductor, an electron jumps from the conduction band to valance band, thus creating an electron-hole pair. The electron-hole pairs dissociate into free photoelectrons in the conduction band and photoholes in the valence band. These photo-induced electrons and holes move separately to the surface of the semiconductor and react with the O_2 and OH^- involved in the dye solutions. This leads to the formation of hydroxyl radicals (•OH), superoxide radical anions ($•O_2^-$) and hydroperoxyl radicals (•OOH) which can decompose the organic dye[4]. In presence of adsorbed water, electrons transfer from water molecule to the positive holes to produce •OH radicals which are powerful oxidants and react with organic and toxic compounds. •OH radicals play an important role in initiating oxidation reactions. This oxidation pathway is known as indirect oxidation to differentiate it from the direct oxidation by holes. However, the role of the •OH radicals is probably overestimated, and some controversial aspects have been reported regarding the origin of photogenerated free •OH radicals[5-6]. The mechanism of the illuminated catalyst, the surface phenomena, and the generated species has been investigated and the parameters that affect the photocatalytic process and consequently the reaction rate have been studied in several reports[7-9]. There are intrinsic and extrinsic parameters

that affect the kinetics and mechanisms of photocatalytic reactions in aqueous media. Detailed explanation about the influence of solution pH, catalyst dosage, substrate concentration, temperature, photonic flux, and the reactor design has been also described in many articles[10-12]. The efficiency of a photocatalyst depends on the competition of different interface transfer processes involving electrons and holes and their deactivation by recombination. Figure 3.1 shows the underlying science of photocatalytic actvity of a semiconductor.

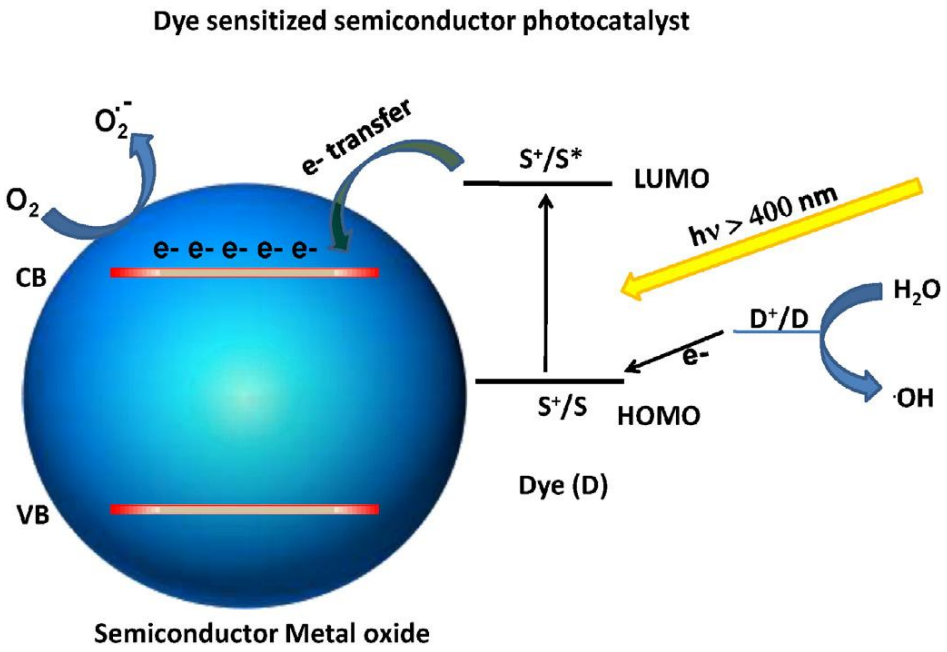

Fig. 3.1. Schematics of principle of photocatalysis. Reprinted from [13], Copyright (2016), with permission from Elsevier.

Su et al.[14] demonstrated that TiO_2/CdS heteroarchitectures possess a higher photocatalytic activity than the pure TiO_2 for the degradation of RB dye under visible-light irradiation, due to the enhanced visible-light absorbing capability stemming from the improvement of the separation of photogenerated electrons and holes between the

TiO_2 and the CdS. The schematic profile depicting the energy band structure and occurrence of vectorial electron transfer in the TiO_2/CdS heteroarchitectures is shown in figure 3.2.

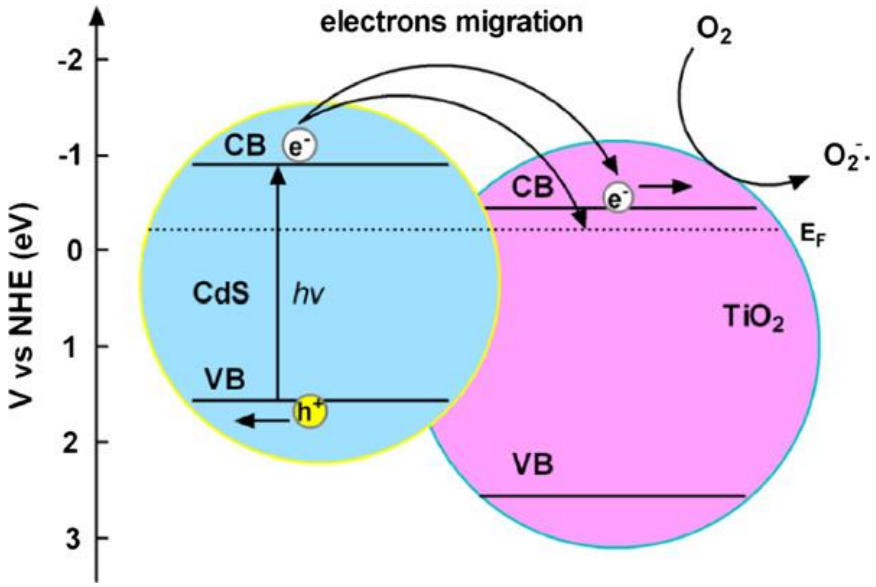

Fig. 3.2. Scheme showing the charge transfer process between the coupled heteroarchitecture semiconductors. Reprinted from [14], Copyright (2011), with permission from Elsevier.

The area of environmental remediation assisted by photocatalytic technologies is an exciting subject of research. It is evident that interdisciplinary research is required to reveal the full picture of the toxicity mechanisms and consequences of the impact of the nanostructured photocatalytic materials on the functioning and health of living beings and the environment.

3.1 Photocatalytic Properties of CdS-ZnO nanocomposites:

The photocatalytic activity of the as prepared samples for the degradation of RhB in aqueous solution was evaluated by measuring the absorbance of the visible light irradiated solution. Prior to irradiation, 10 µM solution of RhB in DI water was taken and sample was added to it to maintain a catalyst concentration of 1gm L^{-1}. Afterward, the organic dye with a catalyst solution was magnetically stirred in dark for 1 hr to assure the adsorption/desorption equilibrium between CdS-ZnO catalyst and RhB. The photocatalytic process was performed by exposing the solution to 1000 Watt halogen lamp radiation and the solution was kept in a cold water bath containing 1mol L^{-1} $NaNO_2$ which is used for removing light wavelength shorter than 400nm [15]. The beaker containing the solution was kept in cold water bath to maintain the reaction temperature at 290 K. The radiation from the halogen lamp in the NIR region was balanced by keeping the solution always in the room temperature and ensuring that the degradation was only the result of photocatalysis without having any thermal effect. Analytical samples for absorption measurement were taken out from the reaction suspension at different time intervals. Optical absorption spectra of the samples were recorded in a UV-Vis 1700 Shimadzu Spectrophotometer. The same process of photocatalytic evaluation is followed for prepared CZ1:1, CZ1:2 and CZ1:3 samples of different morphology and the pH of the above mentioned aqueous solution was kept same (pH 7) for all samples. The photocatalytic activity of samples for the degradation of Phenol in aqueous solution was also evaluated under the visible light irradiation following the above process.

The visible-light photocatalytic activity of CZ1:1, CZ1:2 and CZ1:3 samples was carried out by using it to degrade rhodamine B dye aqueous solution. The degradation of dye was monitored through the change in intensity of the absorption

peak of the RhB. Absorption spectra of the three sample solutions taken at different time (shown in Fig.3.3 a-c)exhibit that at the beginning (t=0) the spectrum shows the intense absorption peak of RhB at 554 nm.

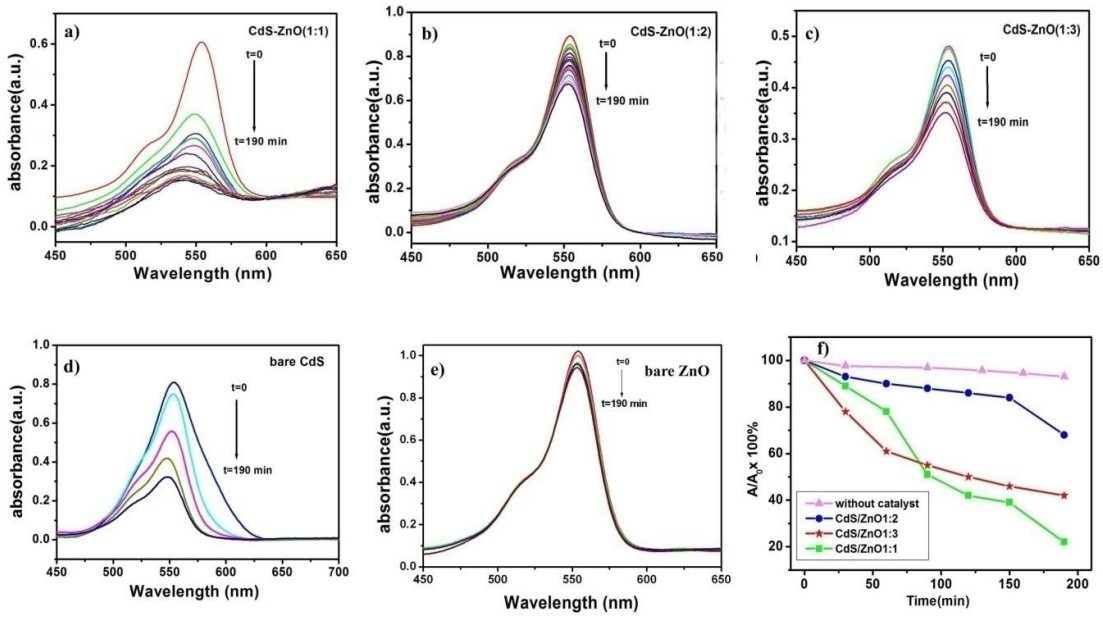

Fig.3.3. Absorption spectra of RhB aqueous solution in presence of CZ1:1(a), CZ1:2(b), CZ1:3(c), CdS(d), ZnO(e) and decrease in normalized absorption intensity with respect to time for three different samples in Phenol aqueous solution (f).

As time prolonged the photocatalysis reaction goes on and the gradual degradation of the organic dye leads to the subsequent reduction of the absorption peak intensity. For CZ1:1 sample, it is seen that the color of the dye is completely faded away after 190 min confirming the complete degradation of the dye molecules. But the dye degraded up to only ~25% for CZ1:2 and ~40% for CZ1:3 within the measurement duration of 190 min. Among these three unique morphologies, compact flowerlike structure in CZ1:1 sample exhibits much faster degradation than others. The higher degradation

capacity of the flower like structure of CZ1:1 nanocomposite may be attributed to the highest surface integration in the unit structures which facilitate effective separation and transfer of the photo generated charges in the catalyst. As photocatalytic performance for composite materials largely depends on their interface so the higher the interface area the better will be the catalytic activity. Here also in CZ1:1, the texture is very well defined and CdS - ZnO interface is perfectly integrated. So the best performance comes from this composite. In case of CZ1:2, the composite gets loosly bounded flower like structure which has poor interface between CdS and ZnO. In CZ1:3 composite though the texture is like scattered flower with some dissociated ZnO petals still the effective interface area between CdS and ZnO is higher than 1:2 composite. So evidently the photocatalytic activity with CZ1:3 comes better than that of CZ1:2 composite structure for RhB and Phenol degradation. The influence of morphology on photocatalytic activities has also been investigated for some other systems like TiO_2[16], Cu_2O[17], ZnO[18] and Ag_3PO_4[19]. But here the study shows the value of morphology and compactness for heterostructured photocatalysts. Experiments without radiation of visible light in the presence of catalyst and with radiation of visible light without the presence of catalyst have also been carried out and the degradation is negligible. The percentage of degradation measured at different time was calculated by normalizing the peak intensity in term of the starting (t = 0) peak intensity of RhB with three catalysts. Decrease in normalized absorption intensity of RhB with respect to time for three samples is shown in Fig.3.4(a). The photocatalytic measurement of bare CdS and ZnO nanoparticles have been also carried out for RhB in the similar method for the comparision. As expected, the result (see Fig. 3.3d-e) does not exhibit any appreciable dye degradation for ZnO but moderate catalytic performance of CdS nanaoparticles has been observed. It shows almost 61%

degradation of RhB in visible light irradiation within the stipulated time. The result reflects that bare CdS nanoparticle is better than CZ1:2 and CZ1:3 but CZ1:1 is much better than CdS nanoparticle in photocatalytic dye degradation due its synergistic effect. Here it is worthy to point out that rational question has already been raised [20] on the suitability of taking photosensitizable molecule (like MB, RhB etc) for clearly understanding the underlying photocatalytic reaction. So another probe molecule phenol has been employed to investigate the true photocatalytic capacity of the CdS/ZnO nanocomposite. Decrease in normalized absorption intensity of phenol with respect to time for three samples is shown in Fig.3.3(f). Again CZ1:1 exhibits the best catalytic activity with almost 78% degradation of phenol within stipulated time of 190 minutes. Compare to CZ1:2, CZ1:3 shows better performance in photocatalytic degradation of standard phenol. The findings confirm our previous result with RhB that shows excellent photocatalytic activity of CZ1:1 nanocomposite.

Pseudo first order kinetic plot for the photocatalytic degradation of RhB of as synthesized CZ1:1, CZ1:2 and CZ1:3 samples are shown in Fig. 3.4(b). The rate constants are found to be 0.01333/min, 0.00113/min and 0.00224/min for CZ1:1, CZ1:2 and CZ1:3 respectively. The fact is that in the CdS/ZnO composite the photo generated excitons are developed in CdS part and the existence of well integrated ZnO crystals supports the efficient separation and transfer of the electrons. As stability is a major issue for an efficient photocatalyst, the best performer in the series, CZ1:1 has been taken to carried out photocatalytic degradation of RhB for ten cycles. The result shows (Fig. 3.5) that after ten cycles the degradation percentage of RhB decreases from 90 to 79 reflecting that CZ1:1 catalyst is moderately robust in normal pH.

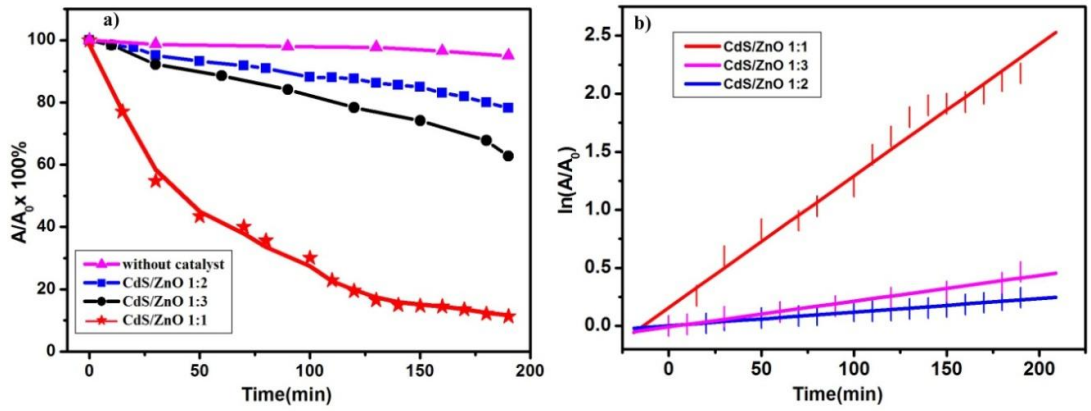

Fig.3.4. Decrease in normalized absorption intensity with respect to time for three different samples in presence of visible light (a); first order kinetic plot for the photocatalytic degradation of RhB for three samples (b).

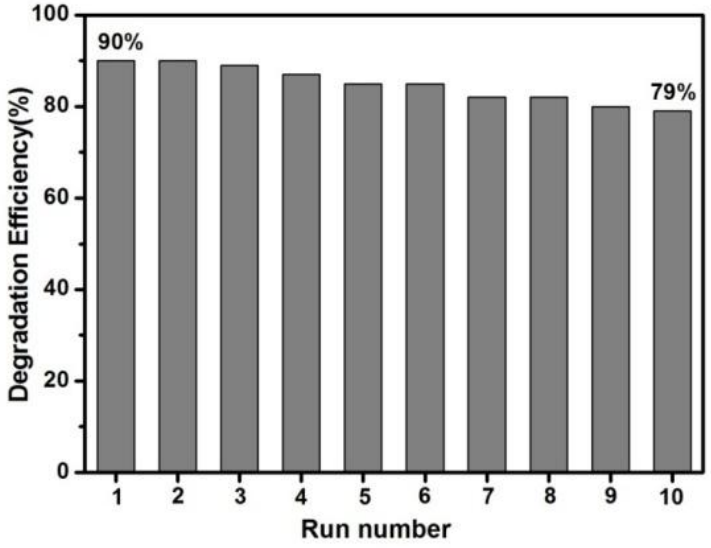

Fig.3.5. Stabilty test of CZ1:1 nanocomposite for ten consequtive cycles measured in terms of percentage of RhB degradation under visible light irradiation.

The figure 3.6(a) shows different absorption spectrum of the sample solution taken at different times. The inset of figure 3.6(a) presents the photograph of the dye with catalyst at starting time and after 190 min of light exposure for CZ1:1. It is seen that the color of the dye is completely faded away confirming the degradation of the dye molecules. The percentage of degradation measured at different time was calculated by normalizing the peak intensity in term of the starting (t=0) peak intensity of RhB with catalyst. Experiments without radiation of light in presence of catalyst and with radiation of light without the presence of catalyst have also been done. All these data in terms of degradation percentage is presented in figure 3.6(b).

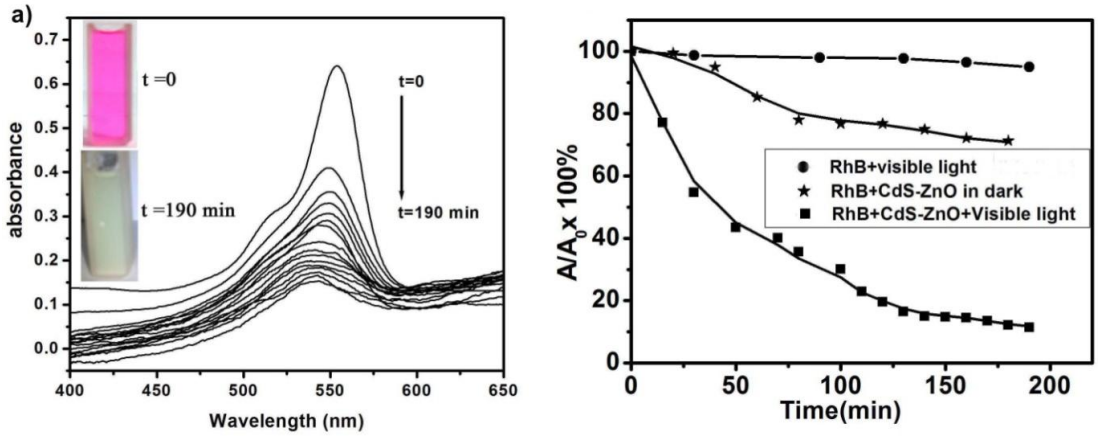

Fig. 3.6. Absorption spectra of rhodamine B aqueous solution in presence of CdS–ZnO during illumination (a); Decrease in normalized absorption intensity of rhodamine B with respect to time for different cases. Inset in (a) panel shows the photograph of RhB in presence of CdS–ZnO at starting and ending time of illumination.

It is seen that as expected there is no change in degradation of RhB when it is exposed to light without catalyst. In case of RhB with CdS-ZnO catalyst without light radiation there is little change and the dye degraded up to 24% within the measurement duration of 190 min. It seems the catalytic effect of the prepared compound semiconductor is responsible for the slight degradation of this organic dye. But the noteworthy thing is that when the dye with sample is exposed in light the degradation rate is extremely fast and dye is almost completely (90%) decomposed within 190 min. Here it is clear that CdS-ZnO1:1 works as strong photo-catalytic agent decolorizing RhB taken as model organic pollutant. The degradation rate constant was calculated from the slope obtained by linear regression from a plot of the natural logarithm of the normalized absorbance as a function of irradiation time [21]. The rate constant is found to be 0.0133/min which is better [22] or comparable [23] to the reported TiO_2 based highly photocatalytic materials. In case of ZnO/CdS system, Ravishankar and his team have shown ZnO/CdS heterostructures with engineered interfaces for high photocatalytic activity and our degradation rate constant is in close match to that of the best sample in the reported series [24]. ZnO/CdS core shell nanorods have also been attempted with variable shell thicknesses to tune the photocatalytic efficiency and it was found that the photodegradation of RhB is better for the higher thickness of CdS shell around ZnO nanorods [25]. Nozaki et al have demonstrated photocatalytic degradation of 3-4-dihydroxy benzoic acid by CdS-ZnO nanorods, chemically grown on indium tin oxide, but their also it takes comparatively long time (~20hr) to reach the sensible degradation of the dye [26]. ITO/CdS/ZnO composite films were employed for the degradation of methyl orange and the result exhibited that the films prepared under specific conditions have shown higher photocatalytic activity following pseudo first

order kinetics of degradation [27]. In our system the structure is unique and the photodegradation capacity is also impressive.

To address the photocatalytic effect in details we propose a possible charge transfer mechanism in our synthesized system and it is shown in figure 3.7(a) as a modified energy band diagram, presented on the canvas of the synthesized materials.

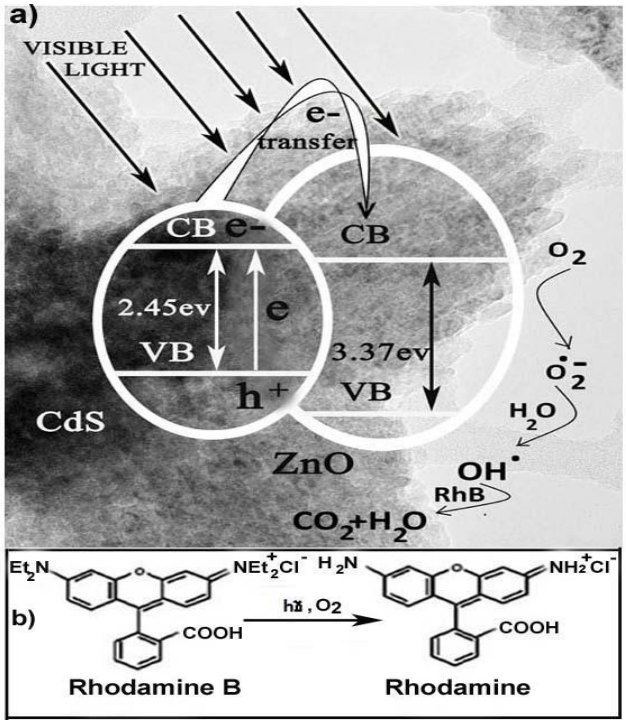

Fig. 3.7. The schematic photodegradation process in the CdS–ZnO/RhB aqueous solution (a); N-deethylation of rhodamine B to rhodamine (b).

The band position of CdS-ZnO system [25,28,29] clearly elucidate the feasibility of charge transfer from CdS to ZnO due to more negative potential of CB and VB edges of CdS than those of ZnO. Furthermore for enhanced photoresponse a faster rate of charge transport is needed and it is facilitated by the intimate and effective contact of the hybrid materials. Here the flower like structure of CdS-ZnO provides the

opportunity for better intersystem electron transfer. According to Anderson's model type II heterojunction is formed between CdS and ZnO. Visible light from halogen lamp generates electron-hole pair in CdS and the photogenerated electrons in CdS core can easily move to ZnO petals by the process of ballistic diffusion [26]. Once the electrons diffuse into the conduction band of ZnO the recombination probability becomes small as there can be no free hole in ZnO under visible excitation. On the other hand remaining part of the photogenerated excitons i.e. holes are accumulated in the VB of CdS as they cannot move towards more positive VB of ZnO. Now the holes in VB of CdS can react with water adhering to the surface to convert the OH into highly reactive $OH^{\bullet}$ and electrons in CB of ZnO can potentially convert the dissolved oxygen into highly oxidative radicals $O_2^{\bullet-}$ which in turn produces $OH^{\bullet}$ [23,30]. This $O_2^{\bullet-}$ can react with a H^+ of solvent water to form $OOH^{\bullet}$ and this $OOH^{\bullet}$ can eventually generate H_2O_2 and finally $OH^{\bullet}$. The strong $OH^{\bullet}$ radicals decompose the organic dye. It is also reported [31] that $OOH^{\bullet}$ and $OH^{\bullet}$ are necessary to N-deethylation of RhB which is the basic requirement for the complete degradation of the dye. Figure 3.7(b) shows the N-deethylation of RhB to Rh [32]. In this way photogenerated electrons and holes in the synthesized CdS-ZnO nanoflower system effectively degrade the organic dye and present the system as a potential material for future study.

3.2 Photocatalytic Property of Co_3O_4-ZnO nanocomposite:

The photocatalytic activity of Co_3O_4-ZnO nanocomposite system was measured by the degradation of RhB in aqueous solution under halogen lamp radiation. In a typical process 10 μM solution of RhB in DI water was taken and the Co_3O_4-ZnO nanocomposite sample was added to it to maintain a catalyst concentration of 1g L^{-1}.

To reach equilibrium condition the organic dye with catalyst solution was stirred in dark for 1 hr and after 1hr of stirring no significant change was observed. The solution was then exposed to 1000 Watt halogen lamp radiation. Actually the radiation from halogen lamp in the NIR region has some heating effect. To ensure that the degradation was only the result of photocatalysis without having any thermal effect, the beaker was kept in a cold water bath to maintain the reaction temperature at 290K. The zero time reading was obtained from the sample solution taken just before turning on the light [21]. Henceforth the sample was taken from the mother solution under the light radiation in regular interval to measure the optical absorbance. Figure 3.8a shows different absorption spectrum of the sample solution taken at different times. At the begining (t=0) the spectrum shows the intense absorption peak of RhB at 554nm. With the passage of time the photocatalytic reaction continues and the gradual degradation of the organic dye leads to the subsequent reduction of the absorption peak intensity. The inset in this figure shows the photograph of the dye with catalyst at starting time and after 400 min of light exposure. It is seen that the color of the dye is completely faded away confirming the degradation of the dye molecules. The percentage of degradation measured at different time was calculated by normalizing the peak intensity in term of the starting (t=0) peak intensity of RhB with catalyst. Experiments without radiation of light in presence of catalyst and with radiation of light without the presence of catalyst have also been done. All these data in terms of degradation percentage is presented in figure 3.8b.

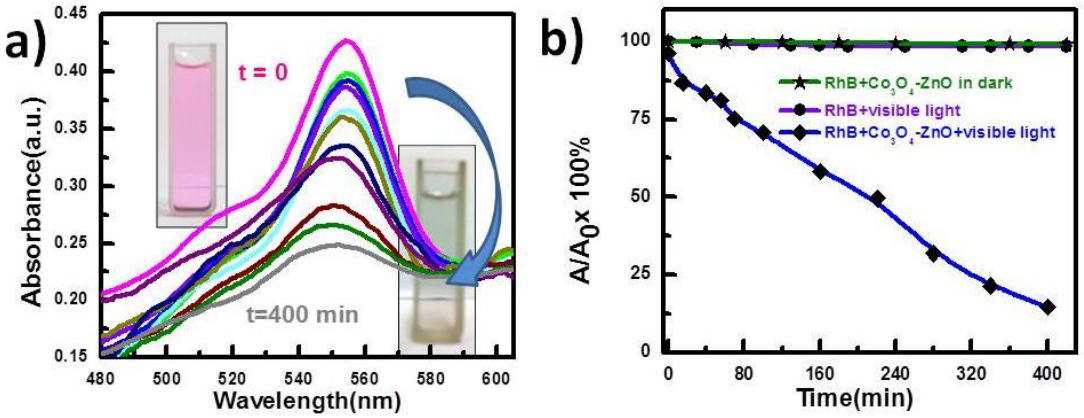

Fig. 3.8. Absorption spectra of rhodamine B aqueous solution in presence of Co_3O_4-ZnO nanocomposite during illumination (a); Decrease in normalized absorption intensity of rhodamine B with respect to time for different cases. Inset in (a) panel shows the photograph of RhB in presence of Co_3O_4-ZnO nanocomposite at starting and ending time of illumination.

It is seen that as expected there is no change in degradation of RhB when it is exposed to light without catalyst and in case of RhB with Co_3O_4-ZnO catalyst without light radiation. But when the aquous solution of dye with sample is exposed in light the degradation rate is quite fast and dye is almost completely (89%) decomposed within 400 min. Here it is clear that Co_3O_4-ZnO works as strong photocatalytic agent and decolorize RhB which was taken as model organic pollutant. Here it is worthy to mention that photocatalytic activity of bare Co_3O_4 and bare ZnO have also been tested but the performances are not at all comparable to the composite material.

To understand the photocatalytic effect in details we propose a possible charge transfer mechanism in our synthesized system and it is shown in figure 3.9 as a modified energy band diagram. The band position of Co_3O_4-ZnO system [33] clearly elucidates the feasibility of charge transfer from Co_3O_4 to ZnO. The CB and VB edges of Co_3O_4 are in more negative potential than those of ZnO. Moreover for enhanced photoresponse a faster rate of charge transport is needed and it is supported here by the intimate surface contact of the hybrid materials.

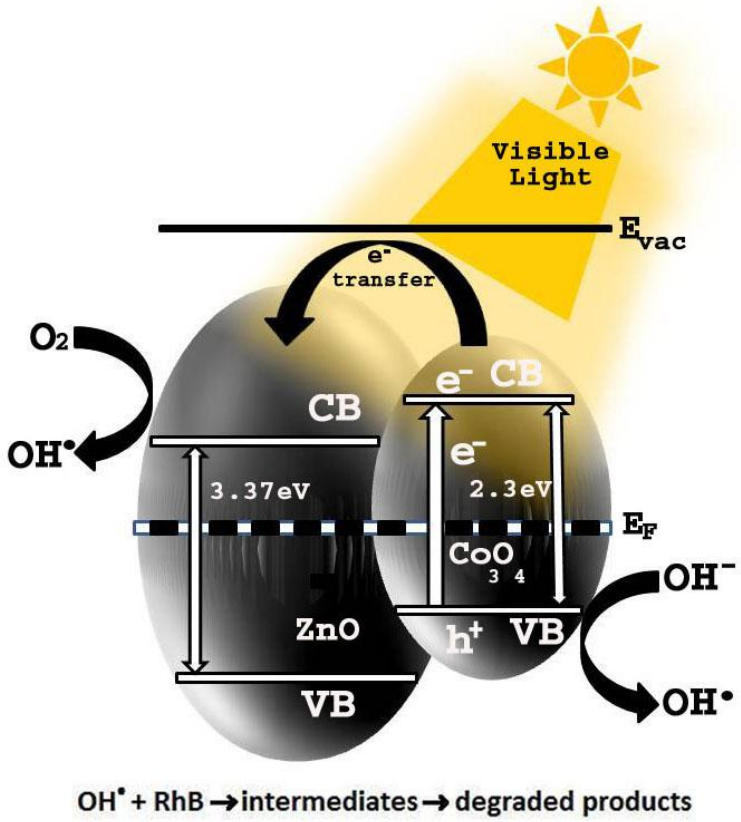

Fig. 3.9. The schematic photodegradation process in the Co_3O_4-ZnO/RhB aqueous solution in presence of light.

Synthesized Co_3O_4-ZnO nanocomposites provide the opportunity for better intersystem electron transfer. Visible light from halogen lamp generates electron-hole pair in Co_3O_4 and the photogenerated electrons in Co_3O_4 can quickly transferred to CB of ZnO. Once the electrons diffuse into the conduction band of ZnO the recombination probability becomes small as there can be no free hole in ZnO under visible excitation. On the other hand remaining part of the photogenerated excitons i.e. holes are accumulated in the VB of Co_3O_4 as they cannot move towards more positive VB of ZnO. Now the holes in VB of Co_3O_4 can react with water adhering to the surface to convert the OH into highly reactive $OH^{\bullet}$. It is possible that the holes directly oxidize the organic dye molecule. On the other hand excessive electrons in CB of ZnO are scavenged by dissolved oxygen molecules only to yield highly oxidative $O_2^{\bullet-}$ radicals which in turn produces $OH^{\bullet}$ [34-35]. This $O_2^{\bullet-}$ can react with an H^+ of solvent water to form $OOH^{\bullet}$. The $OOH^{\bullet}$, reacting further with water molecule, can generate H_2O_2 and eventually H_2O_2 produces $OH^{\bullet}$. The strong $OH^{\bullet}$ radicals reacts with RhB and decomposes it by producing CO_2 and H_2O. $OOH^{\bullet}$ and $OH^{\bullet}$ both are necessary to N-deethylation of RhB which is the basic requirement for the complete degradation of the dye [36]. In this way photogenerated electrons and holes in the synthesized Co_3O_4-ZnO nanocomposite system effectively degrade the organic dye and present the system as a potential material for future study.

References:

1. E. Bequerel, C.R.Acad.Sci.(Paris) 9, 145 (1839).
2. W. Doerfler, K. Hauffe, J. Catal. 3, 171 (1964).
3. A. Fujishima, K. Honda, Nature 238, 37 (1972).
4. Q. Yin, R. Qiao, Z. Li, X. L. Zhang, L. Zhu, J. Alloys Comp. 618, 318 (2015).
5. P. Salvador, J. Phys. Chem. C 111, 17038 (2007).
6. A. Fujishima, X. Zhang, D. Tryk, Surf. Sci. Rep. 63, 515 (2008).
7. D. Bahnemann, Sol. Energy 77, 445 (2004).
8. D. Friedmann, C. Mendive, D. Bahnemann, Appl. Catal. B Environ. 99, 398 (2010).
9. P. Pichat, Wiley-VCH, Weinheim (2013).
10. S. Ahmed, M. G. Rasul, R. Brown, M. A. Hashib, J. Environ. Manage. 92, 330 (2011).
11. J. M. Herrmann, Top Catal. 34, 49 (2005).
12. J. M. Herrmann, Appl. Catal. B Environ. 99, 461 (2010).
13. P. A. K. Reddy, P. V. L. Reddy, E. Kwon, K.-H. Kim, T. Akter, S. Kalagara, Environment International 91, 94 (2016).
14. C. Su, C. Shao, Y. Liu, Journal of Colloid and Interface Science 359, 220 (2011).
15. A. Pal, T.K. Jana, K. Chatterjee, Mater. Res. Bull. 76, 353 (2016).
16. Z. Wei, E. Kowalska, J. Verrett, C. Colbeau-Justin, H. Remitab, B. Ohtania, Nanoscale 7, 12392 (2015).
17. L. Feng, C. Zhang, G. Gao, D. Cui, Nanoscale Res. Lett. 7, 276 (2012).
18. J. Gupta, P. Bhargava, D. Bahadur, Physica B 448, 16 (2014).

19. P. Dong, Y. Wang, H. Li, H. Li, X. Ma, L. Han, J. Mater. Chem. A 1 4651 (2013).
20. X. Yan, T. Ohno, K. Nishijima, R. Abe, B. Ohtani, Chem. Phys. Lett. 429 606 (2006).
21. M. Qamar, S.J. Kim, A.K. Ganguli, Nanotechnology 20, 455703 (2009).
22. J.M. Wu, T.W. Zhang, J. Photochem. Photobiol. A: Chem. 162, 171 (2004).
23. P. Wilhelm, D. Stephan, J. Photochem. Photobiol. A: Chem. 185, 19 (2007).
24. P. Kundu, P.A. Deshpande, G. Madras and N. Ravishankar, J. Mater. Chem. 21, 4209 (2011).
25. S. Khanchandani, S. Kundu, A. Patra and A.K. Ganguli, J. Phys. Chem. C 116, 23653 (2012).
26. J. Nayak, S. N. Sahu, J. Kasuya and S. Nozaki, Appl. Surf. Sci. 254, 7215 (2008).
27. S. Wei, Z. Shao, X. Lu, Y. Liu, L. Cao and Y. He, J. Environ. Sci. 21, 991 (2009).
28. D. Barpuzary, Z. Khan, N. Vinothkumar, M. De and M. Qureshi, J. Phys. Chem. C 116, 150 (2012).
29. P. Sudhagar, S. Chandramohan, R.S. Kumar, R. Sathyamoorthy, C.H. Hong and Y.S. Kang, Phys. Status Solidi A 208, 474 (2011).
30. M.W. Xiao, L.S. Wang, Y.D. Wu, X.J. Huang, Z. Dang, Nanotechnology 19, 015706 (2008).
31. P. Qu, J. Zhao, T. Shen, H. Hidaka, J. Mol. Catal. A: Chem. 129, 257 (1998).

32. G. Schmid, Nanoparticles, Wiley-VCH, Weinheim, (2004).
33. M.A. Kanjwal, F.A. Sheikh, N.A.M. Barakat, X. Li, H.Y. Kim, I.S. Chronakis, J. of Nanoeng. and Nanomanuf. 1, 196 (2011).
34. P. Wilhelm, D. Stephan, J. Photochem. Photobiol. A: Chem. 185, 19 (2007).
35. M.W. Xiao, L.S. Wang, Y.D. Wu, X.J. Huang, Z. Dang, Nanotechnology 19, 015706 (2008).
36. P. Qu, J. Zhao, T. Shen, H. Hidaka, J. Mol. Catal. A: Chem. 129, 257 (1998).

CHAPTER 4

MAGNETIC PROPERTY OF NANOCOMPOSITE

5.1 Magnetic Characteristics of Co_3O_4-ZnO nanocomposite

Certain atoms whose energy levels are not totally filled have a net magnetic moment and behave like small bar magnets. Atoms in the various transition series of the periodic table having unfilled inner energy level in which the spins of the electrons are unpaired, have a net magnetic moment. In case of iron atom, the d level contains only 6 of the possible 10 electrons. Due to this incompletely filled electron d shell iron atom has a strong magnetic moment. When crystals are formed from atoms having a net magnetic moment, a number of different arrangements can occur according to the alignment of magnetic moment of the individual atoms with respect to each other. If the magnetic moments are randomly arranged with respect to each other, then the crystal has a zero net magnetic moment and is called *paramagnetic*. When a DC magnetic field is applied on a paramagnetic crystal, some of the moments are aligned, giving the crystal a small net moment. *Ferromagnetic* crystal retains a component of magnetization in the direction of the applied DC magnetic field after the field is removed and behaves like a bar magnet producing a magnetic field outside of it[1-2]. Magnetic moments in ferromagnetic crystals are equal in magnitude and aligned parallel relative to each other. *Ferrimagnetic* crystal is made of two types of atoms, each having a magnetic moment of a different strength. This type of crystal will also have a net magnetin moment and behave like a bar magnet. In case of *antiferromagnetic* crystal the magnetic moments are arranged opposite to each other, that is, in an antiparallel arrangement. Such a crystal has no net magnetic moment. In addition, *diamagnetic* substances are composed of atoms with closed electronic shells and hence no net magnetic moment.

When dealing with magnetic properties, it is needed to define permeability μ of the material and magnetization M. Permeability μ describes material's response to an external field and magnetization M is the magnetic moment per unit volume. The magnetic susceptibility χ is the change in magnetization M with magnetic field strength H

$$X= dM/dH$$

Ferromagnetic crystals have an ordering temperature called the Curie temperature(Tc) above which they are paramagnetic and antiferromagnetic crystals have an analogous temperature, the Neel temperature (T_N)[3-4], above which they are also paramagnetic. Generally in a bulk ferromagnetic material the microscopic ordering of electron spins results in the formation of regions of magnetic alignment known as magnetic domains. Domains are separated from each other by domain walls. In a domain all the atomoic moments point in the same direction so that within each domain the magnetization is saturated, that is, it attains a maximum possible value. The magnetization vectors of different domains in the material are not all parallel to each other. As a result the material has an overall magnetization less than the value for the complete alignment of all moments. When a strong DC magnetic field (H) is applied, magnetization M increases with the increase of H until a saturation point M_S , is reached. As H is decreased, M does not decrease to the same value having in time of increasing field. It is higher on the curve of the decreasing field. This phenomenon is called hysteresis. Domains that were aligned with the increasing field do not return to their original orientation when the field is decreased. When the applied field H is returned to zero value, magnetization still exists in the magnet. This is referred to as remnant magnetization M_r. To remove the remnant magnetization, a field H_c which is called

coercive field, has to be applied in opposite direction[5]. H_c causes the domains to rotate back to their original positions. Shi et al.[6] investigated the magnetic properties of α-Fe_2O_3 nanoparticles coated with silica of different thickness.The hysteresis phenomenon was observed for this α-Fe_2O_3/SiO_2 nanocomposite shown in figure 4.1.

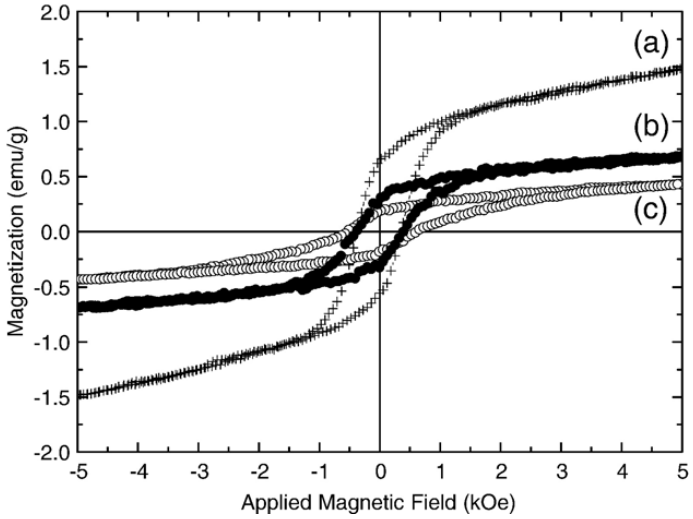

Fig. 4.1. Hysteresis loop of the (α-Fe_2O_3) particles and Fe_2O_3/SiO_2 nanocomposite. (a) Fe_2O_3-core, (b) Fe_2O_3/SiO_2-thin shell, (c) Fe_2O_3/SiO_2-thick shell. Reprinted from [6], Copyright (2007), with permission from Elsevier.

Magnetic nanoparticles exhibit markedly different properties from the bulk counter parts. The hysteresis loop parameters such as the coercivity and remanence become modified significantly. The magnetic nanoparticles become a single domain and therefore maintain a large magnetic moment. They display the phenomenon of superparamagnetism(SPM)[7-8], not keeping magnetized after the action of magnetic field, offering advantage of reducing risk of particle aggregation. Like paramagnetic behavior, superparamagnetic materials retain no magnetization upon removal of a magnetic field[105]. In case of superparamagnetism, coercive field and remanent magnetism are not observed upon removal of field. Usually superparamagnetism can

be realized in magnetic crystal with sizes typically <30nm. If the thermal energy is greater than the crystalline anisotropy energy, then the magnetization can be randomized and if thermal energy is less than the anisotropic energy, then the magnetic moment can not be randomized or it is said to be blocked in one of the easy axis directions. The temperature at which anisotropic energy becomes equal to the thermal energy is known as blocking temperature(T_B). The superparamagnetic transition is observed at the Blocking temperature (T_B)[5,9]. A critical volume for a material with definite anisotropy, to remain superparamagnetic is given by $V_P = 25K_BT/K$ which gives the upper limit of superparamagnetism, where K_B is Boltzmann's constant, T is the temperature and K is the anisotropy constant. Blocking temperature in magnetic nanoparticles can be measured by studying magnetization with respect to temperature without perturbing the system. The sample under study should be cooled in the absence of magnetic field and while warming with a small magnetic field, the magnetization should be analyzed. This is referred to as zero field cooled (ZFC) measurement. In ZFC study maximum magnetization corresponds to the blocking temperature (T_B). Measurement in field cooled (FC) study is recorded while warming and the bifurcation at T_B in ZFC and FC curves could be observed in SPM nanoparticles. The distribution of particle size in the material is obtained from the deviation in the temperature at magnetization maxima in ZFC and the magnetization bifurcation in ZFC and FC. In addition, the bifurcation in the ZFC and FC measurements could be seen both in SPM and spin glass(SG) systems. Zhu et al.[10] demonstrated the temperature dependence of the magnetization in a weak applied field of 100Oe which is shown in figure 4.2.

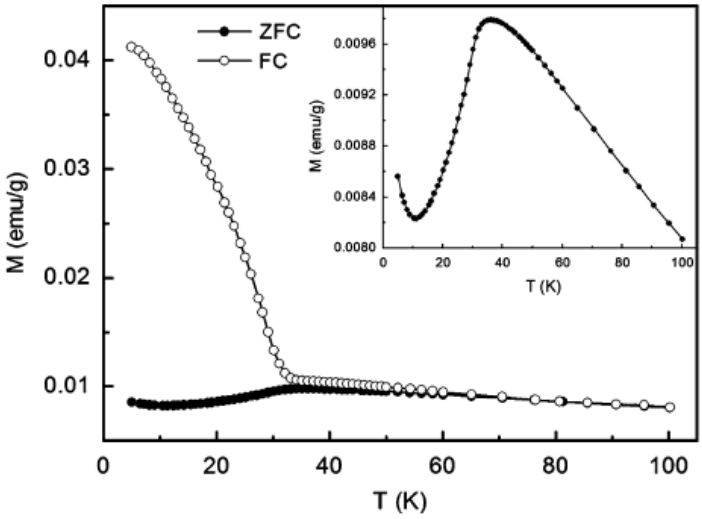

Fig. 4.2. Temperature dependence of the ZFC and FC magnetization curves of Co_3O_4 nanoparticles in an applied field of 100 Oe. The inset is the ZFC curve showing a broad peak around 37 K. Reprinted from [10], Copyright (2008), with permission from Elsevier.

The magnetic properties of nanoparticles are determined the chemical composition, the type and the degree of defectiveness of the crystal lattice, the particle size and shape, the morphology, the interaction of the particle with the surrounding matrix and the neighbouring particles. One can control to an extent the magnetic characteristics of the material based by changing the nanoparticle size, shape, composition and structure. Magnetic nanoparticles are abundant in nature and are observed in many biological objects. Magnetic nanomaterials are used in information recording and storage systems, in new permanent magnets, in magnetic cooling systems, as magnetic sensors, and especially for biological applications.

4.1 Magnetic Characteristics of Co_3O_4-ZnO nanocomposite :

Figure 4.3 shows the *M-T* and *M-H* variation of prepared Co_3O_4-ZnO nanocomposite. The upper panel shows the variation of M_{ZFC} and M_{FC}. Here it is worthy to note that ZnO has no magnetic effect but Co_3O_4 does have its own magnetic behavior. For the better understanding of the magnetic property after the Co_3O_4-ZnO nanocomposite formation, the *M-T* behavior of bare Co_3O_4 nanoparticls is also plotted in the inset of upper panel.

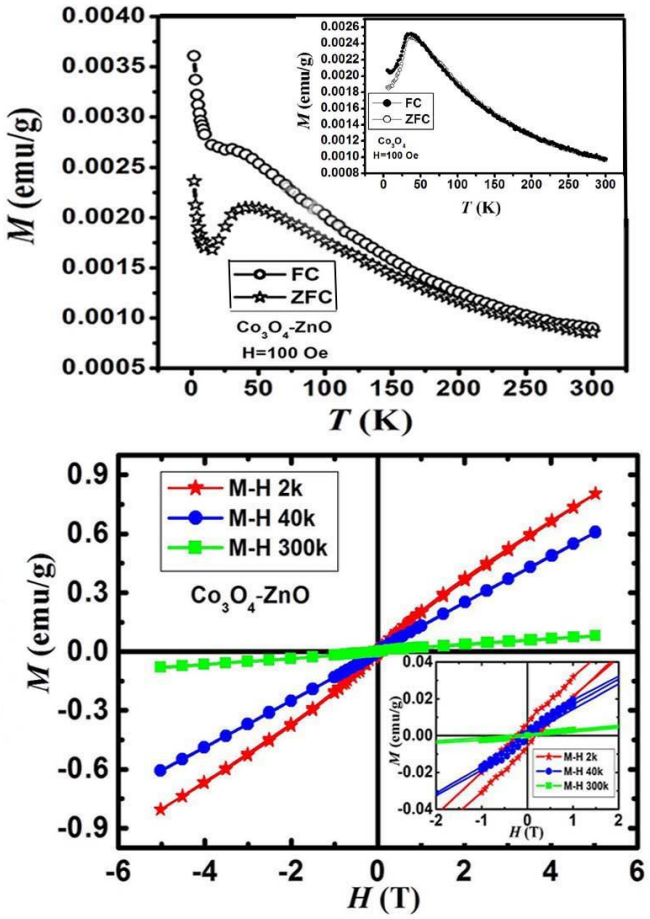

Fig. 4.3. Variation of MZFC and MFC at 100 Oe (upper panel) and MeH variation at 2 K, 40 K and 300 K of as prepared Co_3O_4-ZnO nanocomposite (lower panel). Inset (upper panel); variation of MZFC and MFC of bare Co_3O_4 nanoparticles at 100 Oe. Inset (lower panel); M-H variation at 2 K, 40 K and 300 K of Co_3O_4-ZnO nanocomposite at higher magnification near the center.

The blocking temperature (T_B) of bare Co_3O_4 nanoparticle was observed nearly at 35K (shown in the inset of upper panel of figure 4.3) and for the Co_3O_4-ZnO nanocomposite, the signature of T_B has been observed at nearly 33K.The Néel temperature of Co_3O_4 bulk crystal is known as, $T_N \sim 40$ K [11] and due to the finite size effect it changes with the particle size [12]. A cooling history dependence of M is much stronger in the nanocomposite case compare to the pure Co_3O_4 nanoparticles as M_{ZFC} and M_{FC} lines are seperated at most of the temperature region in the M-T characteristic. Below 33K the M_{FC} data start to decrease implying antiferromagnetic (AFM) interaction. But the most interesting observation for the Co_3O_4-ZnO nanocomposite sample is that, nearly at 15K both M_{ZFC} and M_{FC} data start to increase rapidly and this behaviour are distinctly different from the magnetic data of bare Co_3O_4 nanoparticle as well as from previous reports of Co_3O_4 systems [13-14]. The rapid increment in the magnetic moment of the materials at this low temperature may be attributed to the interface effect of the composite. Scientists have already probed magnetic behavior at different interfaces, theoretically like Heusler and semiconductor junction [15] as well as experimentally like AFM and FM junctions [16] due to its potential of exhibiting new magnetic phenomena. But very recently, Y. Tokura and his team delineated wide prospect of emerging phenomena at transitional metal oxide interfaces and V. Salgueirino et al precisely demonstrated the ferromagnetic behaviour of Co_3O_4 (AFM) and CoO interface due to their heavily strained, atomically sharp interface [17-18]. In tune with their study, our present spinel / wurtzite type system also provides an attractive oxide interface where electrostatic doping can induce changes of pristine magnetic interactions. Stress generated due to the ZnO shell formation onto the Co_3O_4 core like inner particles makes the interface much irregular

shaped opening the possibility of broken symmetry. At the low thermal energy (< 15K) these surface uncompensated spins behave similarly to ferromagnetic spins, and they can spontaneously be aligned by the external magnetic field.

The *M-H* behavior of Co_3O_4 at 300K, 40K and 2 K is shown in the lower panel of figure 4.3. At 300 K, *M* varies linearly with *H* up to 5T, which suggests the paramagnetic (PM) behaviour of the composite sample. No magnetization saturation for the sample was observed under an applied magnetic field up to 5T, suggesting the progressive spin alignment along the external field. Hysteresis loop is not at all prominent in case 300K and 40K measurements but at 2K the sample shows distinct hysteresis loop with coercivity of 230 Oe and remanence of 0.0065emu/g. It also justifies the spontaneous spin alignment of the sample due to the external magnetic field at low temperature. At temperature higher than ~15K the thermal energy inhibits the alignment of the magnetic spins. Here it is worthy to mention that the sample did not show any signature of exchange bias in *M-H* measurement and this fact discard the presence of frozen-in uncompensated spins at the interface.

References:

1. S. O. Kasap, Electronic Materials and Devices, 598 (2002).
2. A. J. E. Joel, S. Miller, Molecule-Based Magnets - An Overview MRS Bulletin, 21 (2000).
3. G. Group, Magnetism, DISCovering Science, (1996).
4. J. Dobson, Magnetism in Matter and Magnetic Biomaterials, (2000).
5. J. C. Q.A. Pankhurst, S.K. Jones, J. Dobson, Journal of Physics D: Applied Physics 36, R167 (2003).
6. Jen-Bin Shi, Chia-Wei Lee, Jhe-Wei Guo, Min-Jung Cheng, Chien Wu a, Chih-Jung Chen, Yu-Cheng Chen, Ya-Ting Lin, Chung-Chieh Chang, Materials Letters 61, 5268 (2007).
7. C. P. Bean, J. D. Livingston, J.Appl.Phys. 30, 120 (1949).
8. M. Knobel, W. C. Nunes, L. M. Socolovsky, E. De Biasi, J. M. Varg as, and J. C. Denardin, J. Nanoscience and Nanotechnology 8, 2836 (2008).
9. S. W. Marcelo Blatt, E. Domany, Neural Computation 9, 1805 (1997).
10. H.T. Zhu, J. Luo, J.K. Liang, G.H. Rao, J.B. Li, J.Y. Zhang, Z.M. Du, Physica B 403, 3141 (2008).
11. W.L. Roth, J. Phys. Chem. Solids. 25, 1 (1964).
12. L. He, C. Chen, N. Wang, W. Zhou, L. Guo, J. Appl. Phys. 102, 103911 (2007).
13. E.L. Salabas, A. Rumplecker, F. Kleitz, F. Radu, F. Schuth, Nano Lett. 6, 2977 (2006).
14. M.J. Benitez, O. Petracic, H. Tuysuz, F. Schuth, H. Zabel, Europhys. Lett. 88, 27004 (2009).

15. S. Picozzia, A. Continenzaa, A.J. Freeman, J. Phys. Chem. Solids 64, 1697 (2003).
16. K. Chakrabarti, B. Sarkar, V.D. Ashok, K. Das, S.S. Chaudhuri, S.K. De, Nanotechnology 24, 505711 (2013).
17. H.Y. Hwang, Y. Iwasa, M. Kawasaki, B. Keimer, N. Nagaosa, Y. Tokura, Nat. Mater. 11, 103 (2012).
18. Zi-An Li, N. Fontaíña-Troitiño, A. Kovács, S. Liébana-Viñas, M. Spasova, R. E. Dunin-Borkowski, M. Müller, D. Doennig, R. Pentcheva, M. Farle,V. Salgueiriño, Sci. Rep. 5, 7997 (2015).

CHAPTER 5

ANTIBACTERIAL PROPERTY OF NANOCOMPOSITE

5.1 Antibacterial Efficacy Test

5.2 Antibacterial activity of the CdS/ZnO nanocomposite

Most of the articles on Nanotechnology include environmental care and human health. Diagnosis and treatment are the spotlight of these novel technologies for the improvement of human living. Despite of all the efforts, hospital acquired infections or Nosocomial infections still remain among the main leading causes of death all over the world. An infection is considered to be nosocomial if it appears after 48 hours of hospital admission or within 30 days of discharge. A wide range of bacteria, fungi and viral pathogens are responsible for such Infections[1]. Nosocomial infection is a serious problem worldwide, because of treatment increases hospital costs significantly. According to a report implemented by WHO(World Health Organization), 55 hospitals of 14 different countries, showed that 8.7% of hospitalized patients had nosocomial infections (WHO/ CDS/CSR/EPH/2002.12). Bacterial resistance against antimicrobial agents is a fact characterized by partial or total refractoriness of microorganisms. *Staphylococcus aureus* has developed resistance to penicillin and methicilline. This is an acquired resistance, where bacterial DNA mutates. Microbial resistance to antibiotics is a world-wide problem in humans and animals and is continuously increasing. The main risk factor for the increase in the antibiotic resistance is an extensive use of antibiotics. This has lead to the emergence and dissemination of resistant bacteria and resistance genes in animals and humans[2]. With the increase of microbial organisms resistant to multiple antibiotics, and the continuing emphasis on health-care costs, the pharmaceutical companies and the researchers have tried to develop new, effective antimicrobial reagents free of resistance and cost. Nanotechnology is expected to open new avenues to fight and prevent disease using atomic scale tailoring of materials. In the present scenario, Nanobiotechnology, an emerging field of nanoscience, utilizes nanobased-systems for various biomedical applications. It has emerged up as integration between

nanotechnology and biotechnology for developing biosynthetic and environmental-friendly technology for synthesis of nanomaterials. Nanoscale materials have emerged up as novel antimicrobial agents owing to their high surface area to volume ratio and the unique physicochemical characteristics including catalytic activity, optical properties, electronic properties, antibacterial properties and magnetic properties[3-8]. The metallic nanoparticles are most promising as they show good antibacterial properties which is coming up as the current interest in the researchers due to the growing microbial resistance against metal ions, antibiotics and the development of resistant strains[9]. Different types of nanomaterials like copper, zinc, titanium[10], magnesium, gold[11], alginate[12] and silver[9,13-24] show antibacterial activity. Recent studies have demonstrated that Metal oxide nanoparticles[25-40] and nanocomposites [8,9,25,26,38,41]also exhibit excellent antibacterial activity Matai et al.[41] investigated antibacterial activity of Ag-ZnO nanocomposite and a plausible antibacterial mechanism of Ag–ZnO nanocomposites was proposed which is shown in figure 5.1.

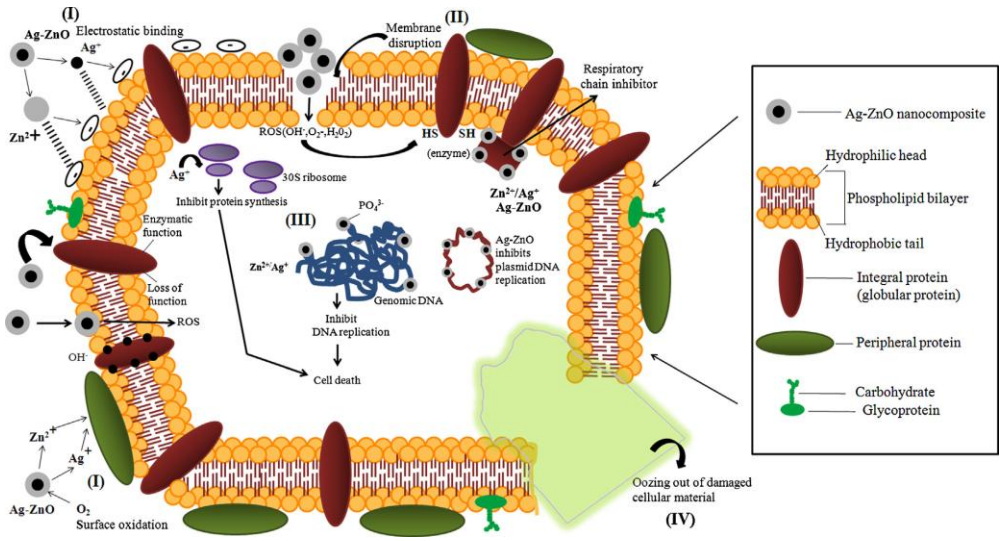

Fig. 5.1. Schematic of possible antibacterial mechanism of Ag–ZnO nanocomposite. Reprinted from [41], Copyright (2014), with permission from Elsevier.

Silver nanoparticles have been employed most extensively among metal nanoparticle antibacterial agents. The exact mechanism of of the antimicrobial effect of silver is still not known but the possible mechanism of action of metallic silver, silver ions and silver nanoparticles have been suggested according to the morphological and structural changes found in the bacterial cells. Several investigation propose that Ag NPs may attach to the surface of the cell membrane disturbing permeability and respiration functions of the cell[42]. Smaller Ag NPs would give more bactericidal effect than the larger Ag NPs due to large surface area available for interaction[42]. It is also proposed that Ag NPs not only interact with the surface of membrane, but can also penetrate inside the bacteria[43]. As an antibacterial agent, in case of E. coli, silver acts by inhibiting the uptake of phosphate and releasing phosphate, mannitol, succinate, proline and glutamine from E. coli cells[44-47]. Thus silver nanoparticles were the effective preventing infection of the wound[48,49]. ZnO nanoparticles have bactericidal properties primarily due to its photocatalytic activity. Destruction of organic material is also possible in a direct reaction with positively charged ZnO particles with bacterial cell. It was observed that ZnO shows bactericidal properties also in case of complete absence of light. Sirelkhatim et al.[50] reviewed the ideas behind the antibacterial activity of ZnO-NPs covering underlying mechanism of evaluating bacteria viability. The noble properties and attractive characteristics of ZnO-NPs confer significant toxicity to organisms, which have made ZnO-NPs successful candidate among other metal oxides. Thus nanostructured materials can act as smart weapon toward multidrug-resistant microorganisms and a talented substitute approach to antibiotics. The toxicological influence of metal, metal oxide NPs should be evaluated to determine the consequences of using these NPs in food safety.

5.1 Antibacterial Efficacy Test:

Microorganisms:

To assess the antibacterial activity of CdS/ZnO samples, *Escherichia coli*, *Staphylococcus aureus* and *Klebsiella pneumoniae* were used as pathogenic microorganisms in this study. The microbial samples were collected from Microbiology Dept. of N. R. S. Medical College & Hospital, Kolkata-14.

Preparation of inoculums:

Bacterial suspension was prepared by taking one or more bacterial colonies from an overnight culture of selective media (Hi-Media, Mumbai) and inserting in a tube with 2 mL of Muller Hinton broth. Turbidity of the suspension was then adjusted to McFarland Nephelo meter = 0.5 ($1.5X10^8$ CFU/mL).[51]

Antibacterial activity assay:

Susceptibility tests were performed by standard well diffusion method against the isolated causative pathogens [52]. A 100 mL of sterilized Muller Hinton agar (Hi-Media, Mumbai) was poured into 180 mm diameter Petri plate to form uniform depth of 4 mm and allowed to solidify. A sterile swab was then dipped into the prepared bacterial suspension, rotated several times and then pressed firmly on the inside of the tube to remove the excess fluid. The swab was then streaked (within 15 - 20 minutes of bacterial suspension preparation) across the surface of the standard test medium consistently by rotating the plate each time to ensure homogeneous distribution of the inoculum onto the surface of the agar plate. After a bacterial inoculation, 8 mm diameter wells were made with a sterilized stainless steel cork borer. The well in each

plate was loaded with a 250 µl of freshly prepared sample suspension (CZ1:1, CZ1:2 and CZ1:3). Suspensions of all samples were prepared by dissolving 100 mg of product in 1 mL sterile distilled water. Simultaneously, the commercially available antibiotic disk like 10mcg Norfloxacin (Hi-media) was used as positive control for the antibacterial assay in this study. The plates were incubated at 37°C for 24 hrs for bacterial growth and inhibition zones were observed. The sensitivity was recorded by measuring the clear zone of growth inhibition on agar surface around the wells.

5.2 Antibacterial activity of the CdS/ZnO nanocomposite:

The antibacterial activity was tested against *Escherichia coli, Staphylococcus aureus* and *Klebsiella pneumoniae* in Muller Hinton agar plates by the well diffusion method. The CdS, CZ1:1, CZ1:2 and CZ1:3 samples were evaluated and displayed in Fig.5.2. The bare CdS and ZnO samples showed no antibacterial activity without light irradiation presented in Fig.5.3(a)-(c) and Fig.5.4(a)-(c) respectively; no inhibition zone was observed for the bacterial strain tested. In contrast, CZ1:1, CZ1:2 and CZ1:3 samples showed a significant inhibitory effect against *Escherichia coli*, *Staphylococcus aureus* and *Klebsiella pneumoniae* bacteria without light irradiation.

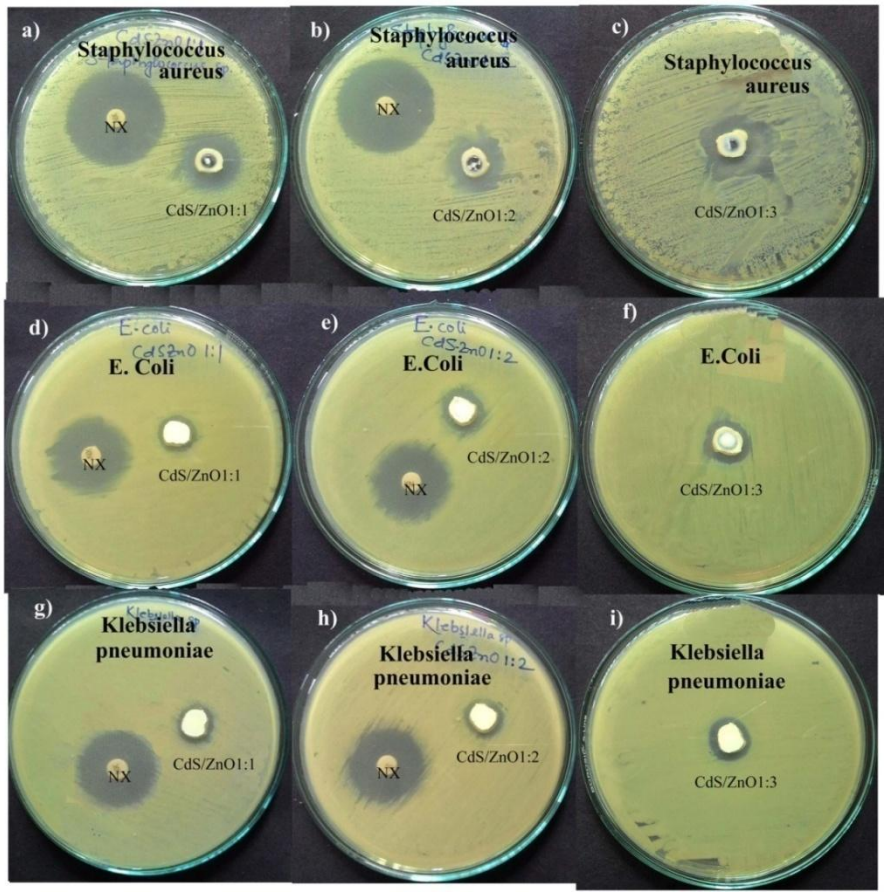

Fig.5.2. Antibacterial activity of CZ1:1 (a), CZ1:2 (b) and CZ1:3 (c) against Staphylococcus aureus; Antibacterial activity of CZ1:1 (d), CZ1:2 (e) and CZ1:3 (f) against Escherichia coli; Antibacterial activity of CZ1:1 (g), CZ1:2 (h) and CZ1:3 (i) against Klebsiella pneumonia; Antibacterial activity of Norfloxacin (NX) as positive control against Staphylococcus aureus (a)-(b), Escherichia coli (d)-(e) and Klebsiella pneumonia (g)-(h).

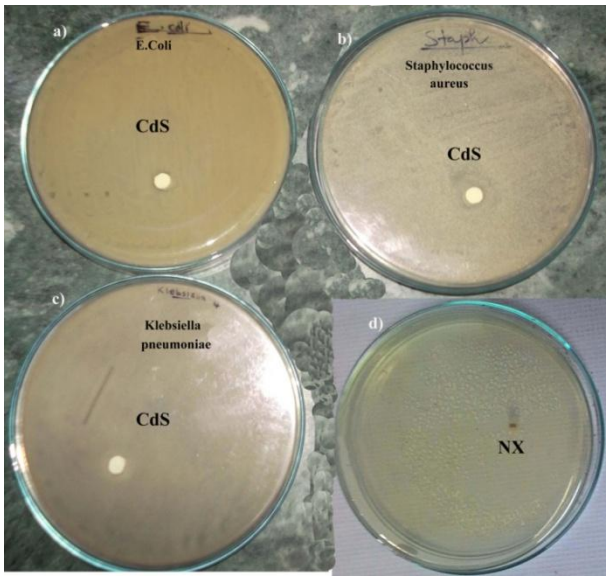

Fig.5.3. No inhibition zone by CdS against *Escherichia coli*(a), *Staphylococcus aureus*(b), and *Klebsiella pneumonia*(c); No inhibition zone by Norfloxacin (NX) Without bacterial inoculation(d).

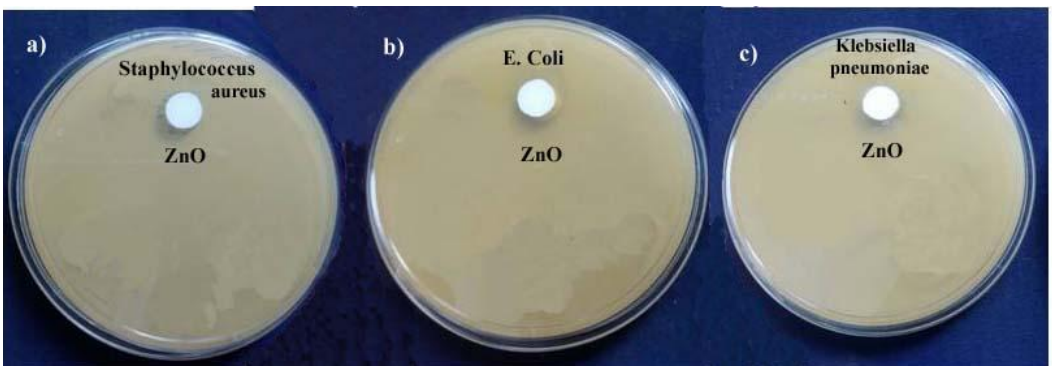

Fig.5.4. No inhibition zone by ZnO against *Staphylococcus aureus*(b), *Escherichia coli*(b), and *Klebsiella pneumonia*(c).

Fig. 5.2 illustrates the images of each inhibition zones for samples and commercially available antibiotic disk for antibacterial activity studies. Norfloxacin (10mcg) were used as control positive for bacterial species for the antibacterial assay due to its high antibacterial outcome. Without bacterial inoculation, Norfloxacin (NX) showed no inhibition zone presented in Fig.5.3(d). Fig. 5.2(a), (d) and (g) showed inhibition zones created by CZ1:1 sample against *Escherichia coli*, *Staphylococcus aureus* and *Klebsiella pneumoniae* respectively. Similarly, Fig. 5.2(b), (e) and (h) display inhibition zones for CZ1:2 sample and Fig.5.2(c), (f) and (i) display inhibition zones for CZ1:3 sample. Fig.5.5 presents the inoculated agar petri plates containing all nanocomposites in the wells before incubation.

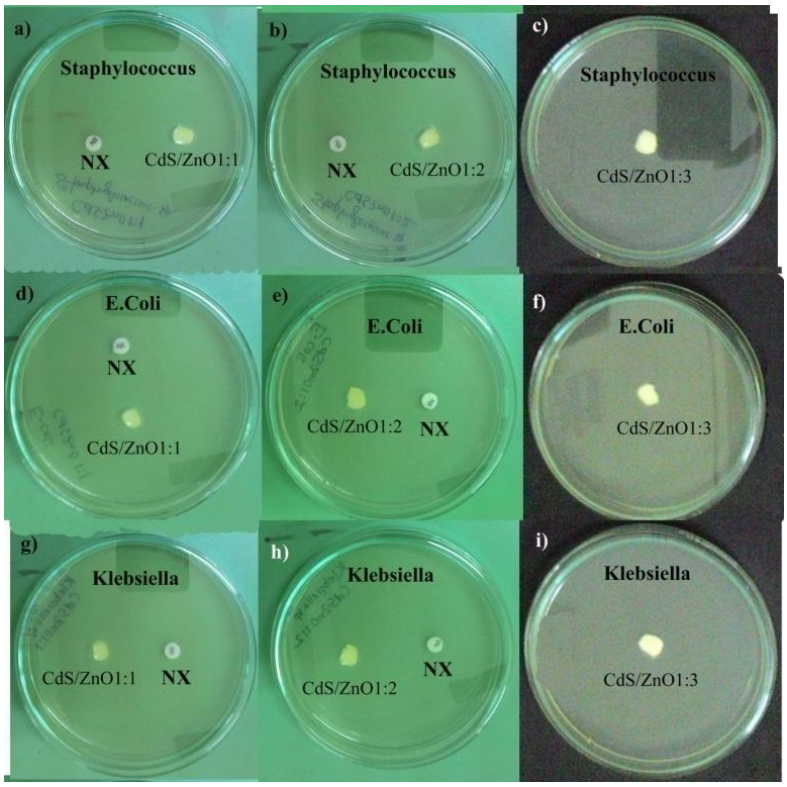

Fig.5.5. Inoculated agar Petri plates containing all nanocomposites in the wells before incubation.

The results of the inhibition zones are presented as average values in mm in the Table 1. The presence of clear zones on the Muller Hinton agar surface proves that the CdS/ZnO nanocomposites were able to inhibit the growth of *Escherichia coli*, *Staphylococcus aureus* and *Klebsiella pneumoniae* whereas no antibacterial activity was detected for the raw CdS and ZnO in dark condition. Zirak et al. also reported that CdS alone exhibited no significant antibacterial activity against bacteria in dark [53] which supports our result. As reported by Prasanna et al. here also bare ZnO also did not show any antibacterial activity in dark[54]. Investigation showed that three nanocomposites showed larger inhibition zones against *Staphylococcus aureus* than *Escherichia coli and Klebsiella pneumoniae.* In addition, CZ1:3 sample exhibits highest inhibition zone (~22 mm) against *Staphylococcus aureus.* Interestingly inhibition zone against all bacteria increases with the nanocomposite containing higher amount of ZnO component. This result indicates that amount of ZnO in the nanocomposite affects the antibacterial activity of the sample against *Escherichia coli*, *Staphylococcus aureus* and *Klebsiella pneumonia.* The resulting antibacterial effect can be explained through the diffusion of the CdS/ZnO nanocomposites over the agar surface, preventing the bacteria growth in the specific area occupied by the nanocomposites. The antimicrobial activity of these nanocomposites, responsible for bacterial cell death, is attributed to several plausible mechanisms (Fig.5.6), like the interaction of nanocomposites with the building elements of the outer membrane/cell wall, causing disruption of the bacterial cell wall by internalization of nanocomposites in bacterial cells, release of Zn^{2+} ions upon surface oxidation, which can damage cell membrane and interact with intracellular contents, electrostatic interactions between the ions released and the negatively charged bacterial cell wall [55-58,41,53]. Furthermore, antibacterial activity of CdS/ZnO samples could be caused by

superoxide anions($\bullet O^{2-}$) generated from ZnO surface in the dark [59,56]. All these will lead to the inhibition and death of the bacteria.

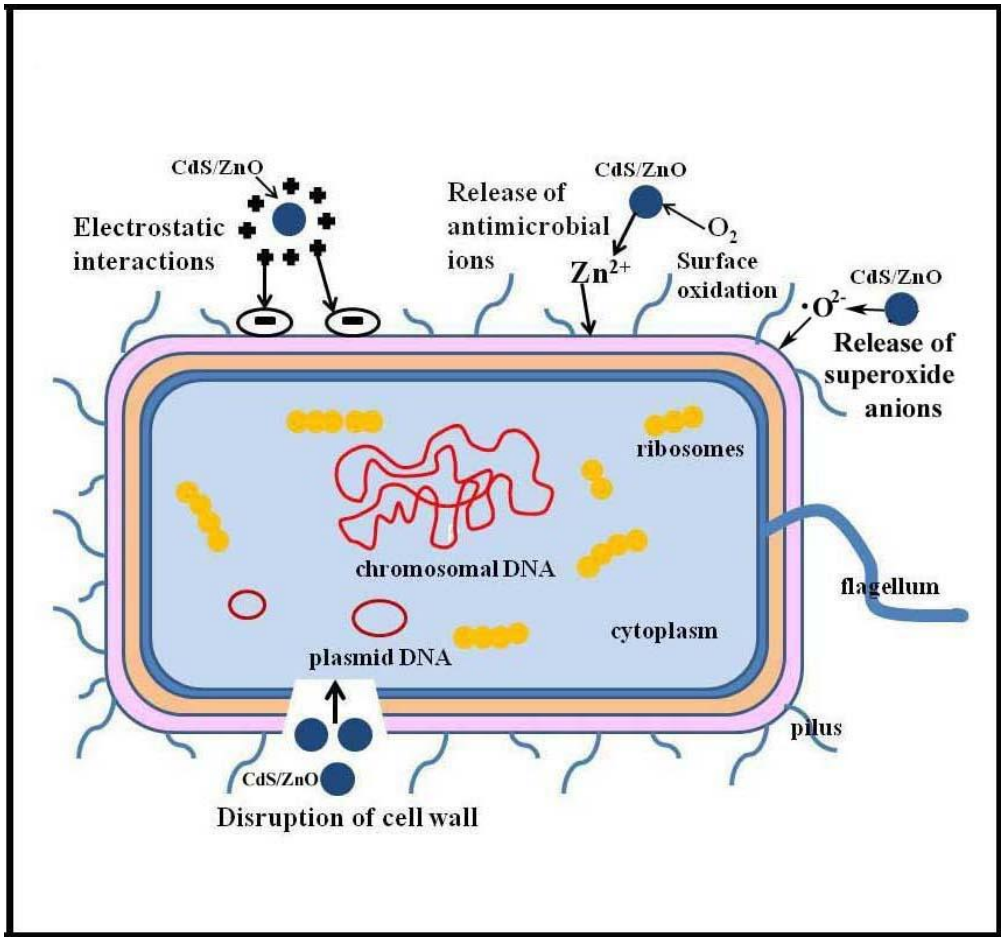

Fig.5.6. schematic representation of various mechanisms of antimicrobial activity of CdS/ZnO nanocomposites.

Although the exact mechanism of action of CdS/ZnO nanocomposites is not known precisely, but CdS/ZnO nanocomposites with 1:3 ratio showed performance as good as commercial antibiotics. As a whole the composites show better activity against Gram-positive bacteria (*Staphylococcus aureus)* than Gram-negative bacteria(*Escherichia coli and Klebsiella pneumonia)* which may be explained by the differences in the

chemical nature of the material present in the outer membrane and cell wall of microorganisms. This preliminary result demonstrates the potential application of CdS/ZnO nanocomposites as an effective antibacterial agent against *Staphylococcus aureus, Escherichia coli and Klebsiella pneumonia*. Future efforts, however, are still needed to further study the antibacterial mechanisms as well as to understand why the CZ1:3 nanocomposite would offer synergistic better antibacterial effect in comparison to CZ1:1 and CZ1:2.

Table 1. Zone of inhibition (ZOI) for *Escherichia coli, Staphylococcus aureus* and *Klebsiella pneumonia.*

Bacteria used in same concentration(1.5 X 10^8/mL)	**Inhibition zone of different antibacterial agents in millimetre (mm)**			
	Control positive NX	**CdS/ZnO 1:1**	**CdS/ZnO 1:2**	**CdS/ZnO 1:3**
Staphylococcus aureus	30	17	18	22
E.coli	24	11	13	14
Klebsiella pneumonia	23	8	11	13

References:

1. Horan, T. C. - Culver, D. H. - Gaynes, R. P. - Jarvis, W. R. - Edwards, J. R. - Reid, C. R.,The Official Journal of the Society of Hospital Epidemiologists of America, 14, 73 (1993).
2. J. R. Morones, J. L. Elechiguerra, A. Camacho, J. T. Ramirez, Nanotechnology 16, 2346 (2005).
3. A.E. van den Bogaard, E.E. Stobberingh, Int J Antimicrob Agents. 14, 327(2000).
4. J. S. Kim, E. Kuk, K. N. Yu, J. H. Kim, S. J. Park, H. J. Lee, Nanomed. Nanotechnol. Biol. Med. 3, 95 (2007).
5. G. Zhao, S. E.Stevens, BioMetals 11, 27 (1998).
6. J.H. Crabtree, R.J. Burchette, R.A. Siddiqi, I.T. Huen, L.L. Hadnott, A. Fishman, Perit Dial Int. 23, 368 (2003).
7. A. Krolikowska, A. Kudelski, A. Michota, J. Bukowska, Surf. Sci. 532, 227 (2003).
8. M. Catauro, M.G.Raucci, F.D. De Gaaetano, A. Marotta, J. Mater. Sci. Mater. Med. 15, 831 (2004).
9. P. Gong, H. Li, X. He, K. Wang, J. Hu, W. Tan, Nanotechnology 18, 604 (2007).
10. P. S. Retchkiman-Schabes, G. Canizal, R. Becerra-Herrera, C. Zorrilla, H. B. Liu, J. A. Ascencio, Opt. Mater. 29, 95(2006).
11. H. Gu, P. L. Ho, E. Tong, L. Wang, B. Xu, Nano Lett. 3, 1261(2003).
12. Z. Ahmad, R. Pandey, S. Sharma, G. K. Khuller. Ind J. Chest. Dis. Allied Sci. 48, 171 (2005).

13. M. Kawashita, S. Tsuneyama, F. Miyaji, T. Kokubo, H. Kozuka, K. Yamamoto, Biomater. 21, 393 (2000).
14. Q.L. Feng, J. Wu, G.Q. Chen, F.Z. Cui, T.N. Kim, J.O. Kim, J. Biomed. Mater. Res. 52, 662 **(**2000).
15. K.-H. Liao, K. Liang Ou, H.-C. Cheng, C.-T. Lin, P.-W. Peng, Appl. Surf. Sci. 256, 3642 (2010).
16. K.H. Cho, J.E. Park, T. Osaka, S.G. Park, Electrochim. Acta 5, 1956 (2005).
17. S.L. Percival, P.G. Bowler, D. Russell, J. Hosp. Infect. 60, 1 (2005).
18. J.B. Wright, K. Lam, D. Hansen, R.E. Burrell, Am. J. Infect. Control 27, 344 (1999).
19. G. Ershov, E. Janata, A. Henglein, J. Phys. Chem. 97, 339 (1993).
20. F. Fu-Ren, A. J. Bard, J. Phys. Chem. 106, 279 (2002).
21. G. Zhao, S. E. Stevens Jr, Biometals 11, 27 (1998).
22. B. G. Ershov, E. Janata, A. Henglein, J. Phys. Chem. 97, 339 (1993).
23. F.-R. F. Fan, A. J. Bard, J. Phys. Chem. 106, 279 (2002).
24. B. L. Ouay, F. Stellacci, Nano Today, 10, 339—354 (2015).
25. T.M. Lopez Goerne, M.A. Alvarez Lemus, V.A. Morales, E.G. López, P.C. Ocampo, J. Nanomed. Nanotechol. S5, 003 (2012).
26. W-C. Lin, C-N. Chen, T-T. Tseng, M-H. Wei, J.H. Hsieh, W.J. Tseng, J. Eur. Ceram. Soc. 30, 2849 (2010).
27. K. M. Reddy, K. Feris, J. Bell, D. G. Wingett, C. Hanley, A. Punnoose, Appl. Phys. Lett. 90, 213902 (2007).
28. L. Brunet, D.Y. Lyon, E.M. Hotze, P.J.J. Alvarez, M. Wiesner, Environ. Sci. Technol. 43, 4355 (2009).

29. T. Szabó, J. Németh, I. Dékány, Colloids and Surfaces A: Physicochemical and Engineering Aspects 230, 23 (2003).
30. O. V. Abramov, A. Gedanken, Y. Koltypin, N. Perkas, I. Perelshtein, E. Joyce, T. J. Mason, Surface and Coatings Technology 204, 718 (2009).
31. H. Yamada, K. Suzuki, S. Koizumi, 32, 193 (2007).
32. O.Yamamoto, International Journal of Inorganic Materials 3, 643 (2001).
33. D. Sharma, J. Rajput, B. S. Kaith, M. Kaur, S. Sharma, Thin Solid Films, 519, 1224 (2010).
34. A. Azam, A. S. Ahmed, M. Oves, M. S. Khan, S. S. Habib, A. Memic, International Journal of Nanomedicine 7, 6003 (2012).
35. N. Tran, A. Mir, D. Mallik, A. Sinha, S. Nayar, T. J. Webster, International Journal of Nanomedicine 5, 277 (2010).
36. P. K. Stoimenov, R. L. Klinger, G. L. Marchin, K. J. Klabunde, Langmuir 18, 6679 (2002).
37. Z. Wei, Z. Zhou, M. Yang, C. Lin, Z. Zhao, D. Huang, Z. Chen, J. Gao, J. Mater. Chem. 21, 16344 (2011).
38. H. Kong, J. Song, J. Jang, Chem. Commun. 46, 6735 (2010).
39. P. Basnet, G. K. Larsen, R. P. Jadeja, Y.-C. Hung, Y. Zhao, ACS Appl. Mater. Interfaces 5, 2085 (2013).
40. O. Mahapatra , M. Bhagat, C. Gopalakrishnan, K. D. Arunachalam, Journal of Experimental Nanoscience 3, 185 (2008).
41. I. Matai, A. Sachdev, P. Dubey, S. Uday Kumar, B. Bhushan, P. Gopinath, Colloids and Surfaces B: Biointerfaces 115, 359 (2014).
42. L. Kvitek, A. Panacek, J. Soukupova, M. Kolar, R. Vecerova, R. Prucek, J. Phys. Chem. C 112, 5825 (2008).

43. J. R. Morones, J. L. Elechiguerra, A. Camacho, K. Holt, J. Kouri, J. T. Ramirez, Nanotechnology 16, 2346 (2005).

44. H. S. Rosenkranz, H. S. Carr, Antimicrob. Agents Chemother. 5, 199 (1972).

45. P. D. Bragg, D. J. Rainnie, Can. J. Microbiol. 20, 883 (1974).

46. W. J. A. Schreurs, H. Rosenberg, J. Bacteriol. 152, 7 (1982).

47. M. Yamanaka, K. Hara, J. Kudo, Appld. Env. Microbiol. 71, 7589 (2005).

48. J.B. Wright, K. Lam, D. Hansen, R.E. Burrell, Am. J. Infect. Control 27, 344 (1999).

49. P.T. Sudheesh Kumar, S. Abhilash, K. Manzoor, S.V. Nair, H. Tamura, R. Jayakumar, Carbohydr. Polym. 80, 761 (2010).

50. A. Sirelkhatim, S. Mahmud, A. Seeni, N. Haida, M. Kaus, L. Chuo Ann, S. K. Mohd Bakhori, H. Hasan, D. Mohamad, Nano-Micro Lett. 7, 219 (2015).

51. F.J. Souza-Filho, A.J. Soares, M.E. Vianna, A.A. Zaia, C.C.R. Ferraz, B.P.F.A. Gomes, Braz. Dent. J. 19, 28 (2008).

52. A. Azam, A.S. Ahmed, M. Oves, M.S. Khan, S.S. Habib, A. Memic, Int. J. Nanomedicine. 7, 6003 (2012).

53. M. Zirak, O. Akhavan, O. Moradlou, Y.T. Nien, A.Z. Moshfegh, J. Alloys Comp. 590, 507 (2014).

54. V. Lakshmi Prasanna, Rajagopalan Vijayaraghavan, Langmuir 31, 9155 (2015).

55. R. Brayner, R. Ferrari-Iliou, N. Brivois, S. Djediat, M.F. Benedetti, F. Fiévet, Nano Lett. 6, 866 (2006).

56. P.J.P. Espitia, N.F.F.S. Soares, J.S.R. Coimbra, N.J. Andrade, R.S. Cruz, E.A.A. Medeiros, Food Bioprocess Technol. 5, 1447 (2012).
57. S.M. Dizaj, F. Lotfipour, M. Barzegar-Jalali, M.H. Zarrintan, K. Adibkia, Mater. Sci. Eng. C 44, 278 (2014).
58. A. Sirelkhatim, S. Mahmud, A. Seeni, N.H.M. Kaus, L.C. Ann, S.K.M. Bakhori, H. Hasan, D. Mohamad, Nano-Micro Lett. 7, 219 (2015).
59. K. Hirota, M. Sugimoto, M. Kato, K. Tsukagoshi, T. Tanigawa, H. Sugimoto, Ceram. Int. 36, 497 (2010).

CHAPTER 6

CONCLUSION & FUTURE WORK

7.1 Conclusion

7.2 Future work

6.1 Conclusion

This thesis focuses on synthesis and study of different properties of nanocomposites. Heterostructure nanocomposites combine two or more disparate materials on the same nanosystem and represent a powerful approach for achieving advanced materials with multiple functionalities stemming from the unusual materials combinations. Synthesis procedures offering high degree of control over the number of components, their compositions, shapes, and interfacial characteristics are discussed. The convenient and mild conditions offered by the wet chemical process for the preparation of nanocomposites has paved the way for the synthesis of new materials that display unique properties.The combined and often synergistic properties of the heterostructure nanocomposites are described with emphasis on optical properties, magnetic properties, antibacterial properties and light induced charge separation effects. Progress toward the application of hybrid nanoparticles in photocatalysis and antibacterial activity is overviewed. The charge transfer dynamics have attracted significant interest also due to the implications of this process on photocatalytic applications of nanocomposites.

We point out some challenges for further development and understanding of heterostructure nanocomposites. Effective conversion of light energy to chemical energy that can be either used or stored is the key for application of these nanocomposites in photodegradation of organic contaminants for water purification and additional environmental related aspects, in energy applications such as in photoelectrochemical cells, and for their use toward hydrogen generation by photochemical water splitting.

As Antibiotic resistance is a serious and growing phenomenon in public health, antibiotics having a different mechanism of action are urgently needed for modifications in the traditional antimicrobial compounds. Owing to their large specific surface area and high bioactivity the developments of nanoparticles with antimicrobial activity have been emerging

as a new class of biomedical materials having improved or distinct antibacterial activity against multidrug-resistant human pathogenic microbes to fulfil the increasing demands for hygiene in daily life. Therefore, applications in fields such as biology and medicine are still under exploration, and such studies for suitable heterostructure nanocomposites are of interest.With regard to nanomaterials, heterostructure nanocomposites with distinct morphologies have drawn attention as they combine the properties of the constituent elements to exert a more pronounced and synergistic effect. Further challenges in heterostructure nanocomposites are to enlarge the selection of materials by development of new combinations, architectures, and higher complexity with multiple-material structures via known and novel synthetic strategies. This leads to multiple functionalities on heterostructure nanocomposites with clear relevance to photocatalysis, water splitting, optical components and biomedical applications.

6.2 Future work

Although various nanocomposite materials have been already synthesized and studied in this thesis, the work can be continued in different direction. In future the following works can be done,

Iron(III) oxide (Fe_2O_3), including α-, β-, ε-, and γ-Fe_2O_3, is a narrow band gap semiconductor which is suitable to be coupled with ZnO to enhance the separation of photogenerated electron–hole pairs in ZnO and Fe_2O_3. Both the valence band and the conduction band of Fe_2O_3 are more negative than those of ZnO, thus allowing photo-generated electron transfer from the conduction band of Fe_2O_3 to the conduction band of ZnO after light activation. The hetero-nanostructure of these two oxides (Fe_2O_3- ZnO) is also expected to display enhanced abilities, such as a broader light absorption range and high effi-

ciency electron–hole separation. Furthermore, Fe_2O_3-ZnO -based sensor shows higher responses to various combustible gases with a faster response/recovery time. These favorable gas-sensing features make the present Fe_2O_3-ZnO nanocomposite to be particularly attractive as a promising practical sensor.

Potential antibacterial applications of graphene and graphenebased nanocomposites have attracted considerable interests, although whether and how graphene oxide (GO) presents antibacterial activity are still under debate.The increasing demand in the development of novel hybrid materials as effective antibacterial agent motivated the researchers to utilize reduced graphene oxide (rGO) /metal oxide(TiO_2, NiO, ZnO, CuO, Co_3O_4 and Fe_2O_3) nanocomposites toward advancements in antibacterial application. Potent antibacterial has been attributed to membrane stress induced by sharp edges of graphene nanosheets, which may result in physical damage to cell membranes. On the other hand, metal oxides(TiO_2, NiO, ZnO, CuO, Co_3O_4 and Fe_2O_3) also exhibit antibacterial activity against bacteria. Therefore, reduced graphene oxide (rGO) tethered with metal oxides such as TiO_2, NiO, ZnO, CuO, Co_3O_4 and Fe_2O_3 may be synthesized and utilized as antibacterial agent.

The considerable antimicrobial activities of metal oxide NPs such as ZnO, Fe_2O_3, Fe_3O_4, MgO, CuO, TiO_2, SiO_2 and their selective toxicity to biological systems suggest their potential applications as nano medicine based antimicrobial agents. The antiseptic qualities of medicinal plants have been long recognized. Biologically active compounds which are present in plants have always been of great interest. A new approach has been taken to study the antibacterial property of medicinal plant extracts treated metal oxides.

Hydrogen production via photocatalytic water splitting using sunlight has enormous potential in solving the worldwide energy and environmental crisis. Water is the most plentiful supply of hydrogen that can be used to produce hydrogen via photocatalytic water splitting. The combination of different semiconductors to create composite materials offers a promising way to achieve efficient photocatalysts because doing so can improve the charge separation, light absorption and stability of the photocatalysts. Thus, hydrogen production by means of a photocatalyst, solar energy and water has noticeably attracted attention in recent decades. In order to photosensitize wide band gap semiconducting oxides towards the visible region, integrated coupling with narrow band semiconductors such as In_2O_3, Fe_2O_3, CuO, CuS, CdS, ZnS and ZnSe, which possess different redox energy levels provide an attraction to achieve more efficient charge separation, thus prolonging the lifetime of the charge carriers. In this regard, synthesis of ZnO or TiO_2 coupled with these narrow band semiconductors is considered to be a potential candidate for hydrogen evolution via photocatalytic water splitting due to their compatible lattice structures, which leads to strong interactions and consequently facilitate the effective interband charge transfer.

APPENDICES

Title: Synthesis and Self-Assembly of Au@SiO2 Core−Shell Colloids

Author: Yu Lu, Yadong Yin, Zhi-Yuan Li, et al

Publication: Nano Letters

Publisher: American Chemical Society

Date: Jul 1, 2002

PERMISSION/LICENSE IS GRANTED FOR YOUR ORDER AT NO CHARGE

This type of permission/license, instead of the standard Terms & Conditions, is sent to you because no fee is being charged for your order. Please note the following:

- Permission is granted for your request in both print and electronic formats, and translations.
- If figures and/or tables were requested, they may be adapted or used in part.
- Please print this page for your records and send a copy of it to your publisher/graduate school.
- Appropriate credit for the requested material should be given as follows: "Reprinted (adapted) with permission from (COMPLETE REFERENCE CITATION). Copyright (YEAR) American Chemical Society." Insert appropriate information in place of the capitalized words.
- One-time permission is granted only for the use specified in your request. No additional uses are granted (such as derivative works or other editions). For any other uses, please submit a new request.

If credit is given to another source for the material you requested, permission must be obtained from that source.

ELSEVIER LICENSE
TERMS AND CONDITIONS

Nov 18, 2016

This Agreement between Tushar Kanti Jana ("You") and Elsevier ("Elsevier") consists of your license details and the terms and conditions provided by Elsevier and Copyright Clearance Center.

License Number	3991870681731
License date	Nov 18, 2016
Licensed Content Publisher	Elsevier
Licensed Content Publication	Environment International
Licensed Content Title	Recent advances in photocatalytic treatment of pollutants in aqueous media
Licensed Content Author	P. Anil Kumar Reddy,P. Venkata Laxma Reddy,Eilhann Kwon,Ki-Hyun Kim,Tahmina Akter,Sudhakar Kalagara
Licensed Content Date	May 2016
Licensed Content Volume Number	91
Licensed Content Issue Number	n/a
Licensed Content Pages	10
Start Page	94
End Page	103
Type of Use	reuse in a thesis/dissertation
Intended publisher of new work	other
Portion	figures/tables/illustrations
Number of figures/tables/illustrations	1
Format	print
Are you the author of this Elsevier article?	No
Will you be translating?	No
Order reference number	
Original figure numbers	Fig. 1.
Title of your thesis/dissertation	SYNTHESIS AND STUDY OF DIFFERENT HETEROSTRUCTURED NANOCOMPOSITE MATERIALS
Expected completion date	May 2017
Estimated size (number of pages)	150
Elsevier VAT number	GB 494 6272 12
Requestor Location	Tushar Kanti Jana Vill+P.O- Sankoa P.S- Kharagpur(Local) Dist- Paschim Medinipur Kharagpur, 721301 India Attn: Tushar Kanti Jana
Total	0.00 USD

ELSEVIER LICENSE
TERMS AND CONDITIONS

Nov 18, 2016

This Agreement between Tushar Kanti Jana ("You") and Elsevier ("Elsevier") consists of your license details and the terms and conditions provided by Elsevier and Copyright Clearance Center.

License Number	3991841031707
License date	Nov 18, 2016
Licensed Content Publisher	Elsevier
Licensed Content Publication	Journal of Colloid and Interface Science
Licensed Content Title	Electrospun nanofibers of TiO2/CdS heteroarchitectures with enhanced photocatalytic activity by visible light
Licensed Content Author	Chunyan Su,Changlu Shao,Yichun Liu
Licensed Content Date	1 July 2011
Licensed Content Volume Number	359
Licensed Content Issue Number	1
Licensed Content Pages	8
Start Page	220
End Page	227
Type of Use	reuse in a thesis/dissertation
Intended publisher of new work	other
Portion	figures/tables/illustrations
Number of figures/tables/illustrations	1
Format	print
Are you the author of this Elsevier article?	No
Will you be translating?	No
Order reference number	
Original figure numbers	Fig. 12.
Title of your thesis/dissertation	SYNTHESIS AND STUDY OF DIFFERENT HETEROSTRUCTURED NANOCOMPOSITE MATERIALS
Expected completion date	May 2017
Estimated size (number of pages)	150
Elsevier VAT number	GB 494 6272 12
Requestor Location	Tushar Kanti Jana Vill+P.O- Sankoa P.S- Kharagpur(Local) Dist- Paschim Medinipur Kharagpur, 721301 India Attn: Tushar Kanti Jana
Total	0.00 USD

ELSEVIER LICENSE
TERMS AND CONDITIONS

Nov 28, 2016

This Agreement between Tushar Kanti Jana ("You") and Elsevier ("Elsevier") consists of your license details and the terms and conditions provided by Elsevier and Copyright Clearance Center.

License Number	3991840546805
License date	Nov 18, 2016
Licensed Content Publisher	Elsevier
Licensed Content Publication	Materials Letters
Licensed Content Title	Optical and magnetic properties of elliptical hematite (α-Fe2O3) nanoparticles coated with uniform continuous layers of silica of different thickness
Licensed Content Author	Jen-Bin Shi,Chia-Wei Lee,Jhe-Wei Guo,Min-Jung Cheng,Chien Wu,Chih-Jung Chen,Yu-Cheng Chen,Ya-Ting Lin,Chung-Chieh Chang
Licensed Content Date	December 2007
Licensed Content Volume Number	61
Licensed Content Issue Number	30
Licensed Content Pages	3
Start Page	5268
End Page	5270
Type of Use	reuse in a thesis/dissertation
Portion	figures/tables/illustrations
Number of figures/tables/illustrations	1
Format	print
Are you the author of this Elsevier article?	No
Will you be translating?	No
Order reference number	
Original figure numbers	Fig. 3.
Title of your thesis/dissertation	SYNTHESIS AND STUDY OF DIFFERENT HETEROSTRUCTURED NANOCOMPOSITE MATERIALS
Expected completion date	May 2017
Estimated size (number of pages)	150
Elsevier VAT number	GB 494 6272 12
Requestor Location	Tushar Kanti Jana Vill+P.O- Sankoa P.S- Kharagpur(Local) Dist- Paschim Medinipur Kharagpur, 721301 India Attn: Tushar Kanti Jana
Total	0.00 USD

Terms and Conditions

ELSEVIER LICENSE
TERMS AND CONDITIONS

Nov 18, 2016

This Agreement between Tushar Kanti Jana ("You") and Elsevier ("Elsevier") consists of your license details and the terms and conditions provided by Elsevier and Copyright Clearance Center.

License Number	3991850474152
License date	Nov 18, 2016
Licensed Content Publisher	Elsevier
Licensed Content Publication	Physica B: Condensed Matter
Licensed Content Title	Synthesis and magnetic properties of antiferromagnetic Co3O4 nanoparticles
Licensed Content Author	H.T. Zhu,J. Luo,J.K. Liang,G.H. Rao,J.B. Li,J.Y. Zhang,Z.M. Du
Licensed Content Date	1 September 2008
Licensed Content Volume Number	403
Licensed Content Issue Number	18
Licensed Content Pages	5
Start Page	3141
End Page	3145
Type of Use	reuse in a thesis/dissertation
Intended publisher of new work	other
Portion	figures/tables/illustrations
Number of figures/tables/illustrations	1
Format	print
Are you the author of this Elsevier article?	No
Will you be translating?	No
Order reference number	
Original figure numbers	Fig. 5
Title of your thesis/dissertation	SYNTHESIS AND STUDY OF DIFFERENT HETEROSTRUCTURED NANOCOMPOSITE MATERIALS
Expected completion date	May 2017
Estimated size (number of pages)	150
Elsevier VAT number	GB 494 6272 12
Requestor Location	Tushar Kanti Jana Vill+P.O- Sankoa P.S- Kharagpur(Local) Dist- Paschim Medinipur Kharagpur, 721301 India Attn: Tushar Kanti Jana
Total	0.00 USD

ELSEVIER LICENSE
TERMS AND CONDITIONS

Nov 18, 2016

This Agreement between Tushar Kanti Jana ("You") and Elsevier ("Elsevier") consists of your license details and the terms and conditions provided by Elsevier and Copyright Clearance Center.

License Number	3991850053828
License date	Nov 18, 2016
Licensed Content Publisher	Elsevier
Licensed Content Publication	Colloids and Surfaces B: Biointerfaces
Licensed Content Title	Antibacterial activity and mechanism of Ag–ZnO nanocomposite on S. aureus and GFP-expressing antibiotic resistant E. coli
Licensed Content Author	Ishita Matai,Abhay Sachdev,Poornima Dubey,S. Uday Kumar,Bharat Bhushan,P. Gopinath
Licensed Content Date	1 March 2014
Licensed Content Volume Number	115
Licensed Content Issue Number	n/a
Licensed Content Pages	9
Start Page	359
End Page	367
Type of Use	reuse in a thesis/dissertation
Intended publisher of new work	other
Portion	figures/tables/illustrations
Number of figures/tables/illustrations	1
Format	print
Are you the author of this Elsevier article?	No
Will you be translating?	No
Order reference number	
Original figure numbers	Fig. 7.
Title of your thesis/dissertation	SYNTHESIS AND STUDY OF DIFFERENT HETEROSTRUCTURED NANOCOMPOSITE MATERIALS
Expected completion date	May 2017
Estimated size (number of pages)	150
Elsevier VAT number	GB 494 6272 12
Requestor Location	Tushar Kanti Jana Vill+P.O- Sankoa P.S- Kharagpur(Local) Dist- Paschim Medinipur Kharagpur, 721301 India Attn: Tushar Kanti Jana
Total	0.00 USD